博　士　論　文

令和３年度

近畿大学大学院

総合理工学研究科

エレクトロニクス系工学専攻

19-4-434-0404　NOOR SHAHIRA BINTI MASROON

博　士　論　文

令和 3 年度

STUDY ON CONTROL OF PLASMA CONFINEMENT LAYER FOR EFFICIENT LASER PEENING

Preface

This dissertation describes the results of a Ph.D. study initiated in April 2019 finished in March 2022. The study was done mainly at Kindai University, Osaka, Japan. To succeed in the Ph.D. study, I had to combine my theoretical knowledge and practical experiences in the past years and more. It was a real challenge for me to execute this research and take it to the next level during this Corona pandemic.

The innovation of laser technology has contributed to the enhancement of people's way of life in various fields including scientific, industrial, medical, power plant, and military applications. Laser applications have covered a broad spectrum going from nano-applications to heavy industrial applications. Lasers are expected to be a vitally important tool for future surface engineering because their processing and other functions are easy to digitally control.

In surface engineering, attention is devoted to the laser peening process. Laser peening is a surface modification technique that uses laser-induced shock waves to create compressive residual stress. By enhancing the surface properties of materials, surface-related failures such as corrosion, wear, and fatigue can be prevented. Not many people are aware that laser peening is a promising technique to repair metal surfaces in liquid environments such as nuclear power plants, turbine blades of generators, and bridges.

The bodywork presented in this dissertation is conducted in the context of laser peening treatment under a liquid confining medium. Discussions regarding this topic have dominated research in recent years. The mechanisms of the laser peening process under a liquid confining medium are still unclear and require further studies. To achieve an efficient laser peening process, the desirable laser peening parameters are required. The knowledge on the effects of controlling the plasma confinement layer toward the laser peening process is the focus of this dissertation. The results obtained throughout this study provide information that helps to understand the laser peening process in a liquid environment. In addition, it has been proven that with proper selection of laser peening parameters and suitable conditions of plasma confinement layer, effective laser peening can be achieved regardless of the lower energy laser pulse. This could be beneficial, particularly in small companies.

This Ph.D. dissertation is the end of my education at Kindai University. I would like to thank the Kindai University for obtaining an education at an excellent level and being an important part of my life.

Acknowledgment

In the name of Allah, the Most Gracious and the Most Merciful

Alhamdulillah, all praises to Allah for the strengths and His blessing in completing this dissertation. The completion of this dissertation would not have been possible without the assistance, guidance, and support of a great number of people, to all of whom I will always be grateful.

I would like to express my sincere gratitude to my Supervisor Prof. Hitoshi Nakano for his encouragement, useful comments, remarks, and engagement through the learning process of this dissertation. He has been my supervisor since my undergraduate study. His professionalism has been of great importance in my development and to strengthen my critical thinking. I am extremely grateful for his responsive guidance and care that went beyond the formal duties of a supervisor.

I would also like to acknowledge Prof. Minoru Yoshida as the main examiner and Prof. Takaomi Matsutani as the second examiner of this dissertation. I am gratefully indebted to them for their very valuable support and feedback during the process.

Special thanks to the Heiwa Nakajima Foundation and Iwatani Naoji Foundation for the support through financial. The financial assistance has been a great help to me in paying my educational expenses, and it allowed me to concentrate more of my time on studying.

I would like to acknowledge the technical and moral support that I received from the members of the Laser Engineering Laboratory. Thank you all for the wonderful moments and discussions.

Finally, I want to express my heartfelt gratitude to my loving parents and family for their unending love, prayers, encouragement, and support throughout my studies. To those who indirectly contributed to this research, your kindness means a lot to me. Thank you so much for everything.

Contents

Chapter 1: Introduction and background

1.1 Surface engineering

1.1.1 Surface enhancement method

Metals are an important part of our lives. A metal failure is a breakdown of a metal due to various factors that affect its strength, stability, and chemical composition. Applied stress, material flaws, and operating conditions can contribute to metal failure. The most common types of metal failure are metal cracking, fatigue failure, cavitation, and corrosion. The failure of one unit or even a small component could lead to a serious matter. Therefore, surface engineering is required, particularly in the industrial sector.

Surface engineering is the process of modifying or coating the surface of a component to improve the function and serviceability of the components for securing the reliability and safety of the products. In surface engineering, various methods of improving the properties of metallic components have been developed [1]. Those properties such as corrosion resistance, wear resistance, or thermal insulation can be enhanced metallurgically, mechanically, chemically, or by adding a coating.

Peening is a common surface modification process used to improve the material properties of metal by inducing compressive residual stress on the surface layer through the application of a mechanical force [2,3]. The most effective and widely used peening technology is shot peening. Shot peening has been applied to many engineering materials for the past seven decades [4]. This technique involves accelerating round metallic, glass, or ceramic particles at high velocities towards the surface of the material and causes plastic deformation which changes the mechanical properties of the surface. It is a kind of surface hammering that creates an indentation on the surface, leading to a highly shocked and compressed region below the indentation. The compressive residual stress induced on the surface is beneficial to improve fatigue life. The size of the particles can be varied in size depending upon the processing condition. Using the larger size of the particles or increasing the velocity of the shot could increase the intensity of the shot peening process. The advantages of the shot peening technique are easy to handle, economical, and can be used on large or small areas as required. However, the shot peening process has its limitations. The surface topography after shot peening is usually rough due to the dimples created by the peening media [4]. In addition, the compressive residual stress induced by shot peening is small, which is not exceeding 250 μm.

Compared with shot peening and other conventional methods, laser peening (also known as laser shock processing) can induce greater depths of compressive residual stress into metal surfaces. Laser peening is a cold working process that uses high laser intensity and a short pulse to initiate the formation of plasma. The shock waves generated from the high-pressure plasma cause plastic deformation on the surface of the material. Among the

major advantages of the laser peening process, five important ones are non-contact processing, smoother processes surfaces, precision process, and high flexibility to treat complex geometrical components

1.1.2 Development of the laser peening technology

Historically, laser peening has been in existence for over five decades. It was first developed at Battelle Laboratory in the 1960s but not commercialized for years due to the lack of a reliable, high repetition rate, high average-power laser. Thorough knowledge of the fundamentals of laser interaction with the target material is very important. Many investigations to understand the interaction of the laser with matter and to generate high pressures were done during the 1960s to early ’70s. From the mid-1980s until the early 1990s, Fabbro, Peyre, and colleagues in France performed a broad-based laser peening effort centered on their high-energy pulsed laser facilities [5–8]. The French programs have given a great contribution to the understanding of laser shock processing to where it stands today.

Laser peening technology has gained an increasing amount of attention and research interest in the past decade [1,6,7,9–12]. Nowadays, laser peening technology has become a reliable surface enhancement technique that improves the properties of metallic materials to prevent surface-related failures [13,14]. It has been widely applied in various sectors such as power generation, automobile, maritime, and many more. Laser peening is advantageous since it has demonstrated high potential and applicability at the industrial level, particularly for crucial components. Because of the increase in the depth of compressive residual stress, the technology has greatly enhanced the mechanical characteristics and performance of numerous engineering materials. High compressive residual stresses on the surface of the material can prohibit crack propagation or minimize stress concentration. In addition, surface enhancement by using a high-power laser is a convenient process when it is necessary to treat well-defined components which have a complex geometry.

1.2. Research motivation

Laser peening was chosen for investigation in this study because it is an emerging surface treatment that is used to improve many properties of the target material such as fatigue life, wear and corrosion resistance, hardness, etc. For application in a large area, the laser peening process relatively high-cost surface treatment technique compared to other forms of peening. However, laser peening generates compressive residual stress fields in tailored properties that can be reliably controlled by the selection of laser peening parameters [15,16]. Significant progress has been made to reduce the cost and increase the throughput of the process, producing a large number of affordable applications.

The efficiency of laser peening treatment is determined by the magnitude of compressive residual stress introduced on the surface of the material. The distribution of

residual stress is dependent on the generation and propagation of a shock wave (or dynamic stress). A breakthrough in attaining a high-pressure pulse was achieved when the plasma expansion occurring in confined mode can be increased with the magnitude of the shock wave pressure 3-4 times greater compared to the direct ablation [17]. In confined mode, a plasma confinement layer that is transparent to the laser beam, typically water, helps amplify the magnitude of the shock wave by resisting the plasma expansion away from the metal surface.

In the case of the laser peening treatment under a liquid medium as a plasma confinement layer, when the high-intensity laser beam is focused on metal, the laser-induced cavitation bubble is generated without exception in liquid. The collapse of the cavitation bubble emits a strong shock wave on the metal surface that can lead to plastic deformation on the material surface. Thus, laser peening will be benefitted due to the dual-shock impact from a single-shot pulsed-laser attributed to the confinement of laser-induced plasma and the collapse of the laser-induced cavitation bubble. The dual-impacts must enhance the work-hardening and induce the compressive residual stress in the surface of the metal. Consequently, the resistance of the metal towards surface-related failures such as fatigue, stress corrosion cracking, and fretting fatigue can be increased.

The effects of laser peening in a plasma confinement layer are attributed to the impact of shock waves generated from the confinement of laser-induced plasma, P_L, and the collapse of the laser-induced cavitation bubble, P_C. Therefore, both P_L and P_C are important factors in determining the effectiveness of laser peening treatment.

To the best of our knowledge, the systematic experimental studies regarding the desirable laser peening parameters in a liquid confining medium do not consider properly the dual impacts that occur near the metal surface after laser irradiation. Therefore, a comprehensive investigation is needed.

1.3. Objective

This research aims to achieve a comprehensive investigation on the effects of controlling the plasma confinement layer on the efficiency of the laser peening process. Thereby, the effects of controlling the laser peening parameters on plastic deformation in the stainless steel for a liquid confining medium were observed and discussed in detail. A lot of research has been conducted to study the mechanisms of laser peening in the liquid confining medium. However, the mechanisms are still insufficiently explored. Therefore, systematic experimental studies that properly consider the shock wave pressure that is induced into the metal are developed to contribute to the clarification. This detailed knowledge of the shock impacts that are attributed to the plastic deformation on the material is essential for achieving an efficient laser peening process.

1.4 Outline of the dissertation

Chapter 1: Introduction and background
This chapter provides a general overview of the research topic and goals for this research. Here, the advantages and current issues of the surface enhancement method are presented. Special attention is given to the development and advantage of laser peening technology, followed by the motivation and objective of this research.

Chapter 2: Laser peening process
This chapter contains information about the basic principle of laser peening. This is followed by the confining mode of the laser peening process. Special attention is given to liquid confining mode.

Chapter 3: Research methodologies
This chapter provides a detailed plan for the research experiment. First, the sample preparation and experimental setup for laser peening treatment including laser peening parameters are described. Then, the method to control the plasma confinement layer is described in detail. At the end of the chapter, the methods to evaluate the plastic deformation are given.

Chapter 4: Experimental results and discussion
This chapter discusses the results obtained during my Ph.D. work. This chapter is divided into three main sections to study the effects of controlling the plasma confinement layer on the laser peening process. The effects of other laser peening parameters on the laser peening process are also discussed.

Chapter 5: Conclusions
This chapter presents the summary and conclusions constructed from the established findings of the study. At the end of this chapter, some recommendations and suggestions for future work are proposed.

Appendix
In the appendix, portions of my master's thesis entitled "Study on the development of simple and low-cost longitudinally excited CO_2 laser" completed at Kindai University has been modified and described. Detail about the longitudinally excited CO_2 laser by using a fast-high voltage solid-state switch can be found.

Chapter 2: Laser peening process

This chapter reviews some background physics behind the work presented in this dissertation. The fundamental of the laser peening process was elucidated. Section 2.1 presents a discussion of the basic principle of laser peening, including the physics of laser-induced plasma formation and shock wave pressure that cause the plastic deformation on the surface of the metal. Section 2.2 discusses the confining mode for the laser peening process. Section 2.3 reviews the mechanics of the underwater laser peening process.

2.1 Basic principle of laser peening

Laser peening or laser shock peening is cold work, mechanical surface enhancement process that uses high intensity of several gigawatts (GW) of peak power. The schematic of the principle of laser peening is shown in Fig. 2.1. First, a short-pulsed laser is focused on a metal that is covered by a coating named sacrificial layer. Usually, an opaque black coating is used to effectively form a high-temperature plasma on the surface of the metal. This is because the black overlay has a low vaporization temperature that can easily absorb the high energy pulses and heat up to form a plasma gas. Additionally, a transparent medium such as water is placed on top of the black coating to limit the thermal expansion of the plasma gas and avoid thermally changing the metal properties and microstructure. This transparent overlay is also known as a plasma confinement layer which confines the plasma from rapidly expanding away to the surrounding. The high pressure from laser-induced plasma enhances a shock wave that can travel into the sample and produce plastic deformation, thus creating compressive stresses. This method has been shown to improve the fatigue performance and mechanical properties of various metallic materials.

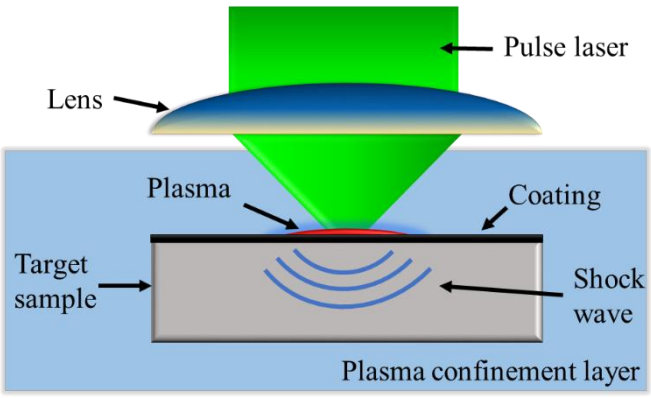

Figure 2.1 Schematic illustration of the principle of laser peening with coating

2.1.1 Physics of laser-induced plasma formation and generation of the pressure pulse

A high-power laser leads to extremely rapid ionization when focused onto matter by the multiphoton process. When the laser-light intensity is exceeding a certain threshold,

which is high enough to induce significant material vaporization, the density of the particles within the vapor plume instantaneously increases. This hot vapor plume or plasma consists of clusters, molecules, atoms, ions, and electrons.

Different mechanisms can lead to laser ablation depending upon the optical, thermal, and mechanical properties of the target. In addition, the characteristics of the laser such as pulse width, laser intensity, and wavelength affect the outcome of the laser ablation process. For nanosecond laser pulses of in the intensity of $<10^8$ W/cm^2, the dominant mechanism of plasma ignition is thermal vaporization because of the existence of free electrons and the electron-lattice coupling time constant is in the order of ps, which is much smaller than the duration of the laser pulse.

Fabbro et al. give a precise description of the mechanisms that involve in the generation of pressure in confinement mode [5]. First, when the laser is switched on, the laser energy is deposited at the interface between the target and the transparent material (see Fig. 2.2). The pressure generated by the plasma induces two shock waves (with velocities D_1 and D_2) propagating inside the target and in the confining medium. Due to the material motion behind the two shock waves, an opening L of the interface occurs, and its thickness increases. Secondly, when the laser is switched off, the plasma continues to maintain a pressure that decreases during its adiabatic cooling, owing to the increase of the plasma interface. Finally, after the plasma has completely recombined, the heated gas inside the interface expands, then adding mechanical momentum to the target.

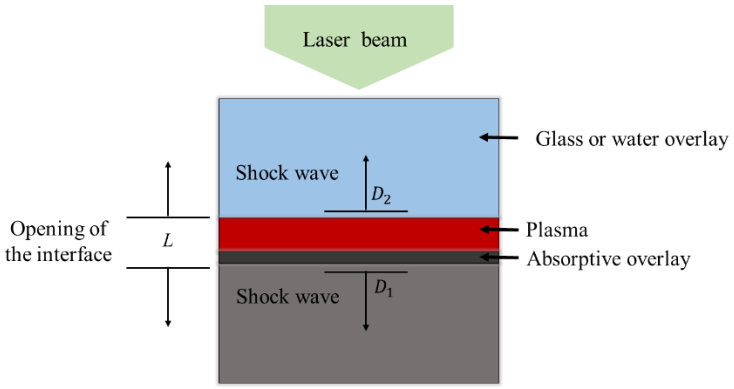

Figure 2.2 Geometry of the target assembly in confined ablation [5]

2.1.2 Propagation of shock wave in the metal

For laser pulse of the ns duration, the ablation process is governed by heat conduction, melting, evaporation, and plasma formation. Shock waves occur when a target is stressed far beyond its elastic limit by a pressure disturbance. Hydrodynamic expansion of plasma causes a shock wave to propagate in the material. It is revealed that the plasma produced by ns laser pulse go through an asymmetric expansion on the initial stage. Then, at a later period, the internal shockwave structure develops and plasma vortical motion

occurs. The structure of shock waves in the plasma during its expansion contains a strong external shock, internal rarefaction shock wave, and many reflected and transmitted shocks.

Depending upon the magnitude of the pressure wave induced into the metal, elastic and plastic deformation on the top region of the component is produced. This deformation creates compressive and tensile residual stresses.

2.1.3 Plastic deformation

Plastic deformation is caused due to the shock wave pressure that propagates through the metal and surpasses the yield strength of the material; subsequently, work-hardening, and compressive residual stress are induced on the metal surface. The dynamic yield strength of a material is depending on the strain, strain-rate, and temperature. Different strain-rates cause the material to react differently.

Hugoniot elastic limit (HEL) is a fundamental dynamic material property of solid materials. The relation between the HEL and the dynamic yield stress (σ_y) is

$$\mathrm{HEL} = \frac{(1-\nu)\sigma_y}{1-2\nu} \tag{2.1}$$

where v is the Poison's ratio.

Although the materials undergo plastic deformation when the pressure exceeds the HEL limit, it must be noted that this plastic deformation will saturate after reaching twice the HEL as shown in Fig. 2.3 [18].

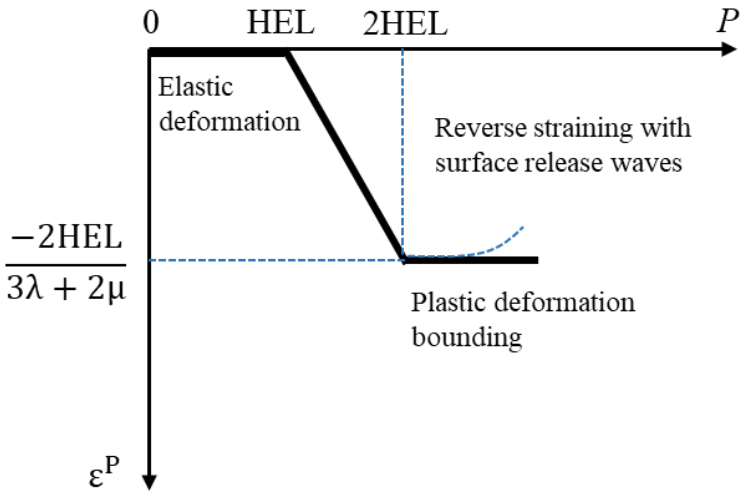

Figure 2.3 Plastic strain induced by laser peening as a function of peak pressure [18]

The yield strength of a material changes depending on a number of elements, including plastic work, pressure, load rate, and temperature. In addition, the stress effect due

to the shock wave pressure that propagates into the material contributes to an increase in the dislocation density and grain refinement.

2.2 Confining mode of the laser peening process

When an intense laser beam irradiates onto a metal surface for a very short period (~30 ns), the heated zone is vaporized to reach temperatures over 10000℃ and then is transformed to plasma by ionization. The plasma continues to absorb the laser energy through inverse bremsstrahlung. The expansion of the high-pressure plasma drives shock waves that propagate isotropically through the material. The interaction of the plasma with a metal surface without any coating or confining medium is defined as 'direct ablation'.

In order to obtain a high amplitude of shock pressure, a laser peening process always uses a confined mode, in which the metal surface is usually coated with an opaque material such as black paint or aluminum foil as a protective coating to prevent the material surface from melting or being damaged, then confined by a transparent material to the laser such as distilled water or glass against the laser radiation [19]. This type of interaction is called 'confined ablation'. Recent research had found that, when using the confined mode, an increase of the pressure by a plasma up to several GPa, which is several times higher than that obtained by direct ablation mode [5,6,8,20]. A stronger shock impact with a high magnitude of compressive residual stress to a deeper depth may benefit the laser peening process. Water is used most often in industrial applications where multiple numbers of laser shots are required in less time because of ease of availability and handling.

The peak pressure owing to the interaction of laser with plasma in confining medium can be estimated by

$$P = 0.01\sqrt{\frac{\alpha}{2\alpha + 3}}\sqrt{Z \cdot I_0} \tag{2.2}$$

$$\frac{2}{Z} = \frac{1}{Z_T} + \frac{1}{Z_C} \tag{2.3}$$

where P, Z, and I_0 are the peak pressure of shock wave , acoustic impedance, and laser intensity, respectively [5,6]. α is a constant that is related to the ratio of thermal to internal energy, and it is shown to be 0.3–0.5, depending on the laser parameters. In eq. (2.3), Z is defined as the reduced acoustic impedance, where Z_T and Z_C are the acoustic impedances of the target sample and confining medium, respectively.

The plasma confinement layer using confining medium plays an important role in the laser peening process to suppress the expansion of laser-induced plasma form rapidly expanding away to the surrounding, thus enhancing the shock wave pressure propagating into the metal. The degree of confining ability was determined by acoustic impedance. The

acoustic impedance Z_C is given by the product of the density d_C and the speed of sound v_S in the medium.

$$Z_C = d_C \times v_S \tag{2.4}$$

The condition or the properties of the plasma confinement layer is the important key factor to realizing a high-efficiency laser peening process. Therefore, the influence of the acoustic impedance of the plasma confinement layer on the laser peening effectiveness has attracted interest as a means of optimizing the conditions for effective surface treatment [21,22]. It should be noted that high transmissivity at the laser wavelength, low chemical reactivity with the target materials, high electrical resistivity, and non-flammability are all needed features for a plasma confinement layer.

2.2.1 Transparent overlay

Transparent materials are in many ways the most important for optics because laser light can pass through them. Transparent solid mediums such as glass, fused quartz, or acrylic can also be used as a plasma confinement layer [5,20,23]. Laser peening treatment by using a solid-state confining medium is suitable for some applications that cannot allow water presence such as electronic device treatment. In addition, when addressing the generic problem to the surface condition or geometry of the target sample, an alternative approach which is soft polymer confinement has been developed [24]. This polymer allows adaptability and shaping possibilities for better confinement. However, the main concern of using a solid confining medium is its incapability for multiple numbers of shots on the same spot. Replacement of the confining medium is necessary to perform multiple shots on the surface of the target thus decreasing the efficiency of laser peening treatment. This concludes that consideration on the ease of application, speed of control, and cost are needed when employing solid medium as a plasma confinement layer.

2.2.2 Water as a plasma confinement layer

Usually, a thin water layer is used to confine the plasma from expanding away from the metal surface not only because of its transparency but also because of ease of availability and handling [5,17]. The laser peening process by using water as a plasma confinement layer allows multiple shocking of a single area of the material. In addition, it ensures contact with the surface and is desirable for nonplanar surfaces.

Generally, the surface of the target sample is coated with an opaque material and covered with a transparent overlay. When a protective coating is used, the remaining coating needs to be removed after the treatment. In 1995, laser peening without coating (LPwC) was discovered for the first time in the world. This technique has been applied in nuclear power

reactors as a preventive maintenance measure against stress corrosion cracking [25,26]. In addition, during the laser peening process, the surface preparation or coating before laser irradiation is not required, thus reducing the operating cycle. In this study, laser peening treatment was carried out by adopting this technique where no protective coating is used as illustrated in Fig. 2.4 [25,27,28].

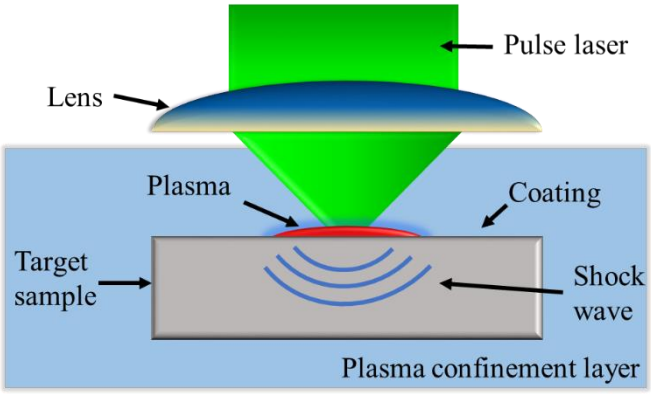

Figure 2.4 Schematic illustration of the principle of laser peening without coating

2.3 Mechanics of underwater laser peening process

Recently, the phenomena of laser-induced cavitation bubble on a solid target are important due to the cavitation impact that can improve the performance of metallic properties and it has gradually attracted many researchers [29–31]. Several investigations have shown that laser peening treatment in a liquid confining medium is beneficial because a single-shot laser pulse can produce a dual-impulse peening effect [12,32].

Laser ablation of a solid target in liquid involves complicated physical processes. Here, the generation of laser-induced cavitation bubble on metal is described briefly. Figure 2.5 shows the formation of laser-induced cavitation bubble after laser irradiation. When the high-intensity laser beam is focused on metal, the laser-induced cavitation bubble is generated without exception in liquid. The generation of the laser-induced cavitation bubble is attributed to pressure induction and energy deposition. In the case of the pressure induction method, a shock wave propels the surrounding liquid and resulting in a pressure drop. The motion of surrounding liquid caused by pressure drop induction results in a formation of a cavitation bubble. On the other hand, during energy deposition by laser irradiation on the metal surface, the plasma accelerates and the generation of a thin layer of water vapor around the plasma causes the formation of a cavitation bubble. The cavitation bubble is generated and it expands outward due to the high pressure within the bubble. This cavitation bubble expands to its maximum size and collapses hundreds of microseconds later from laser irradiation. The collapse of the cavitation bubble emits a strong shock wave on the metal surface that can lead to plastic deformation on the material surface.

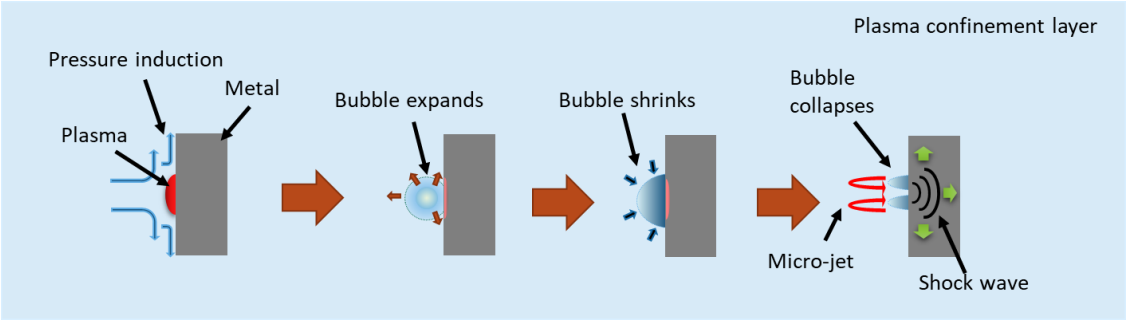

Figure 2.5 Formation of laser-induced cavitation bubble on the metal surface

2.3.1 Formation of laser-induced cavitation bubble

By focusing a short-pulse laser in a liquid environment, a bubble can be generated if the laser irradiation reaches the threshold of the optical breakdown of the liquid. During optical breakdown, nonlinear light absorption due to an ionization process results in a plasma formation. The formation of a plasma in a liquid environment is accompanied by the generation of shock waves. Subsequently, the high-pressure plasma is attributed to the growth of a bubble. For several years, researchers have been giving intensive attention to the dynamics of the laser-induced bubble in a liquid confining medium [33–39]. This bubble behaved similarly to a cavitation bubble. Therefore, a bubble induced by a pulsed laser was named a laser-induced cavitation bubble.

The well-known equation that describes the bubble dynamics in terms of hydrodynamics is the Rayleigh-Plesset equation. Eq. (2.5) displays the Rayleigh equation based on cavitation bubble theory [31].

$$R\ddot{R} + \frac{3}{2}\dot{R}^2 = \frac{P_\infty - P_0}{\rho_L} \tag{2.5}$$

where R is the bubble radius; $\dot{R}$ and $\ddot{R}$ are the velocity and the acceleration of the bubble, respectively; ρ_L is the density of water; P_∞ is static pressure in water; P_0 is vapor pressure in the bubble. The above equation is the general equation of motion for a spherical bubble in liquid. The bubble grows until its maximum size due to huge internal bubble pressure. Afterward, the bubble quickly shrinks due to the imbalance of the bubble pressure and the ambient pressure. This process will be repeated for several cycles until its energy is finally dissipated into the medium. The maximum bubble radius and bubble energy can be obtained;

$$R_{max} = \frac{T_c}{0.915\sqrt{\rho/(P_\infty - P_0)}} \tag{2.6}$$

$$E_B = \frac{4}{3}\pi(P_\infty - P_0)\, R_{max}^3 \tag{2.7}$$

where R_{max} is the maximum bubble radius; T_c is the bubble oscillation period; E_B is the energy of the cavitation bubble. The bubble size is related to its oscillation period T_c.

2.3.2 Effects from the collapse of the laser-induced cavitation bubble

Several studies have shown that laser peening treatment in a liquid confining medium is advantageous because a dual-impulse peening effect can be obtained by a single-shot laser pulse as illustrated in Fig. 2.6 [12,32,39].

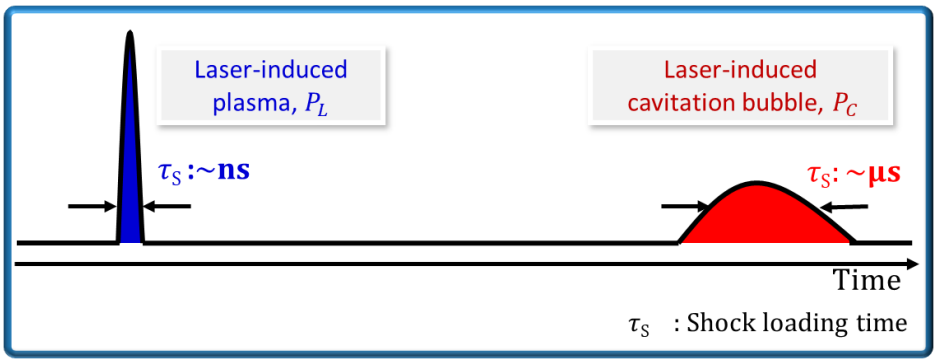

Figure 2.6 Schematic illustration of shock wave pulse from laser-induced plasma P_L and the collapse of laser-induced cavitation bubble P_C.

The shock wave caused by the confinement of laser-induced plasma P_L occurs several tens of nanoseconds immediately after laser irradiation, meanwhile, the shock wave caused by the collapse of laser-induced cavitation bubble P_C occurs in several tens to hundreds of microseconds after the laser-induced plasma disappears [10,29]. In the case of P_L, a high amplitude of shock wave pressure and shock loading time in nanosecond order of time is obtained. However, in the case of P_C, despite having a smaller amplitude of shock wave pulse compared to P_L, it has a longer shock loading time compared to P_L, which is probably in microseconds order. When the peak pressure generated from the confinement of laser-induced plasmas and the collapse of the laser-induced cavitation bubble exceeds the dynamic yield stress, the metal is plastically deformed at the surface. This enhances the work-hardening and induces the compressive residual stress in the surface of the metal. The amplitude of the shock wave pressure and the shock loading time are the critical parameters that have to be optimized to increase the effectiveness of laser peening. The effect of laser peening is given by

$$E_{\mathrm{LP}} \propto \int_0^{\infty} P\, dt \tag{2.8}$$

where E_{LP} is the effect of laser peening and P is the shock wave pressure in a time-dependent. Here, the effect of laser peening is attributed to the impact of shock waves generated from the confinement of laser-induced plasma P_{L} and the collapse of the laser-induced cavitation bubble P_{C}. Hence, both P_{L} and P_{C} are important factors in determining the efficacy of laser peening treatment.

Chapter 3: Research methodologies

3.1 Sample preparation

3.1.1 Material

The austenitic stainless steel SUS316L was selected as a target sample through all experiments. The advantages of austenitic stainless steel as compared with the cheaper martensitic or ferritic ones are better corrosion resistance, workability (ductility), and weldability. SUS316L is widely used in impact-resistant structures. The chemical composition and mechanical properties of SUS316L are shown in Tables 1 and 2, respectively. The properties differ depending on the type and amount of alloying elements added to the steel.

Table 1: Chemical composition of SUS316L stainless steel

Chemical composition	C	Si	Mn	P	S	Ni	Cr	Mo
(%)	≦0.030	≦1.00	≦2.00	≦0.045	≦0.030	12.00 - 15.00	16.00 - 18.00	2-3

Table 2: Mechanical properties of SUS316L stainless steel

Tensile strength (MPa)	Yield strength (MPa)	Elongation (%)	Hardness (HV)
≥ 480	≥ 175	≥ 40	≦200

3.1.2 Polishing

Before performing laser peening treatment on the sample, the sample was mechanically polished. The smoothing of a sample's surface was conducted by using mechanical tools and abrasives. Rough polishing using the polishing machine, the samples were wet-polished by an abrasive paper in the order of 800, 1000, and 1500. As the abrasive paper grit size increased, finer scratches and smoother surfaces were achieved. The process continued by performing mirror polishing of alumina suspension (BAIKOWSKI) with a particle size of 1.0 μm. After the sample surface became a smooth and mirror-like surface, the metal sample was placed in a beaker, and acetone is put until the metal sample was fully immersed. The samples were ultrasonically cleaned in acetone for about 10 minutes to remove the residue on the sample surface effectively.

3.1.3 Annealing

Generally, a metal sample generates stress during processing, so that it is accumulated inside the metal as residual stress. Since laser peening aims to apply compressive residual stress, it is difficult to evaluate the stress if the residual stress exists in the state before the peening treatment. Therefore, to eliminate the internal stresses and unify the initial condition of the mirror-polished metal, an annealing process was performed before laser irradiation.

Figure 3.1 Vacuum electric furnace

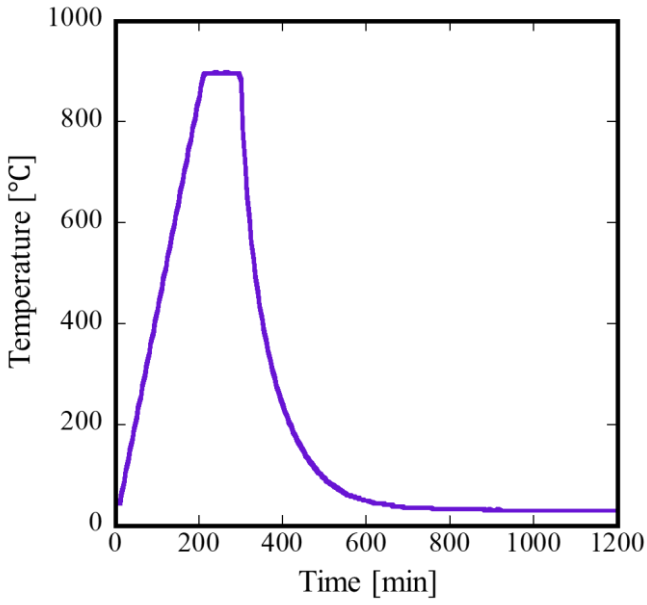

.

Figure 3.2 Temperature profile of annealing process

The annealing was performed using a vacuum electric furnace as shown in Fig. 3.1. To remove the residual stress of austenitic stainless steel, it is recommended to anneal at a

temperature of 900 ℃ in a vacuum condition. Heating was started from room temperature, then increased to the desired annealing temperature of 900 ℃, then the heating temperature was maintained constant. The final step was natural cooling in the furnace until room temperature was reached. The temperature profile of annealing process is shown in Fig. 3.2.

3.2 Experimental setup for laser peening treatment

A laser peening technique without a protective coating layer to impart compressive residual stress on the target samples was adopted in all experiments.

3.2.1 Types of laser used

Pulsed lasers are the preferred sources in laser peening where the laser energy is deposited onto the substrate surface within a short time. In this study, laser peening treatment was performed by a Brilliant Easy Nd: YAG (neodymium-doped yttrium aluminum garnet) type Q-switched laser as shown in Fig. 3.3. The specification of this laser is shown in Table 3. Nd: YAG is a crystal that is used as a laser medium. This laser can be operated in pulsed mode at both wavelengths: fundamental (1064 nm) and second-harmonic (532 nm). Nd: YAG laser is a four-level laser system, which means that four energy levels related to laser action. A flashlamp is used as a pumping source to supply energy to the Nd: YAG to achieve population inversion.

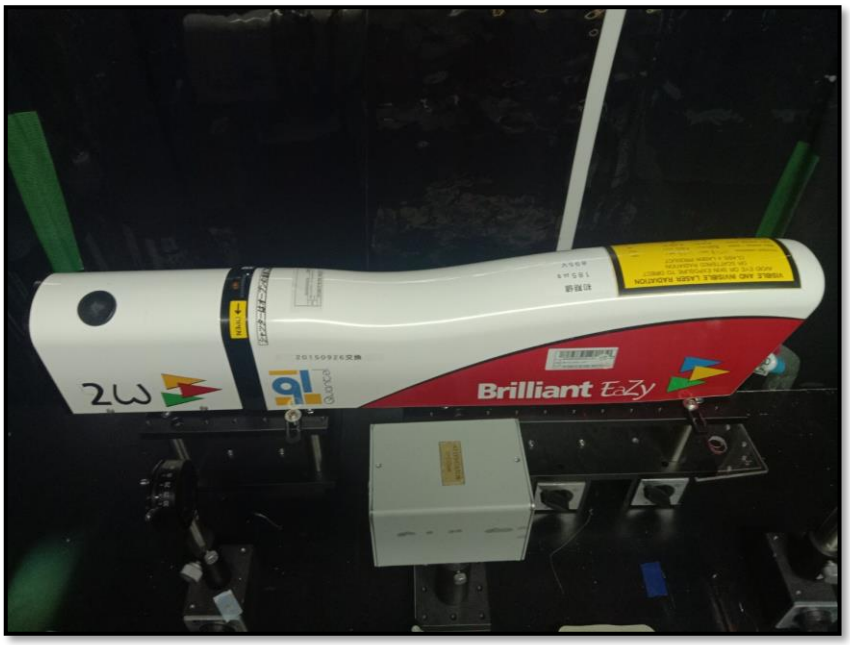

Figure 3.3 Brilliant Easy Nd: YAG laser

Table 3: Specification of a Brilliant Easy Nd: YAG Q-switched laser

Principal radiation [nm]	Max energy per pulse [mJ]	Max average power [W]	Pulse duration [ns]	Repetition rate [Hz]
532	165	1.65	4	10
1064	330	3.3	5	10

Figure 3.4 depicts a simplified diagram of the laser used in this study. The cavity (resonator) is comprised of the cavity rear mirror with maximum reflectivity and the partially reflecting output mirror. The three other components (polarizer, quarter-wave plate, and the electro-optical modulator) are used to radiate to Q-switched laser pulse.

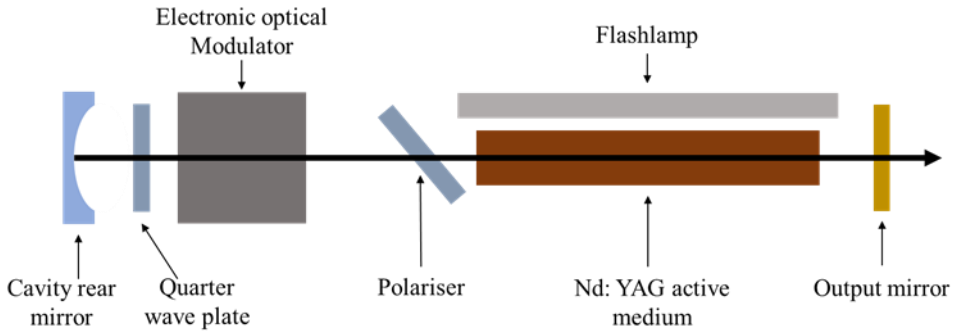

Figure 3.4 Simplified diagram of a Brilliant Easy Nd: YAG Q-switched laser

3.2.2 Optical arrangement

Figure 3.5 represents the experimental setup including the optical arrangement for laser peening treatment. The experiments were performed using a Q-switched Nd: YAG laser operating at 10 Hz. The laser beam was passed through an energy attenuator and pinhole and then focused on the sample using a lens with a focal length of 10 cm. The energy attenuator, consisting of a half-wave plate and cross polarizers, could adjust the laser intensity continuously. The focal spot diameter was fixed at 200 μm by adjusting the size of the pinhole. The sample was supported by a holder and placed in a transparent container, or "peening cell," which was filled with confinement media. The thickness of the confinement medium above the sample was 20 mm, which is sufficient to suppress the expansion of the laser-produced plasma to generate high pressure. The peening cell was then clamped down on an XY stage. The laser beam passed through the confinement medium and struck the sample perpendicularly.

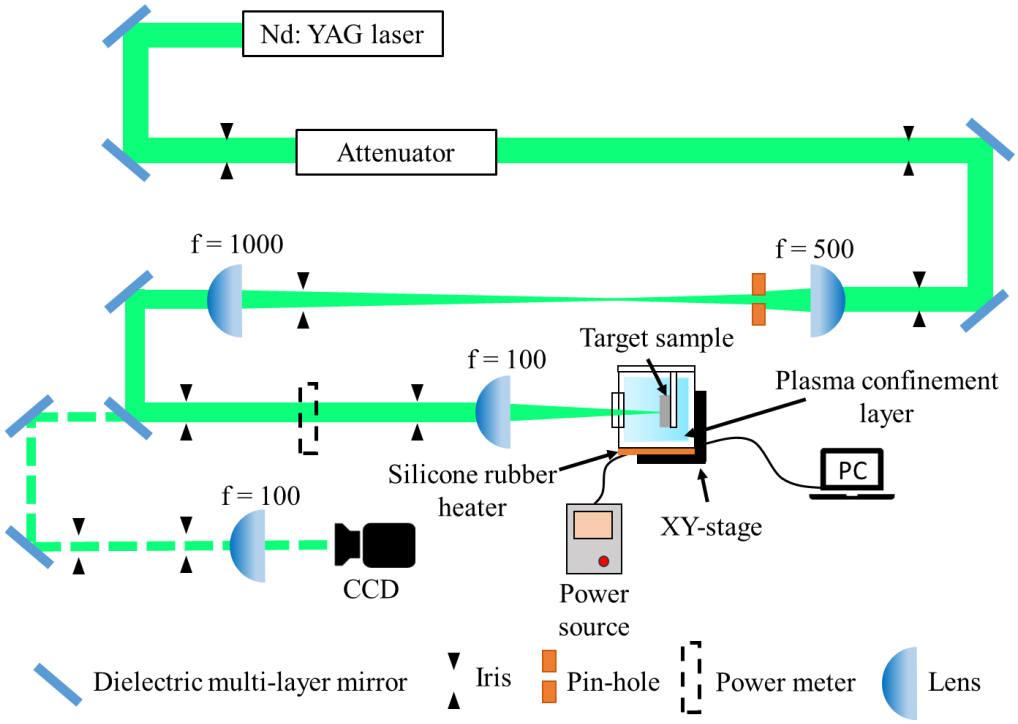

Figure 3.5 Schematic of the experimental setup with optical arrangement for laser peening treatment

3.2.3 Spot diameter

The spot diameter is the diameter of the laser beam in the focal plane when the laser beam is focused by a lens. The plastically affected depth of the treated sample is determined by the spot diameter. When the spot diameter is large, the shock wave propagates in the metal as a plane wave, which resulted in an attenuation rate of 1/r. On the contrary, when the spot diameter is small, the shock wave propagates as a spherical wave, which resulted in an attenuation rate of $1/r^2$. The net result was that the energy attenuation rate was less for the large diameter, and the plane wave can propagate deeper into the treated sample. However, a large spot diameter leads to a high thermal effect on the sample. Since the laser peening technique without a protective coating is employed in this study, the use of the large spot diameter is avoided because this could damage the surface of the treated specimen. In addition, spot diameter determines the intensity of the applied laser energy per time and area. Therefore, a successful laser peening treatment without a protective coating can be achieved when operating with relatively low laser energy due to high laser intensities obtained from the small diameter.

Here, an imaging system consisting of three converging lenses A, B, and C, and pin-hole is given as shown in Fig. 3.6, which is expanded the optical system in Fig. 3.7.

Firstly, the beam from lens A that has a short focal length passing through the pin-hole is diverged. Secondly, the diverged beam is recollimated with a longer focal length.

Hence, larger beam waist and smaller divergence. The lenses are positioned like an inverted telescope

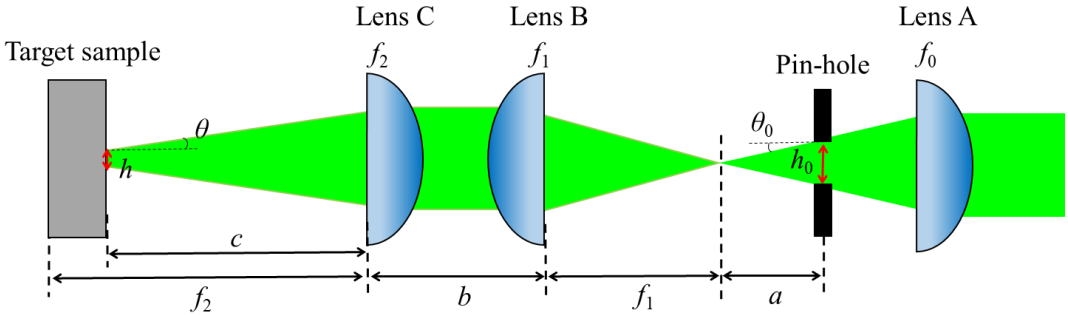

Figure 3.6 Imaging optical system

The ray direction goes from right to left. a is the distance from the pin-hole to the diverging point, b is the distance between lens B and lens C, and c is the distance between lens C and the target sample.

The laser beam was focused by a lens A and passed through the pin-hole. The image with a size of h_0 is formed. Since this image formation is in front of the focal point of the lens B, it is transferred in front of the focal point of the lens C. The focal lengths of lenses B and C are f_1 and f_2, respectively. θ and θ_0 are the slopes of the rays.

ABCD matrix can be utilized to describe a ray propagation through an optical element. The ray transfer matrix in Fig. 3.6 is

$$\begin{pmatrix} h_0 \\ \theta_0 \end{pmatrix} = \begin{bmatrix} 1 & a \\ 0 & 1 \end{bmatrix} \begin{bmatrix} 1 & f_1 \\ 0 & 1 \end{bmatrix} \begin{bmatrix} 1 & 0 \\ -\frac{1}{f_1} & 1 \end{bmatrix} \begin{bmatrix} 1 & b \\ 0 & 1 \end{bmatrix} \begin{bmatrix} 1 & 0 \\ -\frac{1}{f_2} & 1 \end{bmatrix} \begin{bmatrix} 1 & c \\ 0 & 1 \end{bmatrix} \begin{pmatrix} h \\ \theta \end{pmatrix} \tag{3.1}$$

$$\begin{pmatrix} A & B \\ C & D \end{pmatrix} = \begin{bmatrix} 1 & a \\ 0 & 1 \end{bmatrix} \begin{bmatrix} 1 & f_1 \\ 0 & 1 \end{bmatrix} \begin{bmatrix} 1 & 0 \\ -\frac{1}{f_1} & 1 \end{bmatrix} \begin{bmatrix} 1 & b \\ 0 & 1 \end{bmatrix} \begin{bmatrix} 1 & 0 \\ -\frac{1}{f_2} & 1 \end{bmatrix} \begin{bmatrix} 1 & c \\ 0 & 1 \end{bmatrix} \tag{3.2}$$

From Eqs. (3.1) and (2.2)

$$\begin{pmatrix} h_0 \\ \theta_0 \end{pmatrix} = \begin{pmatrix} A & B \\ C & D \end{pmatrix} \begin{pmatrix} h \\ \theta \end{pmatrix} \tag{3.3}$$

$$\begin{pmatrix} h \\ \theta \end{pmatrix} = \begin{pmatrix} \bar{A} & \bar{B} \\ \bar{C} & \bar{D} \end{pmatrix} \begin{pmatrix} h_0 \\ \theta_0 \end{pmatrix} \tag{3.4}$$

From Eq. (3.4), the image of spot diameter is given by

$$h = \bar{A}h_0 + \bar{B}\theta_0 \tag{3.5}$$

Since the diameter of the pinhole and the diameter of the laser beam are in an imaging relationship, the image can reach the sample surface regardless of the inclination of the light beam of the pinhole. Therefore, $\bar{B}$= 0.

$$h = \bar{A}h_0 \tag{3.6}$$

Therefore, the image transfer magnification m is

$$m = \frac{h}{h_0} = \bar{A} \tag{3.7}$$

The transfer magnification is adjusted to be 1⁄10 in this study. A laser beam having a spot diameter of 200 μm can be obtained by using a pin-hole with a diameter of 2 mm. The spot diameter was evaluated with a beam profiler. In addition, a part of the reflected light from the metal sample is transmitted through the dielectric multilayer mirror and imaged on the CCD camera so that the image of the focused spot can be confirmed.

3.2.4 Laser output beam profile

The design of the optical system described above makes it possible to control the laser output beam profile. The spot diameter of the imaged laser beam was measured with a beam profiler (manufactured by Ophir Japan). The second harmonic of the Nd: YAG laser (wavelength: 532 nm) was used as the laser light source. Figure 3.7 shows the spot diameter on the metal surface when a pinhole with a diameter of 2 mm is used. From Fig. 3.7, the spot diameter of the laser beam at the imaging position is estimated to be 200 μm, which is 1/10 times the pinhole diameter, and the spatial distribution of the laser is a flat top. A flat-top beam is more efficient as it surpasses the threshold while minimizing wasted energy by maintaining a constant irradiance value through a beam cross-section, thus providing a consistent intensity across the target of a laser system.

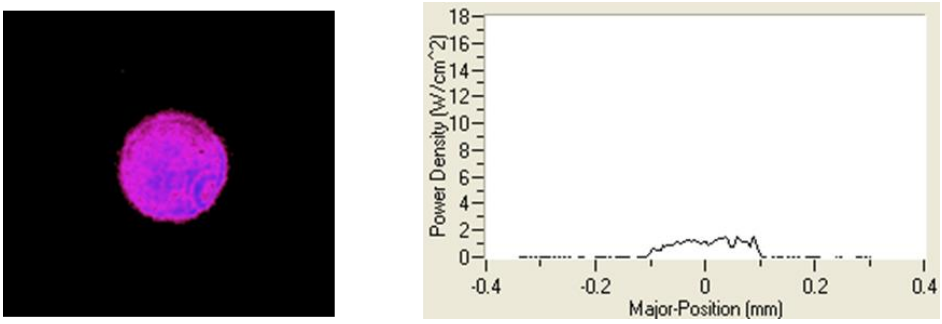

Figure 3.7 Laser output beam profile

3.3 Laser peening parameters

The laser peening process can be controlled by various parameters as shown in Fig. 3.8. Although this study focused on controlling the plasma confinement layer, other laser peening parameters such as laser wavelength, laser intensity, and coverage are also considered.

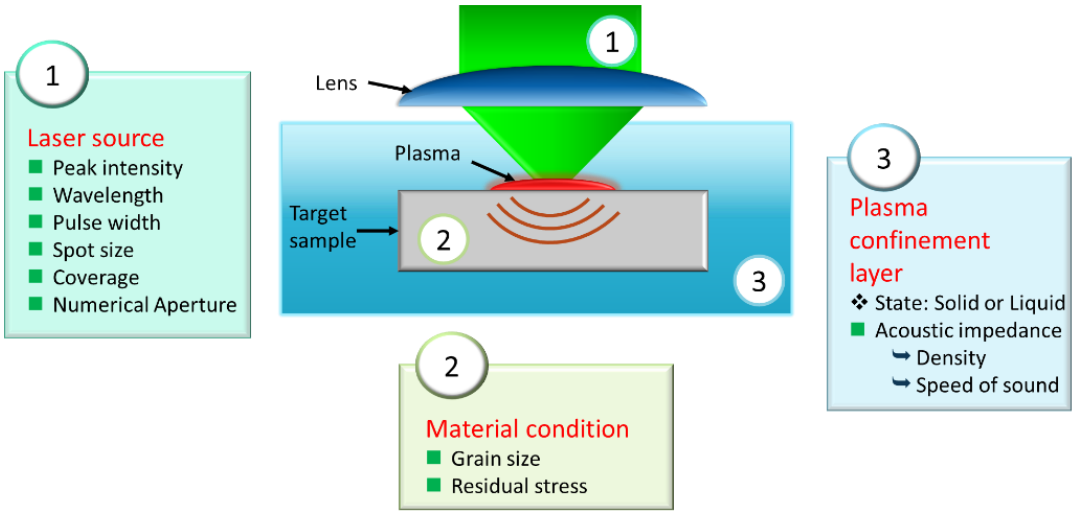

Figure 3.8 Laser peening parameters

3.3.1 Laser wavelength

In the laser peening process, a plasma confinement layer is used to constrain the high-pressure plasma. A plasma confinement layer with high transparency towards the laser beam is desirable because the transmissivity of the laser beam through the plasma confinement layer has a significant effect on the laser peening process. Generally, water is commonly used as a plasma confinement layer. Figure 3.9 shows the absorption of electromagnetic radiation by water across a wide wavelength range [40]. Water is transparent in the visible light but absorbs light in the near-infrared. This shows that the transmission of light through water can vary with wavelength. The fundamental (1064 nm) and second-harmonic (532 nm) wavelength were used for laser peening treatment in this study. The second harmonic wavelength has the lowest absorption in water, thus the laser peening treatment using this wavelength can be carried out without concerning the thickness of the water.

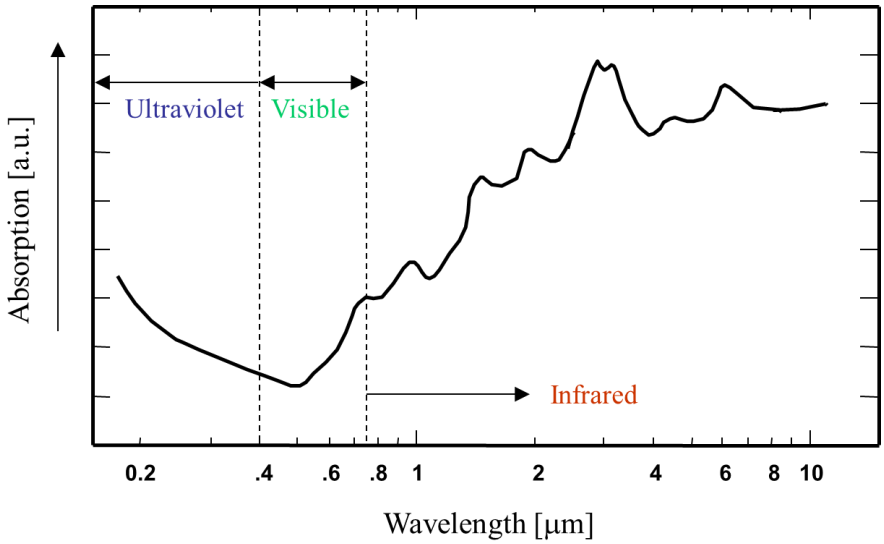

Figure 3.9 Absorption of electromagnetic radiation by water

On the other hand, the absorption of the specimen is also determined by the laser wavelength. The wavelength dependence of the absorption rate of different materials is shown in Fig. 3.10. As can be seen in Fig. 3.10, the absorption rate of metal varied with the wavelength. Since the transmittance and the absorption rate of the material differ depending on the wavelength, it is necessary to select the wavelength depending on the application for efficient laser peening.

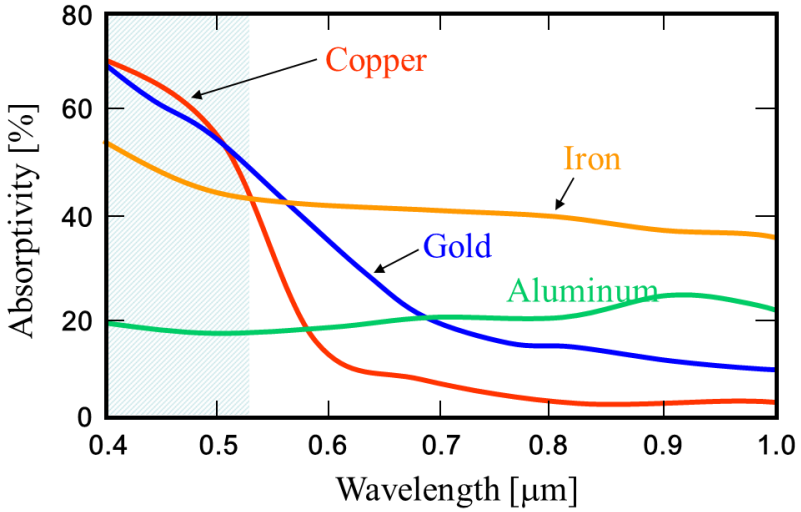

Figure 3.10 The absorption rate of common metals

3.3.2 Laser intensity, *I*

In the confined mode of the laser peening process, the laser intensity is one of the important factors that affect the magnitude of the peak pressure. Laser intensity, *I* is defined as the power per unit area delivered by the incident laser beam.

$$I = \frac{E \times 10^{-3}}{f \cdot (\tau_P \times 10^{-9}) \left(\frac{d}{2}\right)^2 \pi} \tag{3.8}$$

I: Laser intensity [W/cm^2]
E: Average laser output energy [J]
d: Spot size [cm]
τ_P: Pulse width [ns]
f: Frequency [Hz]

3.3.3 Coverage, C_V

Given the relatively small spot size, the amount of residual stress is not so high compared to the larger spot size. Considering this fact, the overlapping laser pulse technique was employed.

The coverage or overlapping rate C_V, which is the number of laser shots per unit area, was obtained by controlling the XY-stage with a computer to move the target sample in the x and y directions during laser irradiation as shown in Fig. 3.11. Here, $C_V = (\pi d^2/4) \cdot N/A \times 100$ [%], where d, N, and A represent the spot diameter of the irradiated laser pulse, number of pulses, and irradiated area, respectively.

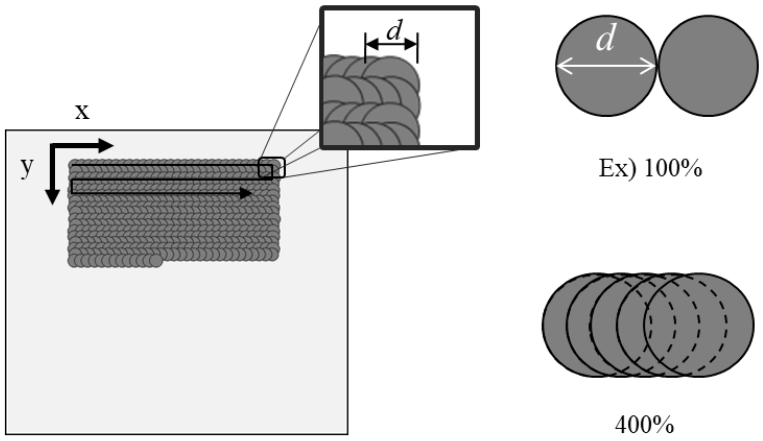

Figure 3.11 Schematic illustration of the scan direction of the laser pulses and pattern of the coverage

3.4 Methods to control plasma confinement layer

As discussed in Chapter 2, a plasma confinement layer having high acoustic impedance is desirable to increase the effectiveness of the laser peening effect. The acoustic impedance of the plasma confinement layer is determined by the product of the density and speed of sound in the medium. The amplitude of the peak pressure can be increased,

meanwhile, the pressure duration can be also significantly widened using a plasma confinement layer having a high acoustic impedance.

Instead of focusing more on the acoustic impedance of the plasma confinement layer, another approach has been taken. A systematic approach to control the plasma confinement layer has been described in this section. When using a liquid medium as a plasma confinement layer, three main parameters can be controlled: temperature, thickness, and liquid properties such as concentration and viscosity. It must be noted that the change in temperature and the liquid properties of the plasma confinement layer also influences its acoustic impedance.

3.4.1 Water temperature as an acoustic impedance control [41]

Water is commonly used as a plasma confinement layer during laser peening processing. It has been discovered that by controlling the temperature of the water, the acoustic impedance can also be controlled. This is because both the speed of sound and the density of water are highly temperature-dependent. The acoustic impedance of water at different temperatures ranging from 30 to 80 °C can be calculated using equation (2) based on data collected from the literature. Figure 3.12 shows the acoustic impedance as a function of water temperature and a peak at the temperature of around 60 °C can be seen.

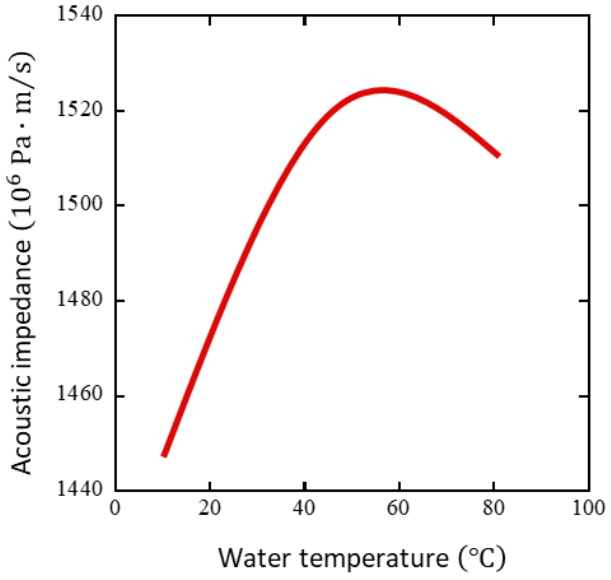

Figure 3.12 Relation between water temperature and acoustic impedance

3.4.2 Controlling the liquid properties of plasma confinement layer [42]

In the case of liquid properties, any kind of transparent liquid can be selected as a candidate for the plasma confinement layer. Glycerol solution was found to be effective as a plasma confinement layer due to higher acoustic impedance than water [22,43,44]. The

acoustic impedance of glycerol solution that depends on the density and sound velocity is controlled by varying its concentration. The acoustic impedance of the plasma confinement layer is calculated, then the relation that shows the acoustic impedance versus concentration of glycerol solution is presented in Fig. 3.13. Higher acoustic impedance can be obtained at a high concentration of glycerol solution. However, it must be noted that the viscosity in glycerol solutions increases as the concentration increases (see Fig. 3.14).

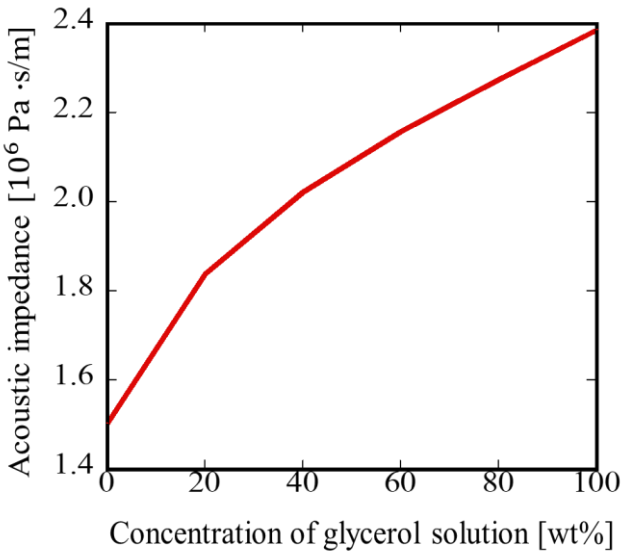

Figure 3.13 Acoustic impedance of glycerol solution as a function of concentration

In Fig. 3.15 the results of measurement of the transparency of glycerol solution at different concentrations were presented for laser wavelengths of 532 nm and 1064 nm. The measurements showed that the transparency of water (0 wt%) towards the laser radiation at the wavelength of 532 nm and 1064 nm are about 94 % and 84 %, respectively. Lower transparency is probably due to the higher absorption coefficient in water. In the case of laser wavelength of 532 nm, the increase in the concentration of glycerol solution does not affect its transparency towards laser radiation. However, at 1064 nm wavelength, a slight decrease in transparency can be seen when the concentration is increased. Therefore, a high concentration of glycerol solution was assumed to have a high absorption coefficient.

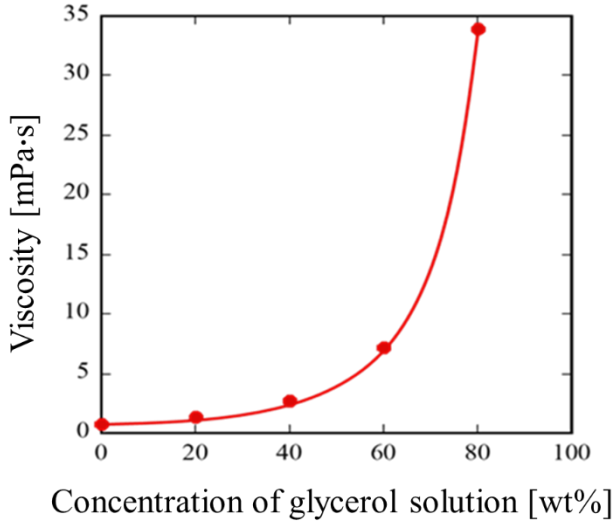

Figure 3.14 Viscosity of glycerol solution as a function of concentration

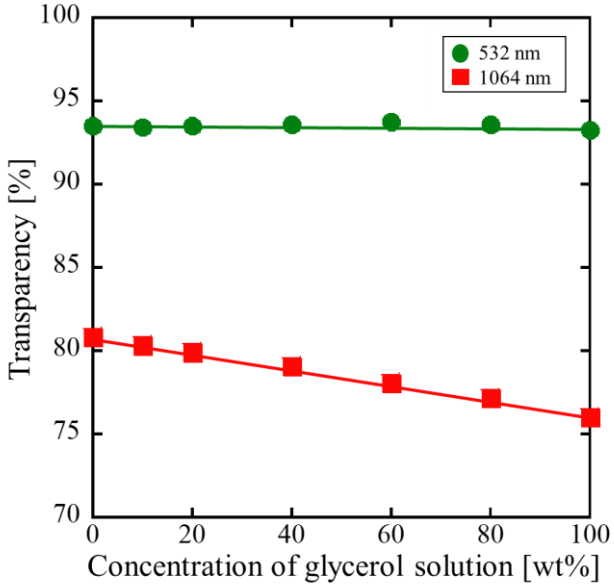

Figure 3.15 Transparency of glycerol solution as a function of concentration

3.5 High-speed imaging system

With a high-speed imaging system, it is possible to observe the phenomena occurring in the plasma confinement layer that takes place near the surface of the metal after laser irradiation. The phenomena near the metal surface were recorded with a Shimadzu high-speed video camera. An AF Micro-Nikkor 200 mm f/4D IF-ED was mounted on the camera (see Figure 3.16)

Figure 3.17 shows an arrangement of the high-speed imaging system. A stainless steel SUS316L was used as a target and immersed in a plasma confinement layer. The laser source was a Q-switched ND: YAG laser and the laser intensity was controlled by an

attenuator placed in the optical path. The focal spot diameter was fixed at 200 µm by adjusting the size of the pinhole.

Figure 3.16 High-speed video camera Shimadzu mounted with a lens having a focal length of 20 cm

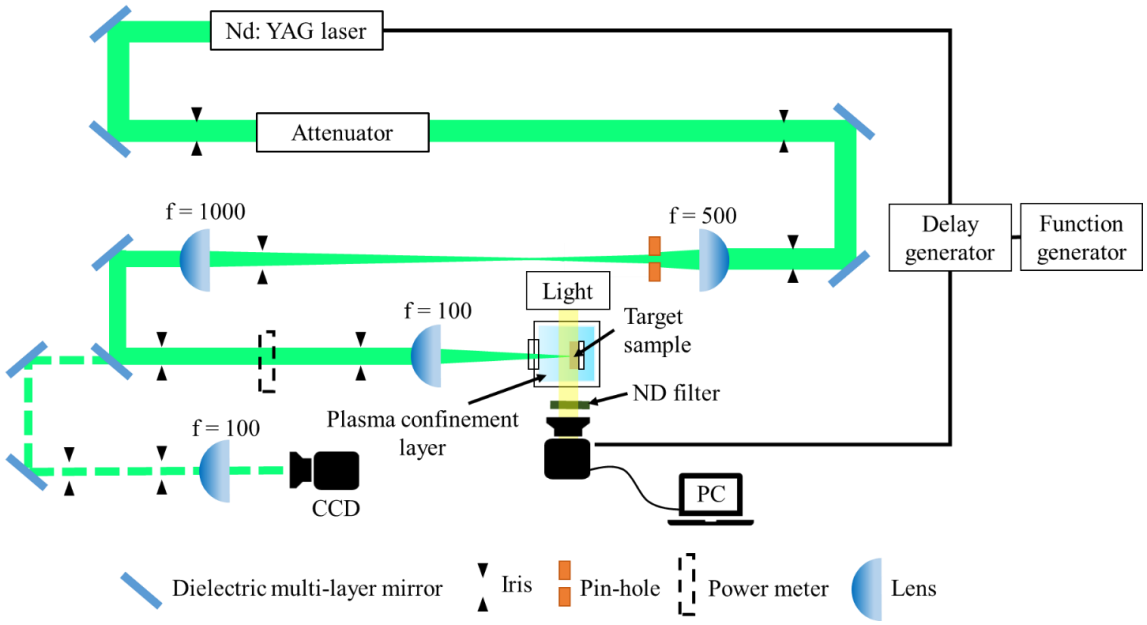

Figure 3.17 Optical arrangement for observing the phenomena occurs near the metal surface after laser irradiation

During imaging, a consistent light condition was maintained. A White LED flashlight (SparkLED LHA-SP431) is used as an illumination light for recording. The adjustment of the light intensity of the flashlight is required to capture the phenomena that occur near the metal in the range of milliseconds. To reduce or attenuate the light intensity,

a neutral density (ND) filter was installed in front of the high-speed camera. A function generator (Agilent 33250A) is used to control the timing of lighting light of the flash lamp manually by sending a signal to the delay generator (Model DG535) for generating a single-shot laser pulse, while a digital delay generator is used to provide delays for triggering the high-speed video camera.

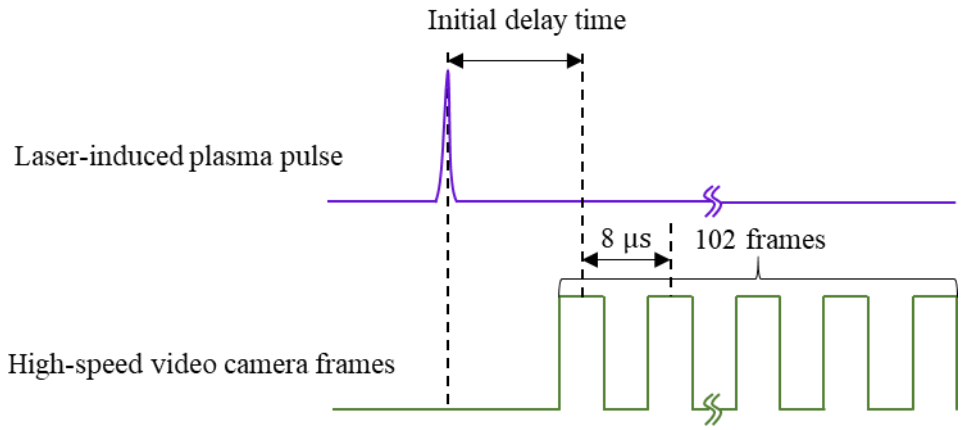

Figure 3.18 Timing chart for an imaging system (Shutter speed = 8 μs)

Figure 3.18 shows the timing chart for one experiment. For each laser pulse, 102 frames were captured in the high-speed video camera, and the total duration of images captured near the metal surface after laser irradiation depends on the shutter speed. The shutter speed can be adjusted depending on the desired range of time. For example, if the shutter speed is set to be 8 μs, the phenomena that occur near the metal surface in about 800 μs can be recorded. Therefore, the temporal resolution of the measurements is estimated to be 125000 fps.

3.6 Pressure measurement by using polyvinylidene fluoride (PVDF) gauge sensor

Many techniques have been used already to characterize the shock wave pressure [45]. Piezoelectric quartz, copolymers, electromagnetic gauges (EMV), or streak camera can be used for the measurements of a very high amplitude shock wave [23,46]. In this study, a very well-adapted instrument which is piezoelectric polyvinylidene fluoride (PVDF) gauge sensor is used to measure the shock wave pressure.

3.6.1 Basic principle of PVDF gauge

The piezoelectric effect of PVDF was first raised by Kawai in 1969 [47]. PVDF film is an appealing material for use as a sensing element in a piezoelectric stress gauge, which measures high dynamic pressure and delivers electrical charges when mechanical stress is applied [48]. When certain materials are subjected to mechanical stress, electrical

charges in response to the applied mechanical stress are generated. This effect is known as piezoelectricity.

PVDF is the sensors of selection for a wide range of measurement applications because they have useful characteristics: rapid response (~ns), large stress range, large signal to noise ratio, very thin, and simple circuitry. In this study, the impact pressure from the laser pulse was measured using a PVDF gauge (PVF2-11-.125-EK, Dynasen) as shown in Fig. 3.19. This gauge was constructed from 0.0011 inches thick, uni-axially stretched, and poled PVF_2 film with a copper electrode on each side. This layer is laminated between two sheets of polymer material using an epoxy lamination process. The measurement area which is also called as "active area" has an area of 10 mm^2 in area. The stress application range is around 10 MPa to 10 GPa.

Figure 3.19 PVDF gauge (PVF2-11-.125-EK, Dynasen)

3.6.2 Experimental setup for shock impulse measurement

The effectiveness of laser peening treatment can be estimated by measuring the magnitude of shock wave pressure induced by a pulsed laser. A process of laser peening treatment in a liquid confining medium leads to the formation of a laser-induced cavitation bubble on the surface of the metal. Some observations have revealed that when the bubble collapse, a strong shock wave is generated near the target. In this study, the magnitude of shock wave pressure was evaluated by measuring the shock impulse of laser-induced plasma and the collapse of cavitation bubbles generated by a single-shot pulse laser in a liquid confining medium. The experimental setup is shown in Fig. 3.20. The experiments were performed with a Nd: YAG laser and a similar optical arrangement as the laser peening treatment was applied. A SUS316L stainless steel sheet with a thickness of 0.05 mm was used as a target sample and glued on a polyvinylidene fluoride (PVDF) gauge sensor. The gauge sensor was connected to an oscilloscope (Tektronix DPO3034) via a charge integrator (CI-50-0.1 Dynasen Inc.). Each measurement was repeated more than five times under the same experimental conditions.

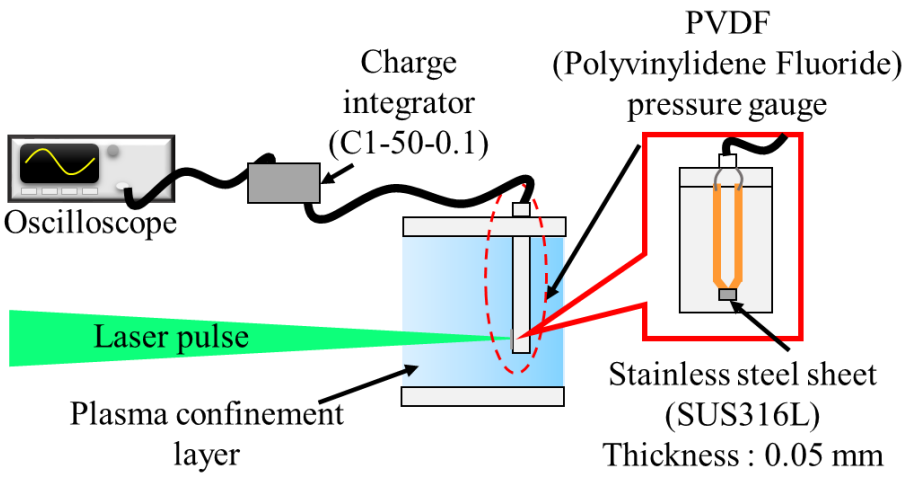

Figure 3.20 Schematic illustration of the experimental setup for shock impulse measurement

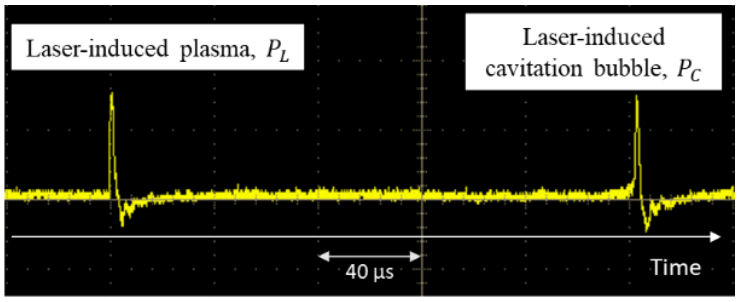

Figure 3.21 Shock wave signal from laser-induced plasma and the collapse of laser-induced cavitation bubble from PVDF gauge sensor

The output signal from the PVDF gauge sensor caused by the laser-induced plasma, P_L, and the collapse of cavitation bubble, P_C is shown in Fig. 3.21. The effects of laser peening are influenced by both shock impulses. Here, the shock impulses for both the laser-induced plasma and the cavitation bubble collapse can be determined simply by measuring the area under the curve of the peak pulse using Eq. (3.9).

$$Imp = \int_0^\infty F_{(t)}\,\mathrm{d}t \tag{3.9}$$

F is the force acting on the target in time-dependent and Imp is the shock impulse.

The signal from the PVDF gauge sensor was integrated in the charge integrator having a capacitance of 0.1 µF, then it was displayed by an oscilloscope with a 50 Ω load as shown in Fig. 3.22. The time constant was estimated to be several microseconds. Therefore, the shape of the pulses obtained is similar although the actual response time is different.

In addition, the time interval between peaks at various conditions of the plasma confinement layer was examined. The influences of the plasma confinement layer on the time interval were explained in the consideration section of every investigation.

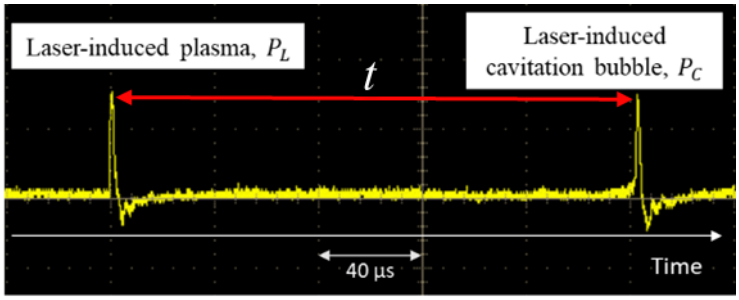

Figure 3.22 Time interval between peaks of laser-induced plasma and laser-induced cavitation bubble, t

3.7. Evaluation method on the plastic deformation after laser peening treatment

The evaluation on the plastic deformation on the surface of the material after laser peening treatment was carried out by measuring the surface hardness and residual stress via Vickers hardness test and x-ray diffraction method, respectively.

3.7.1 Vickers hardness test

Surface hardness is a very easy way to measure the material property that can readily be compared before and after surface treatment. Vickers hardness testing has been widely used for measuring the hardness of the metal [49]. It is the most universal method for determining the hardness of an object and can be used as a macrohardness tester or microhardness tester. Hardness test is easy to perform and requires little in the way of specimen preparation.

The Vickers hardness test is a test performed to measure the hardness of the treated samples. Figure 3.23 shows the schematic illustration of the Vickers hardness test. A square-based pyramid-shaped diamond with an angle of 136° at the vertex is pressed into the surface of the test piece using a prescribed force, F. The hardness is calculated from the size of an impression produced under load by a pyramid-shaped diamond indenter. The Vickers hardness number is the ratio of the load applied to the surface area of the indention. After the force has been removed, the two diagonal lengths of the indentation left in the surface of the material are measured under a microscope and the arithmetic means, d, is calculated with the following formula.

$$HV = \frac{2F}{d^2} \sin\frac{136^\circ}{2} = 1.854\frac{F}{d^2} \tag{3.10}$$

(*F* in kgf, *d* in mm)

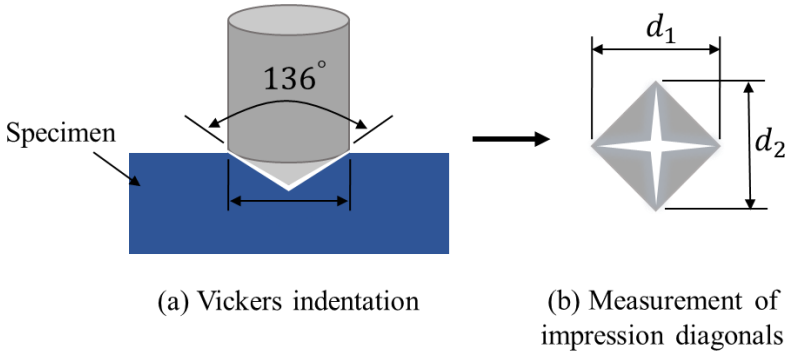

Figure 3.23 Schematic illustration of Vickers hardness test

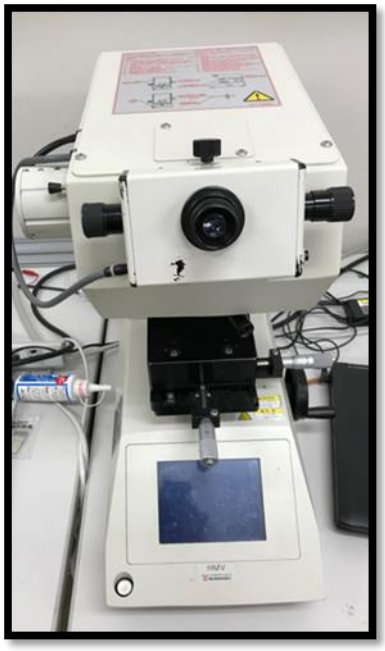

Figure 3.24 Vickers hardness tester

The hardness value is expressed as Vickers Hardness (HV). The smaller the indent left by the indenter at a defined test force in the surface of the specimen, the harder the tested material. The material investigated in this study is SUS316L stainless steel. Vickers hardness tester shown in Fig. 3.24 is used to measure the hardness of the material. To conduct the Vickers hardness test, the specimen is mounted on the specimen clamp to ensure the fixed position during the measurement, then placed at the tester from where it would make contact with the indenter. The selection of the load is made in inverse function to its hardness. The load is set to be 1.961 N (0.2 kgf). The load is applied for a time of 10 s. The internal software of the Vickers hardness tester automatically provides hardness calculations.

3.7.2 Residual stress measurement by X-ray diffraction

Residual stress can be defined as those stresses that remain in a body or material after processing in the absence of external forces or thermal gradients. The measured compressive residual stress induced during the laser peening is an important indicator of the effectiveness of the laser peening process. Compressive residual stress at the metal surface is often desired due to the positive effect on fatigue resistance because it impedes fatigue crack growth. When a laser peening treatment is performed on the metal, the crystal structure is plastically deformed due to the applied stress. The challenge in measuring residual stress is due to their hidden nature, but many reliable methods have been well established. There are two basic types of residual stress measurement. These are non-destructive and destructive methods. The non-destructive techniques can be carried out by using the X-ray diffraction (XRD) method. X-ray diffraction is the more common method, as X-rays are quite readily available.

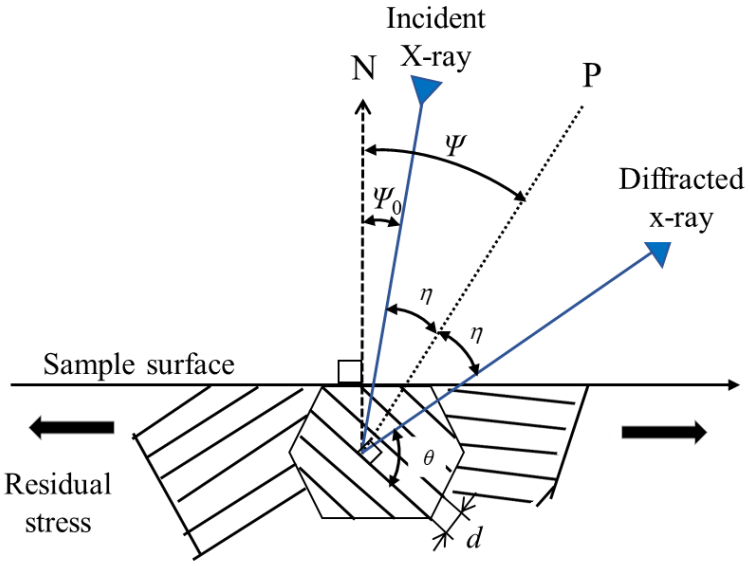

Figure 3.25 Schematic of crystal plane (*d*, lattice spacing of crystal plane, N, direction normal to the sample surface, P, Direction normal to diffracted crystal plane.

Figure 3.25 shows the schematic of crystal plane. As the X-rays hit the faces of the crystal, x-rays scatter in distinct patterns, which are sensed by a detector to be recorded for subsequent analysis. The incident beam diffracts X-ray from planes which satisfy Bragg's law given by

$$n\lambda = 2d \sin\theta \qquad (3.1)$$

where n is an integer denoting the order of diffraction, is the x-ray wavelength, d is the lattice spacing of crystal planes, and θ is the diffraction angle. A monochromatic beam of x-ray is incident on a sample and reflected x-ray are detected by a detector. The lattice spacing, d can be determined from the known wavelength and the measured diffraction angle. If the residual stresses exist within the sample, then the lattice spacing will be different than that of an unstressed state. This difference has the relation to the magnitude of the residual stress. Table 4 shows the measurement conditions used in this experiment. Cr-Kβ characteristic X-rays were used as the radiation source. The measurement was performed by irradiating a range of 5 mm × 5 mm with a laser and masking the area other than the measurement part.

Table 4 Measurement conditions of X-ray diffraction

Characteristic X-ray	Cr
Tube voltage (kV)	40.0
Tube current (mA)	35.0
Scan range (deg)	144.0-153.0
Scanning step (deg)	0.10
Counting time (s)	1.0
Diffraction plane	γ-Fe 311
Diffraction angle (deg)	148.5
ψ (deg)	0, 18.4, 26.6, 33.2, 39.2, 45.0

Electro-polishing is one of the necessary surface removals to measure the residual stress as a function of depth. To obtain depth profiles, the surface of the sample was removed by electropolishing. This process was repeated after each measurement.

Chapter 4: Experimental results and discussion

4.1. Effects of controlling the temperature of the water on laser peening

As mentioned in section 3.4 of Chapter 3, the acoustic impedance of water can be controlled by controlling its temperature. The investigation on the effects of controlling the temperature of the plasma confinement layer was conducted and described in this section.

4.1.1. Overview

Nd: YAG laser was operated at a wavelength of 532 nm with a pulse width of 4 ns. Laser peening treatment was conducted from high to low temperature. Therefore, a silicone rubber heater was required to control the temperature during the peening process. It was placed under the peening cell which was designed specifically for heat conduction by attaching a metallic surface at the bottom of the peening cell to control the water temperature (see Fig. 3.5). The temperature of the silicone rubber heater was adjusted manually by increasing or decreasing the current from the power source that connected to the silicon rubber heater. The thickness of the plasma confinement layer was fixed to be 20 mm. To investigate the effect of controlling the acoustic impedance of water on laser peening, experiments were carried out by varying the water temperature in the range of 30 to 80 °C.

4.1.2 Evaluation on plastic deformation after laser peening treatment

Figure 4.1 shows the hardness difference of metal surface as a function of water temperature. Hardness difference is defined as the difference between the hardness on the peened surface and the surface before laser peening. The coverage and laser intensity were set to be 900% and 3 GW/cm^2, respectively. The hardness increases with temperature from 0 to 60 °C, reach a maximum at about 60 °C, and then decrease with the further increase of temperature to 80 °C. Maximum hardness of about 108 HV was obtained. An increase in surface hardness has been attributed to plastic deformation resulting in dislocation multiplication and movement. By controlling the acoustic impedance of the plasma confinement layer, an effective laser peening treatment can be achieved.

To evaluate the residual stress induced on the surface of the metal, laser peening treatment was performed on the stainless steel under the same conditions used to measure the surface hardness. Fig. 4.2 shows the residual stress as a function of water temperature. The residual stress was measured non-destructively by X-ray diffraction. A negative value of residual stress indicates compressive residual stress. The compressive residual stress increases as the temperature increases. At a temperature of about 60 °C, the highest compressive residual stress of about -300 MPa was obtained on the surface of the treated sample. The high value of acoustic impedance at 60 °C as shown in Fig. 3.12 proved to be the reason for an increase in the compressive residual stress.

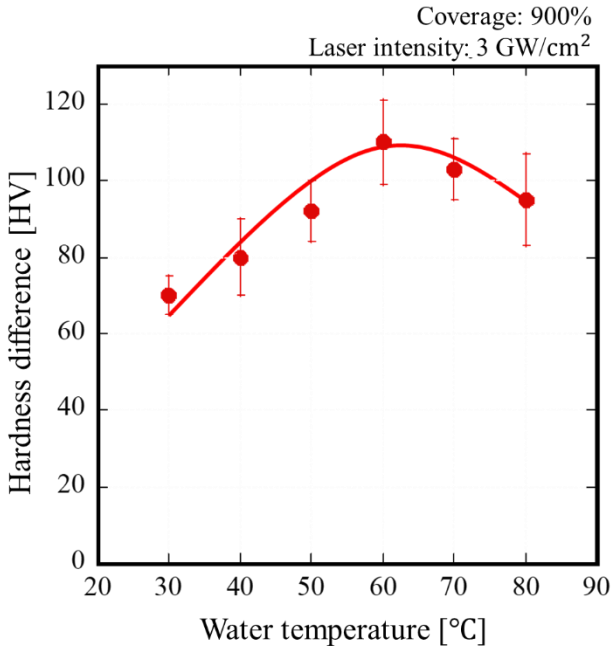

Figure 4.1 Hardness difference as a function of water temperature

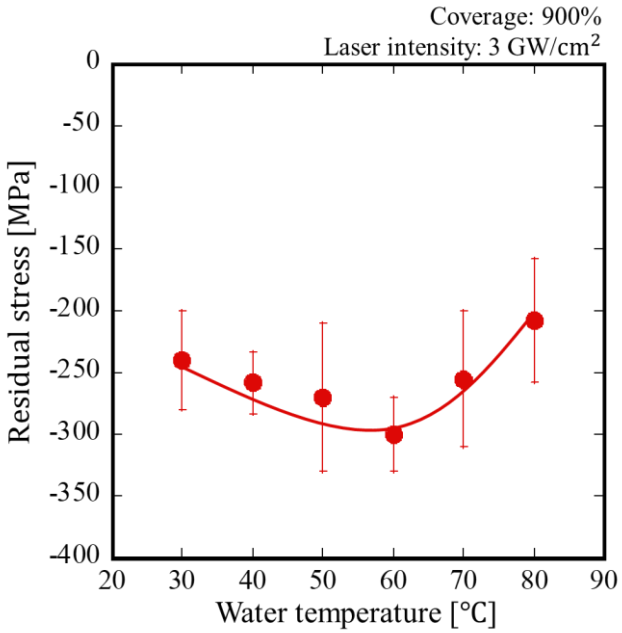

Figure 4.2 Residual stress on the surface of the metal as a function of water temperature

As shown in Figs. 4.1 and 4.2, the results on surface hardness and compressive residual stress exhibit the same trend as the acoustic impedance shown in Fig. 3.12. High surface hardness and compressive residual stress values were obtained around 60 °C. This shows that an increase in the acoustic impedance of plasma confinement results in an

increased ability to suppress the expansion of laser-produced plasma from rapidly expanding away to the surrounding. Thus, a high magnitude of shock wave pressure propagates into the target metal, enhancing the mechanical properties of the metal.

The influence of laser intensity and coverage on surface hardness at 30 °C and 60 °C were investigated. Figure 4.3 shows the hardness difference as a function of laser intensity. In this case, the coverage was set to be 900%. A high magnitude of surface hardness was obtained at a temperature of around 60 °C. The surface hardness increases when the laser intensity is increased up to 3 GW/cm^2 for both temperatures. It should be noted that the peak pressure of laser-induced plasma in confined mode is proportional to the square root of the laser intensity. This might explain the increase in surface hardness. However, the surface hardness saturates when the laser intensity exceeds approximately 3 GW/cm^2 due to the laser-induced breakdown of the water, which limits the energy delivered to the metal surface [6]. Here, if the laser intensity exceeds the threshold of the laser-induced breakdown, the laser light does not reach the metal surface.

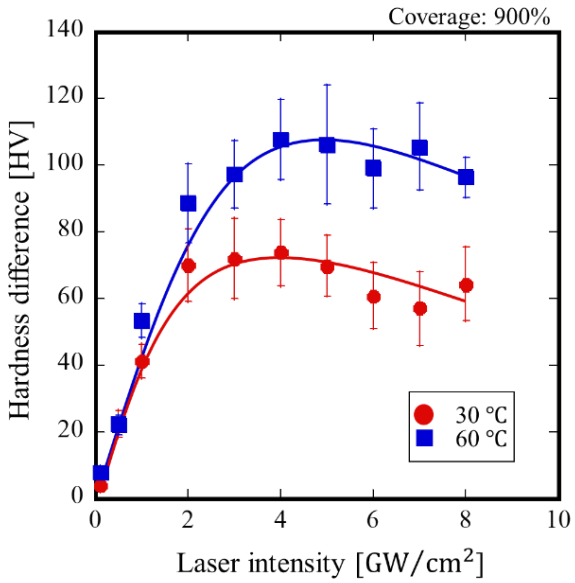

Figure 4.3 Hardness difference as a function of laser intensity at 30 °C and 60 °C

For hardness difference as a function of coverage, the laser peening treatment was performed by adjusting the laser intensity to 2 GW/cm^2. The results on surface hardness at the both cases of 30 °C and 60 °C were shown in Fig. 4.4. The surface hardness obtained at 60 °C is higher compared to 30 °C. It can be seen that the surface hardness increases when the coverage is increased up to 1200% for both temperatures. By increasing the coverage which is also increasing the number of shots on the treated area, the surface hardness can be increased. The hardness should increase proportionally to the coverage. In addition, Tsuyama et al. has reported that a high magnitude of compressive residual stress in the material can

also be obtained [50]. However, when the coverage is more than 1200%, the surface hardness saturates. This is due to the heat accumulation that can lead to oxidization and melting. Therefore, the hardness is no longer proportional to the coverage.

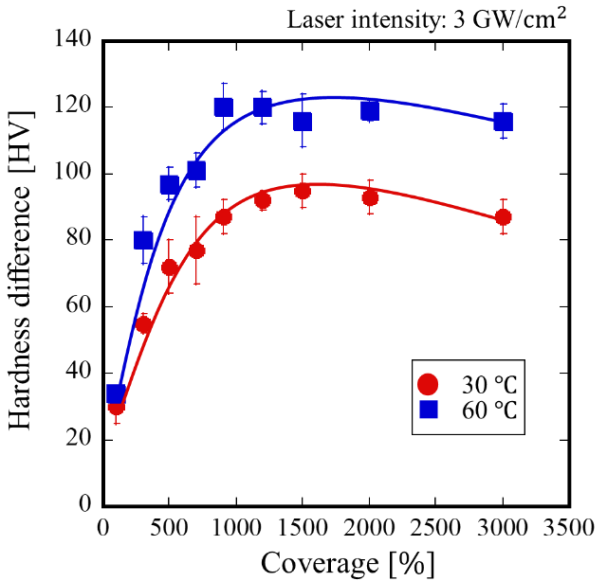

Figure 4.4 Hardness difference as a function of coverage at 30 °C and 60 °C

4.1.3 Consideration on shock impulses

The shock impulses generated from the confinement of the laser-induced plasma and the collapse of the laser-induced cavitation bubble were measured by using the shock impulse measurement described in Section 3.6.2 of Chapter 3. The collapse of the laser-induced cavitation bubble contributes to the higher magnitude of shock impulse compared to the laser-induced plasma. The characteristic of the shock impulse from the collapse of the laser-induced cavitation bubble has an almost similar trend as that of the shock impulse produced by the laser-induced plasma. This is probably attributed to the laser energy absorbed by the plasma generated on the surface of the metal.

Liu et al. [51] has studied the effect of temperature on the dynamics of the laser-induced cavitation bubble. They measure the growth and collapse of the cavitation bubble by using two fiber-optic sensors based on optical beam deflection (OBD). The signal amplitude of the impacts generated from the laser-induced plasma and the collapse the of cavitation bubble reach a maximum at the temperature of about 50 °C. It was said that when the water temperature is low, the gas content in the water is high, which acts as a cushioning effect, and the result is that the bubble collapse velocity is decreased. When the temperature is increased, the cushioning effect is decreased due to the reduction of gas content, thus increasing the impact force.

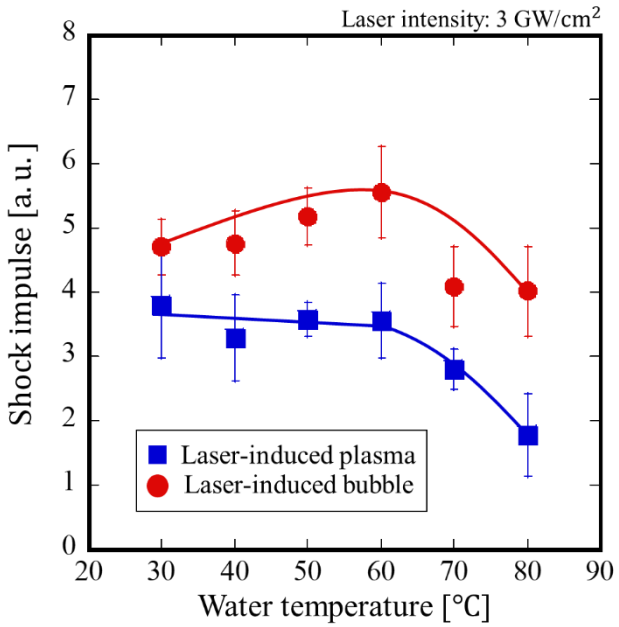

Figure 4.5 Shock impulse of laser-induced plasma and laser-induced cavitation bubble as a function of water temperature

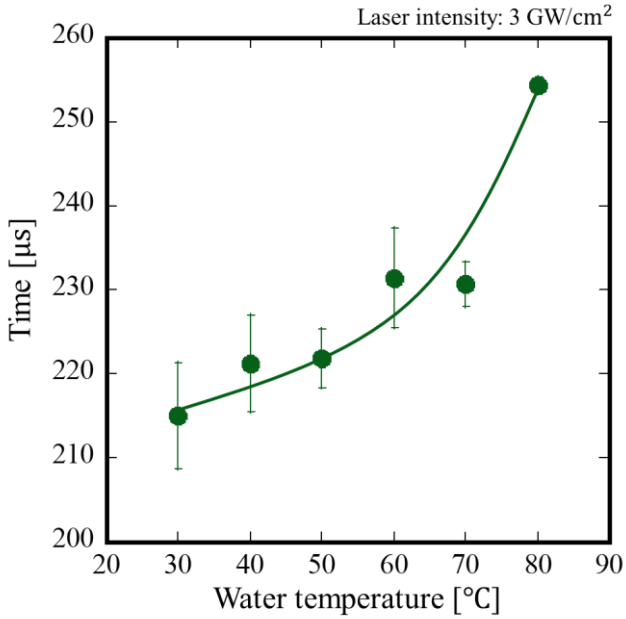

Figure 4.6 Time interval between peaks of laser-induced plasma and laser-induced cavitation bubble as a function of water temperature

The time interval between peaks of laser-induced plasma and laser-induced cavitation bubble was considered to investigate the dynamics of the cavitation bubble when the temperature of the water was increased. The data obtained based on the measurement of

the time interval has been plotted and presented in Fig. 4.6. The time interval between peaks of laser-induced plasma and laser-induced cavitation bubble indicates the developing time of laser-induced cavitation bubble. It can be suggested that the size of the cavitation bubble increases in time at high temperature due to higher vapor pressure inside the bubble an the decreases of the viscosity of plasma confinement layer. Although the size of the cavitation bubble is expected to be largest at 80 °C, the results from the shock impulse measurement show that the shock impulse decreases when the temperature is more than 60 °C. This is probably due to the changes in both external compression pressure and the internal cushion that affects the intensity of the bubble collapse [52]. Therefore, desirable temperature of the water is required to obtain large shock impact, thus enhance the efficacy of the laser peening treatment.

4.1.4 Summary

This study has provided a new technique to control the acoustic impedance by controlling the water temperature. Hence, warm water with a temperature around 60 °C was found to be effective to improve the mechanical performance of stainless steel. In addition, the optimization of laser intensity and coverage is required to realize efficient laser peening treatment. Proper estimation of the effectiveness of the laser peening process by controlling the temperature of the water can be determined by shock impulses generated from both laser-induced plasma and cavitation bubble. A simple and new approach demonstrated in this work will pave a way for laser peening technology to a wide range of new applications.

Section 4.1 of this dissertation, in part, is a reprint of the material as it appears in "Water temperature as acoustic impedance control for efficient laser peening". Optik, 2021, 242:167097. This work was co-authored by Akihiro Hata, Miho Tsuyama, Manabu Heya, and Hitoshi Nakano. The dissertation author is the first author of this work.

4.2 Effects of controlling liquid properties of glycerol solution on laser peening

Most previous studies on laser peening have employed water as the plasma confinement layer. In this experiment, a glycerol solution having higher acoustic impedance than water was selected as the plasma confinement layer to suppress the laser-induced plasma from rapidly expanding away from the surface. In this section, the results obtained from the investigation on the effects of controlling liquid properties of glycerol solution towards laser peening have been studied.

4.2.1 Overview

The effects of controlling liquid properties of glycerol solution on laser peening have been extensively investigated. Nd: YAG laser with wavelength 532 nm and 4 ns pulse

width was used and the experimental setup including optical arrangement as explained in Section 3.2 was adopted. The thickness of the plasma confinement layer was fixed to be 20 mm. The study in this section is described as follows. First, laser peening treatment was performed on stainless steel by changing various parameters, then the plastic deformation that occurred on the surface of the metal is evaluated. Second, the shock impulses of laser-induced plasma and laser-induced cavitation bubble generated from the single-shot laser pulse were measured to investigate the effect of liquid properties on the effectiveness of laser peening. Lastly, the dynamics of the laser-induced cavitation bubble in various concentrations of glycerol solution were observed to help better understand.

4.2.2 Evaluation on plastic deformation after laser peening treatment

Figure 4.7 shows the hardness difference of metal surface as a function of concentration at different coverages. The hardness difference is defined as the increase in surface hardness in the laser-peened area from its initial hardness. The laser intensity was set to be 2 GW/cm^2. The data plotted at 0 wt% concentration is the result on the hardness of metal surface after laser peening treatment in water. The highest value of metal hardness is about 98 HV at 900% coverage in a 20 wt% concentration of glycerol solution. When the concentration is increased up to 20 wt%, the metal hardness increases for all coverages. However, the metal hardness decreases when the concentration is more than 20 wt%. This is most likely due to the concentration of glycerol solution which influences its viscosity. The lower value of metal hardness obtained in glycerol solution compared to water indicates that a high concentration is not effective for laser peening treatment. However, according to the results shown in Fig. 4.7, by increasing the coverage from 100% to 900%, the metal hardness can be increased at any concentrations. From this result, it can be seen that the coverage does not strongly influence by the concentration of the glycerol solution. Hence, an increase in coverage from 100% to 900% resulted in an increase in metal hardness due to a large number of laser pulses applied on the surface.

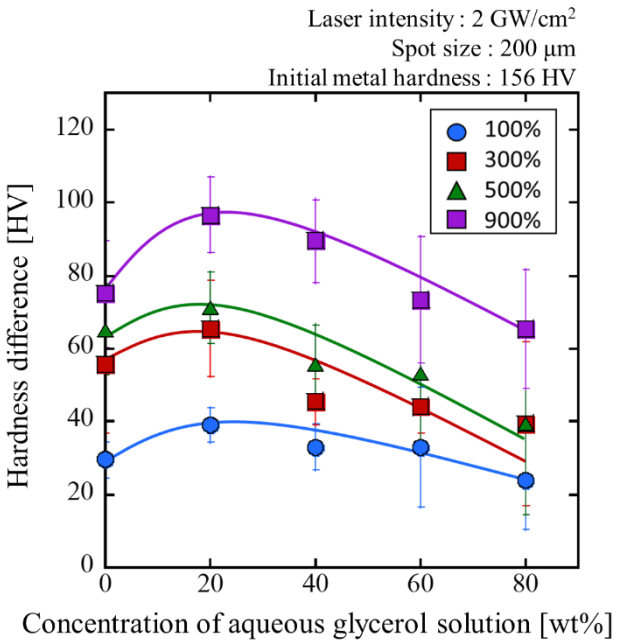

Figure 4.7 Hardness difference as a function of concentration of glycerol solution at different coverage

The cause for the decrease in hardness at high concentration was investigated. Figure 4.8 shows the image of the laser-peened surface at all concentrations of glycerol solution. The coverage and laser intensity were fixed at 900% and 2 GW/cm^2, respectively. As the concentration increases, the change in the overlapping dents pattern can be seen. At low concentration, a uniform overlapping dents pattern was obtained on the peened surface. However, an uneven overlapping dents pattern was obtained at a high concentration of about 80 wt%. This demonstrates that the laser beam cannot reach the metal surface successfully, thus resulting in a decrease of hardness.

Tsuyama et al. has mentioned that the reason for the ineffective laser peening treatment performing under a high concentration of plasmas confinement layer was the presence of a small cavitation bubble that interrupts the path of the laser beam [44]. It should be noted that, after the first cavitation bubble collapsed, a new bubble was generated, expanded, shrank, and collapsed. This process continues until the bubble splits into small bubbles that remain spherical if steady-state condition. When the cavitation bubble is in a steady-state, two situations can happen. In the low concentration of plasma confinement layer, the small bubble rises towards the surface of confining medium. As a result, the laser beam can successfully reach the metal's surface (see Fig. 4.9(a)). However, in a high concentration of plasma confinement layer, the small bubble tends to stay on the peened surface for a long time because the rising speed becomes extremely slow due to high viscosity (see Fig. 4.9(b)). Therefore, at high concentrations, laser peening treatment is not

effective due to the presence of the small bubbles that remain on the optical path of the laser beam, thus causing the laser beam to scatter and refract.

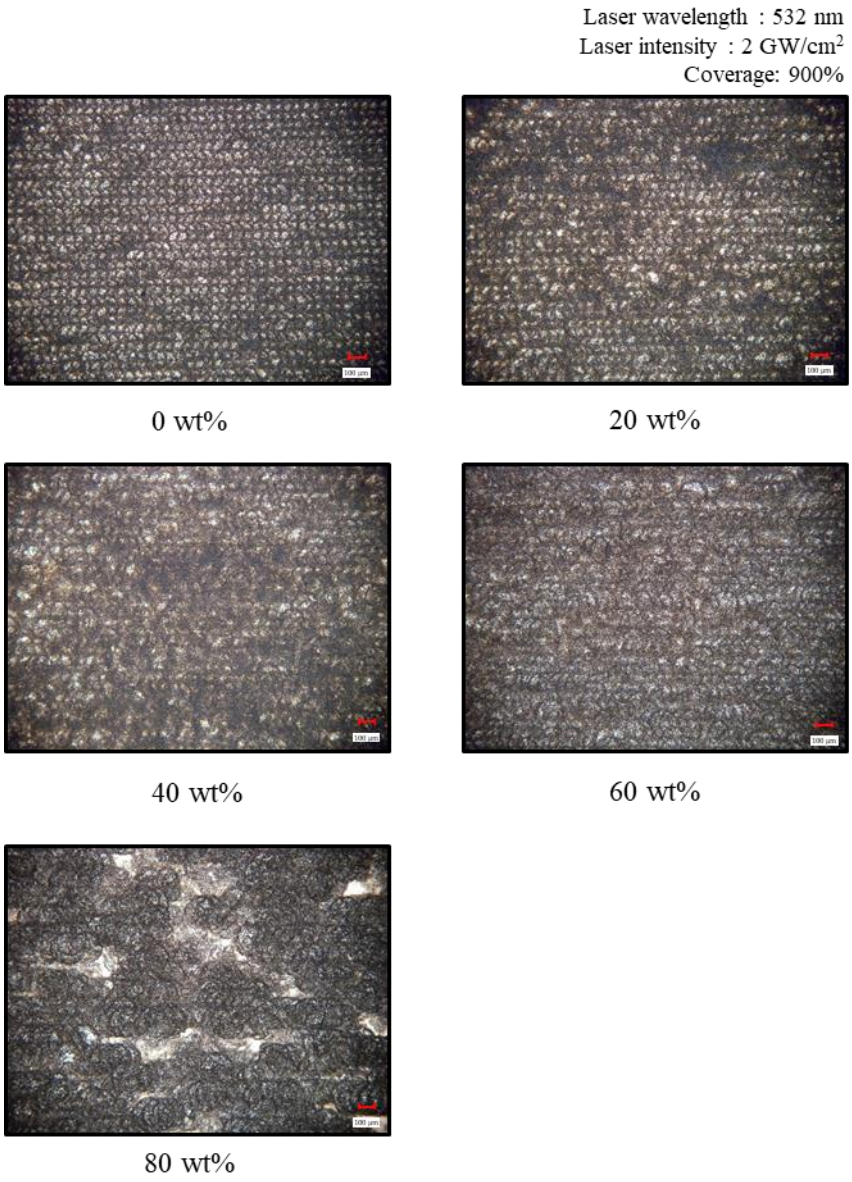

Figure 4.8 Laser-peened surface at various concentrations of glycerol solution

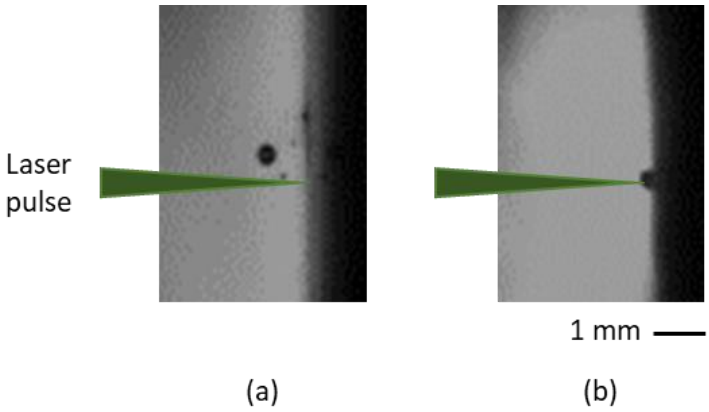

Figure 4.9 Shadowgraph of small cavitation bubble at captured by a high-speed camera at 100 (a) 20 wt%, (b) 80 wt%

Based on the results obtained on the hardness of metal's surface, laser peening performed in 20 wt% concentration of aqueous glycerol solution was found to be effective. Here, laser peening treatment was performed in water and 20 wt% concentration of aqueous glycerol solution for comparison. The laser intensity and coverage were set to be 2 GW/cm^2 and 900%, respectively. The residual stress of the target sample on the peened surface was characterized using the X-ray diffraction method. The degree of laser peening effect can be determined by evaluating the residual stress in-depth direction. The depth profiles were obtained through the repeated cycles of electropolishing to remove the surface layer. Figure 4.10 shows the residual stress introduced by laser peening in water and aqueous glycerol solutions with a 20 wt% concentration as a function of depth. The residual stresses obtained from the surface of the metal until 140 μm in depth were compared. A positive and negative value of residual stress in Fig. 4.10 denote tensile and compressive residual stress, respectively. Tensile stress was detected on the surface of the target metal (depth=0 μm) in both plasma confinement layers. When the depth is increased, the residual stress changed from tensile to compressive residual stress in both the plasma confinement layers. The highest value of compressive residual stress at a depth of approximately 10–40 μm under the metal surface was obtained in 20 wt% aqueous glycerol solution owing to the high acoustic impedance. The high acoustic impedance of the plasma confinement layer contributes to an increase in the intensity of the shock wave pressure, thus enhancing the laser peening effect. A plasma confinement layer with high acoustic impedance is preferable for obtaining high residual stress.

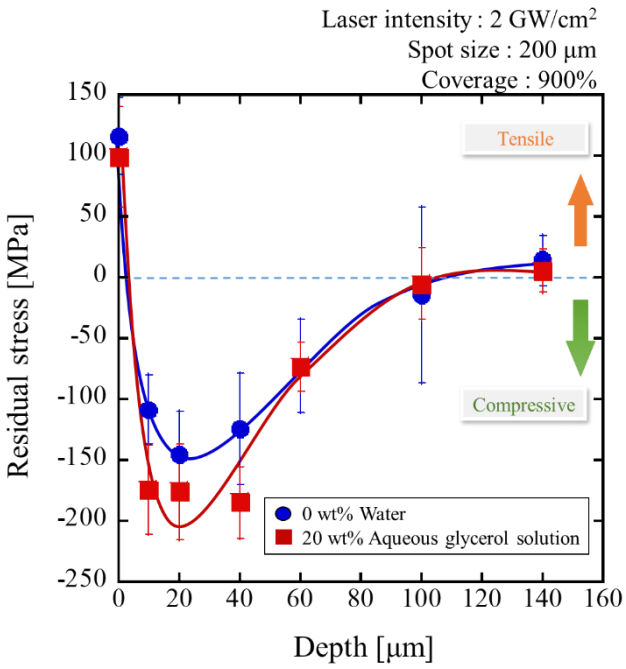

Figure 4.10 Residual stress as a function of depth in water and 20 wt% concentration of aqueous glycerol solution

An aqueous glycerol solution of around 20 wt% in concentration is desirable for obtaining high metal hardness. The effect of the laser intensity on the metal hardness was investigated using a 20 wt% aqueous glycerol solution. The hardness difference as a function of laser intensity is shown in Fig. 11. Based on Eq. (2.2), the peak pressure is proportional to the laser intensity. The results obtained in this study demonstrate that the metal hardness is almost proportional to the laser intensity up to 4 GW/cm^2. The metal hardness increases owing to work hardening caused by the high shock wave pressure impact-induced inside the metal surface. However, the linear relationship between the laser intensity and metal hardness does not exist beyond a laser intensity of approximately 4 GW/cm^2 because laser-induced breakdown occurs, which limits the energy delivered to the metal surface [5]. Thus, a desirable laser intensity exists for effective laser peening treatment.

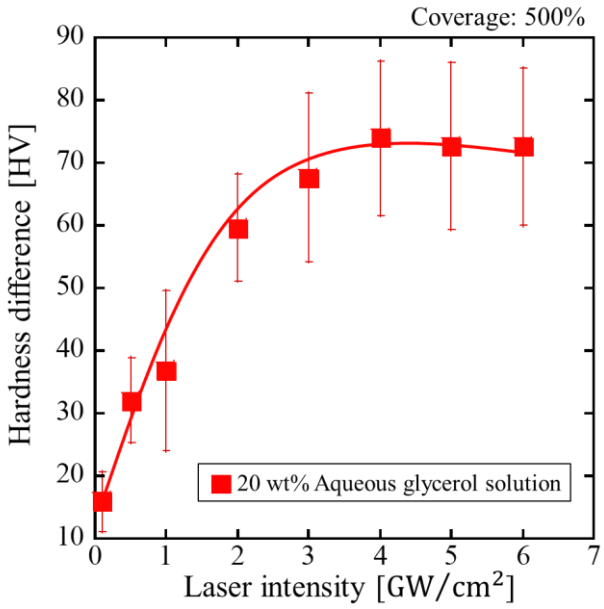

Figure 4.11 Hardness difference as a function of laser intensity in 20 wt% aqueous glycerol solution

4.2.3 Consideration on shock impulses and dynamics of laser-induced cavitation bubble

Further evaluation was performed by measuring the shock impulses via the PVDF gauge sensor as described in Section 3.6.2 of Chapter 3. The shock impulses were determined by the forces acting on the target for some amount of time that generated from the confinement of the laser-induced plasma and the collapse of the cavitation bubble. The laser intensity and spot size were fixed at 2 GW/cm^2 and 200 μm, respectively. Figure 4.12 shows the shock impulse of laser-induced plasma, that is, P_L, as a function of the concentration of the aqueous glycerol solution. A peak at approximately 20 wt% concentration can be observed. The shock impulse of laser-induced plasma was expected to increase when the concentration is increased due to an increase in acoustic impedance. However, the results obtained are opposite to what can be expected theoretically. More theoretical work is probably required to fully comprehend these findings.

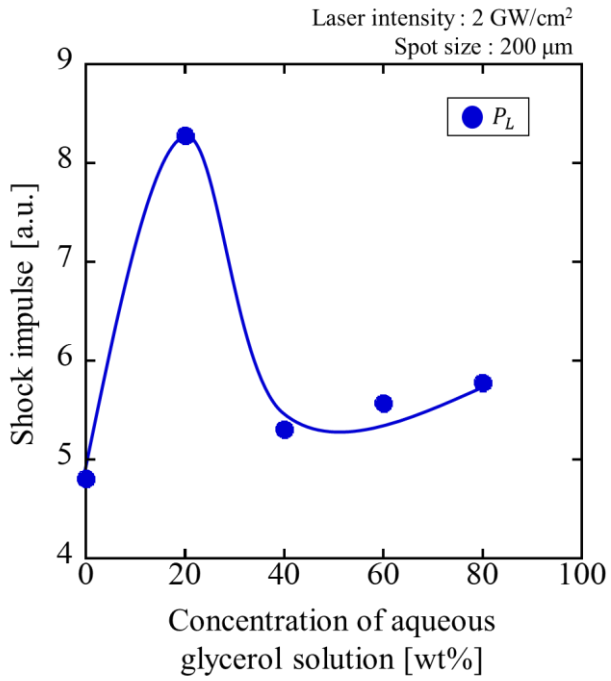

Figure 4.12 Shock impulse of laser-induced plasma as a function of concentration glycerol solution

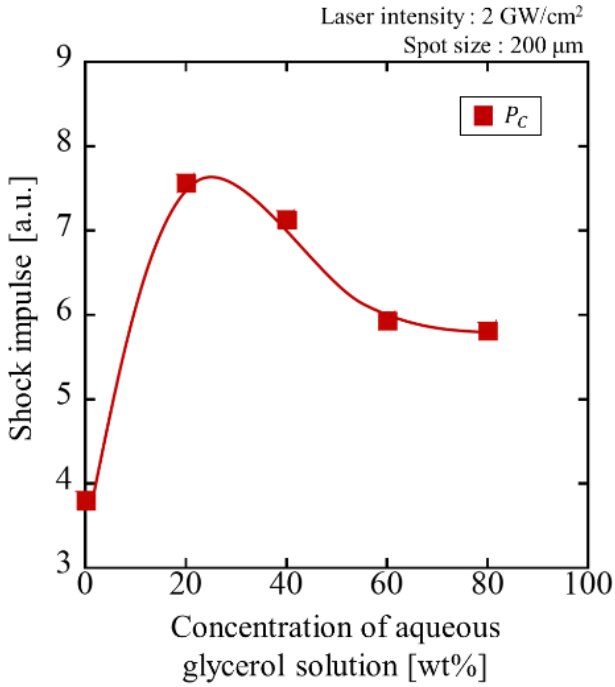

Figure 4.13 Shock impulse of laser-induced cavitation bubble as a function of concentration of glycerol solution

During the investigation on the shock impulses, more attention was given to the mechanisms of the laser-induced cavitation bubble. Some researchers have reported that the

collapse of the first cavitation bubble is effective for underwater laser peening and a series of experiments was applied to study its mechanism [29,53]. Therefore, the shock impulse from the collapse of the first cavitation bubble was considered. Figure 4.13 shows the shock impulse of the laser-induced cavitation bubble, that is, P_C, as a function of the concentration of the aqueous glycerol solution. The shock impulse by cavitation bubble showed the maximum value when the concentration was 20 wt%. However, the shock impulse became weaker as the concentration of the aqueous glycerol solution increased from 20 to 80 wt%. Liu et al. has investigated the dependence of laser-induced cavitation bubbles near a rigid on liquid viscosity by using a fiber-coupling optical beam deflection. They concluded that a high viscosity reduces the liquid-jet impact force and cavitation erosion [54]. This shows that besides the presence of a small bubble that interrupts the laser beam, the weak shock impulse emitted from the collapse of the first cavitation bubble is the cause for ineffective laser peening at high concentration due to high viscosity. Properties of the liquid have a great influence on the shock impulse generated from the collapse of the laser-induced cavitation bubble. Therefore, a low concentration is desirable to obtain a high magnitude of shock impulse.

The time interval between the peaks of laser-induced plasma and the collapse of laser-induced cavitation bubble at various concentrations of aqueous glycerol solution was measured and the results were presented in Fig. 4.14. Based on the results obtained, the longest time was found to be in 20 wt% concentration. When the concentration is increased from 20 wt% to 80 wt%, the developing time decreases. It is reasonable that the bubble size tended to decrease with concentration due to the viscous impact that acts on the bubble, thus a shorter time to collapse. In the case of water (0 wt%), a shorter time interval was obtained compared to the 20 wt% concentration. This could be due to the smaller size of cavitation bubble generated on the metal surface. The time interval has a strong relationship with the developing time of laser-induced cavitation bubble. Therefore, from this data, the developing time of the laser-induced cavitation bubble is proportional to the shock impulse of P_C.

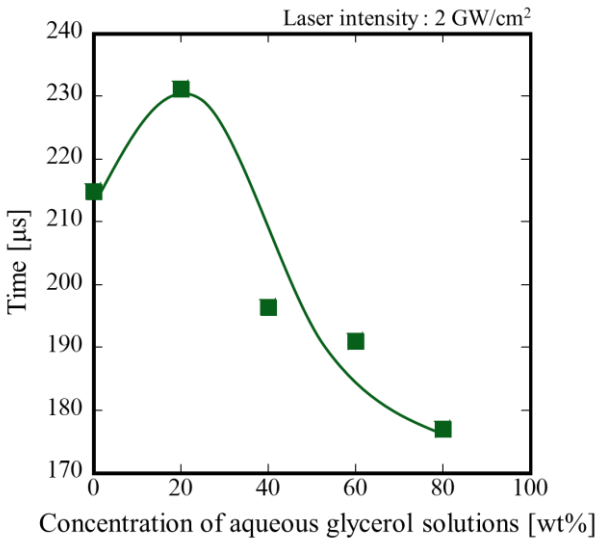

Figure 4.14 Time difference between peaks of laser-induced plasma and laser-induced cavitation bubble as a function of concentration of glycerol solution at 532 nm wavelength

The dynamics of a laser-induced cavitation bubble when the laser intensity is 2 GW/cm^2 has been observed by using a high-speed video camera to have a better understanding of the phenomenon that occurs near the metal surface in different liquid properties. The shutter speed was set to be 8 μs. Figure 4.15 shows the time evolution of laser-induced cavitation bubble after laser radiates on the metal surface. The first frame at 8 μs shows the laser radiates on the metal's surface. Due to the pressure induction and energy deposited on the metal surface, a laser-induced cavitation bubble in a hemispherical shape is formed. The high pressure within the cavitation bubble causes it to expand outward until it reaches its maximum size. Then, the cavitation bubble shrinks due to the imbalance between internal bubble pressure and ambient pressure. After that, a shrinking process occurs on the cavitation bubble and the bubble collapse.

The size of the laser-induced cavitation bubble qualitatively appears smaller when the concentration is increased. The maximum diameter of the cavitation bubble at different concentrations was measured and plotted as a function of time (see Fig. 4.16). A maximum diameter of about 2.6, 2.4, 2, and 1.6 mm were obtained at 20, 40, 60, and 80 wt% concentrations, respectively. A decrease in the diameter of the cavitation bubble can be observed when the concentration is increased owing to an increase in viscosity. In highly viscous solutions, viscous forces acting on the cavitation bubble resist the bubble growth in the medium, suggesting that the decrease in the shock impulse generated from the collapse of the cavitation bubble.

	Concentration [wt%]			
Time [μs]	20	40	60	80
0				
8	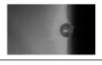			
16	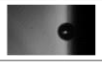			
24	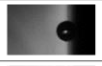			
32				
40				
48	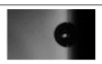			
56			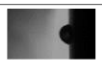	
64				
72	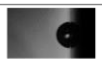		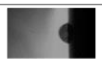	
80				
88			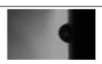	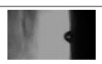
96				
104				
112			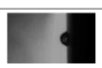	
120	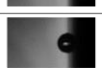	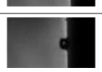	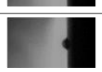	
128	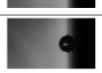	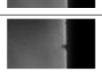	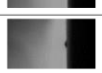	
136	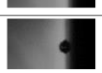	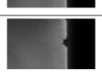		
144		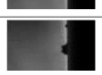		
152	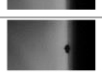	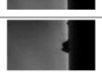	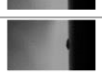	
160	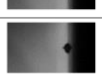	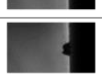		

Figure 4.15 Time evolution of laser-induced cavitation bubble generated on the stainless steel in different concentrations of glycerol solution. The inter-frame duration is 8 μs.

To explore more about the effects of laser intensities on the hardness of the metal, the dynamics of a laser-induced cavitation bubble in 20 wt% concentration of aqueous glycerol solution were examined. The images of cavitation bubbles during their maximum size at different laser intensities were presented in Fig. 4.17 with the diameter measurement. As the laser intensity continues to increase, more plasma is generated on the surface of the

metal, and it absorbs laser energy effectively and expands to form a larger bubble size with more bubble energy.

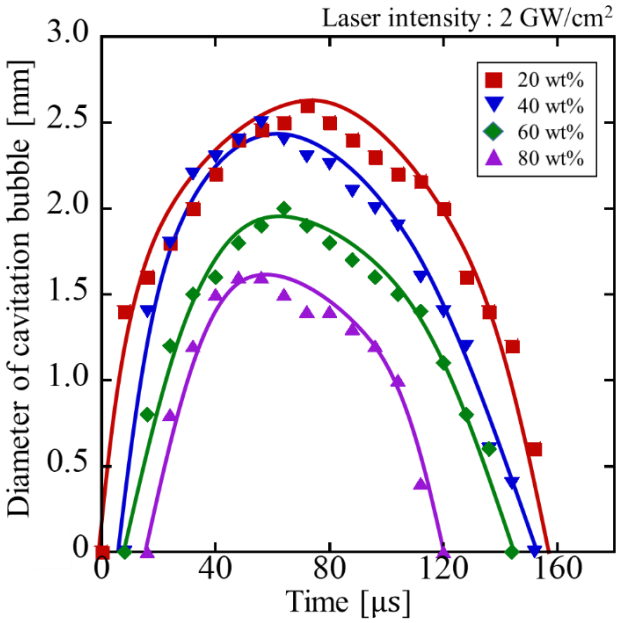

Figure 4.16 Diameter of laser-induced cavitation bubble as a function of time

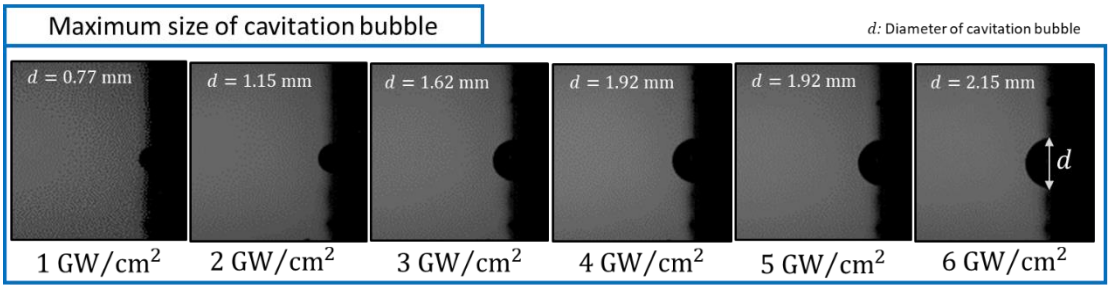

Figure 4.17 Shadowgraph of laser-induced cavitation bubble during maximum size at different laser intensities in 20 wt% concentration of aqueous glycerol solution

4.2.4 Observation of the laser-peened surface

In this section, the discussion point to the observation of the peened surface in 20 and 80 wt% concentrations of aqueous solutions. Laser peening in 20 wt% was found to be effective, meanwhile in 80 wt% laser peening was ineffective. Therefore, both concentrations were selected for comparison. The laser-peened surfaces after laser peening treatment in 20 wt% and 80 wt% were observed through a digital microscope and the images were shown in Fig. 4.18 and 4.19, respectively. The laser peening treatment was carried out at four different coverages: 100, 300, 500, and 900%. The laser intensity was fixed to be 2 W/cm^2.

For 20 wt% concentration, a uniform overlapping dents pattern was obtained at all coverages (see Fig. 4.18). At 100 % of coverage, the dents pattern shows that the laser beam irradiated on the sample successfully. However, in 80 wt% concentration, although the coverage was set to be at 100%, the laser pulse did not reach the sample successfully (see Fig 4.19). This proves that other factors also affect the effectiveness of laser peening treatment at high concentration besides the presence of the small cavitation bubble. This is probably due to non-linear absorption, filamentation, etc. High coverage is necessary to ensure the laser pulse successfully reaches the selected area. Certainly, it will also be necessary to gain a more detailed understanding of the penetration of the laser pulse in glycerol solution.

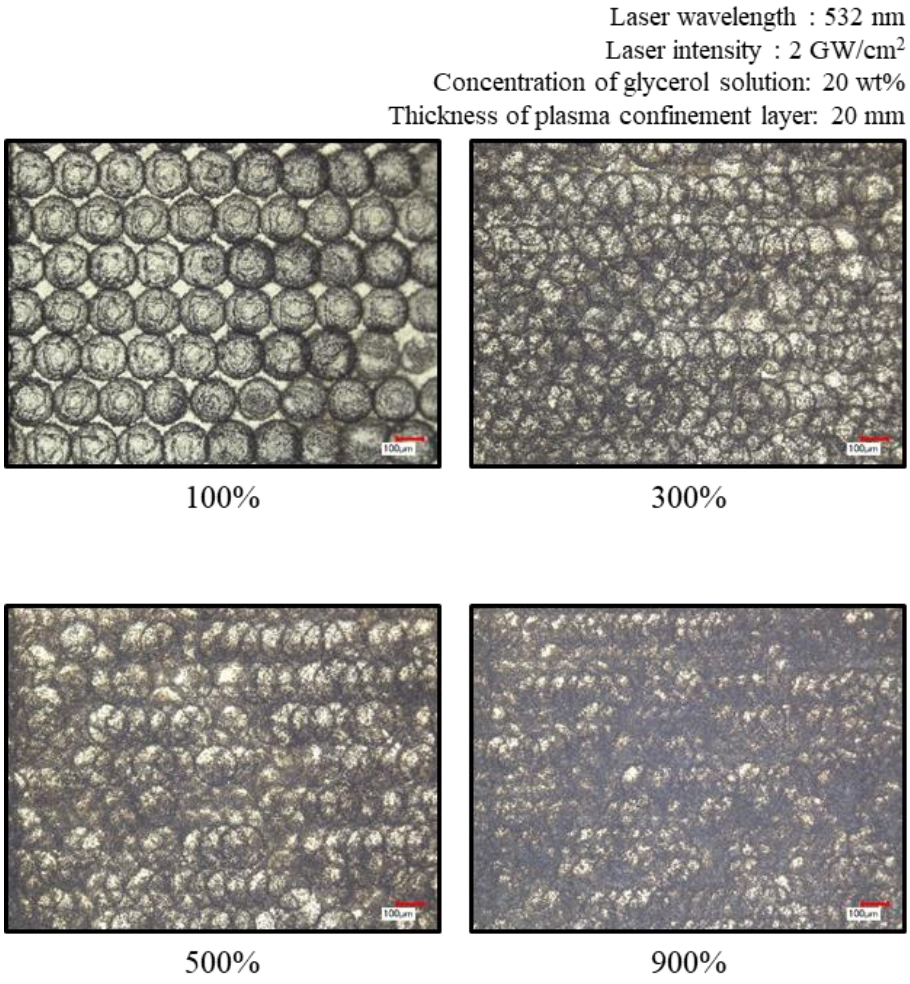

Figure 4.18 Laser-peened surface at different coverages in 20 wt% concentration of aqueous glycerol solution

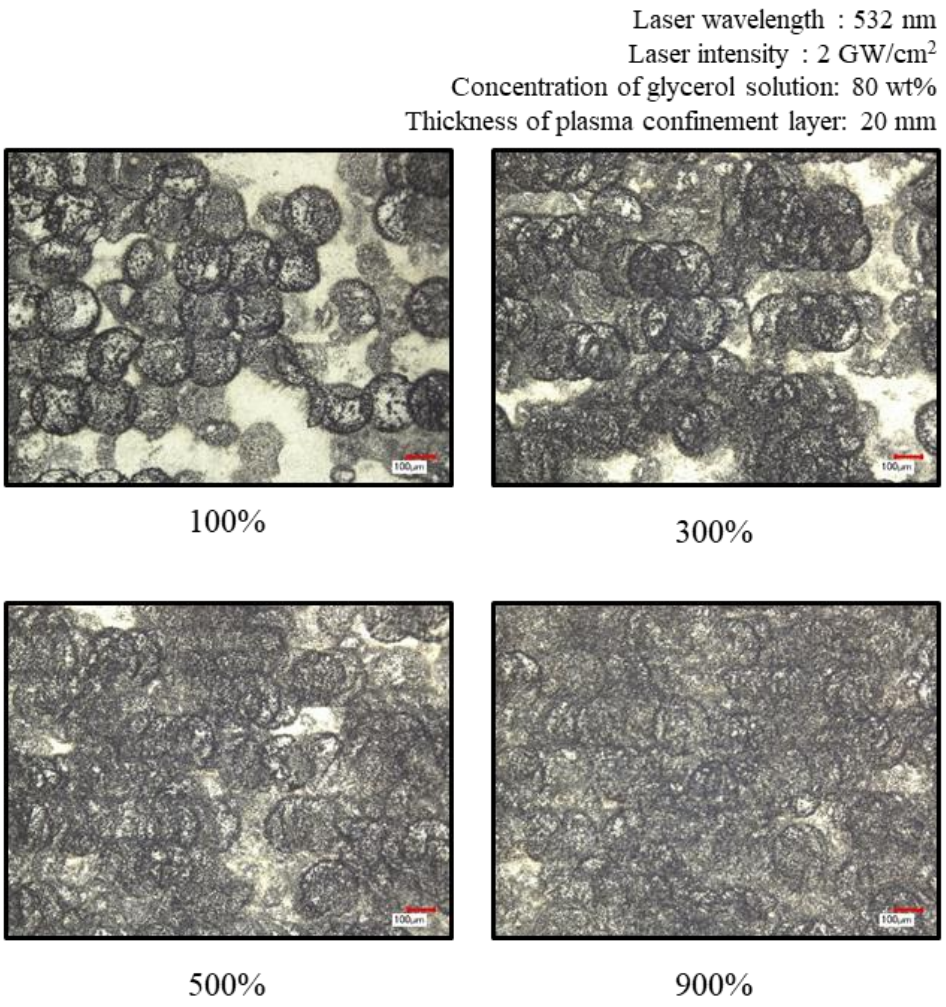

Figure 4.19 Laser-peened surface at different coverages in 80 wt% concentration of aqueous glycerol solution

During the laser peening process at static condition using plasma confinement layer having high concentration, the formation of small bubbles that remains on the optical path of the laser beam must be considered. In the conventional laser peening treatment, the coverage was varied by changing the speed of the x-y stage movement controlled by a computer. This technique was found to be ineffective when employing a plasma confinement layer that has a high concentration. Therefore, a new technique to obtain a uniform overlapping dents pattern has been demonstrated to increase the laser peening performance. In this technique, first, the targeted area of the material's surface was peened by the pulsed laser with a coverage of 100%. Then, the process was repeated on the same targeted area depending on the desired coverage. For instance, to obtain 500% of coverage, laser peening treatment should be performed on the material at 100% of coverage five times. This new technique has been demonstrated on stainless steel. To obtain 100, 300, 500, and 900% of coverages, the sample was peening at 100% of coverage for one time, three times, five times,

and 9 times, respectively. Figure 4.20 shows the images of laser-peened surfaces observed through a digital microscope. Uniform overlapping dents pattern was obtained when the coverage is increased. The effectiveness of laser peening treatment in a high concentration of plasma confinement layer can be increased by using this technique.

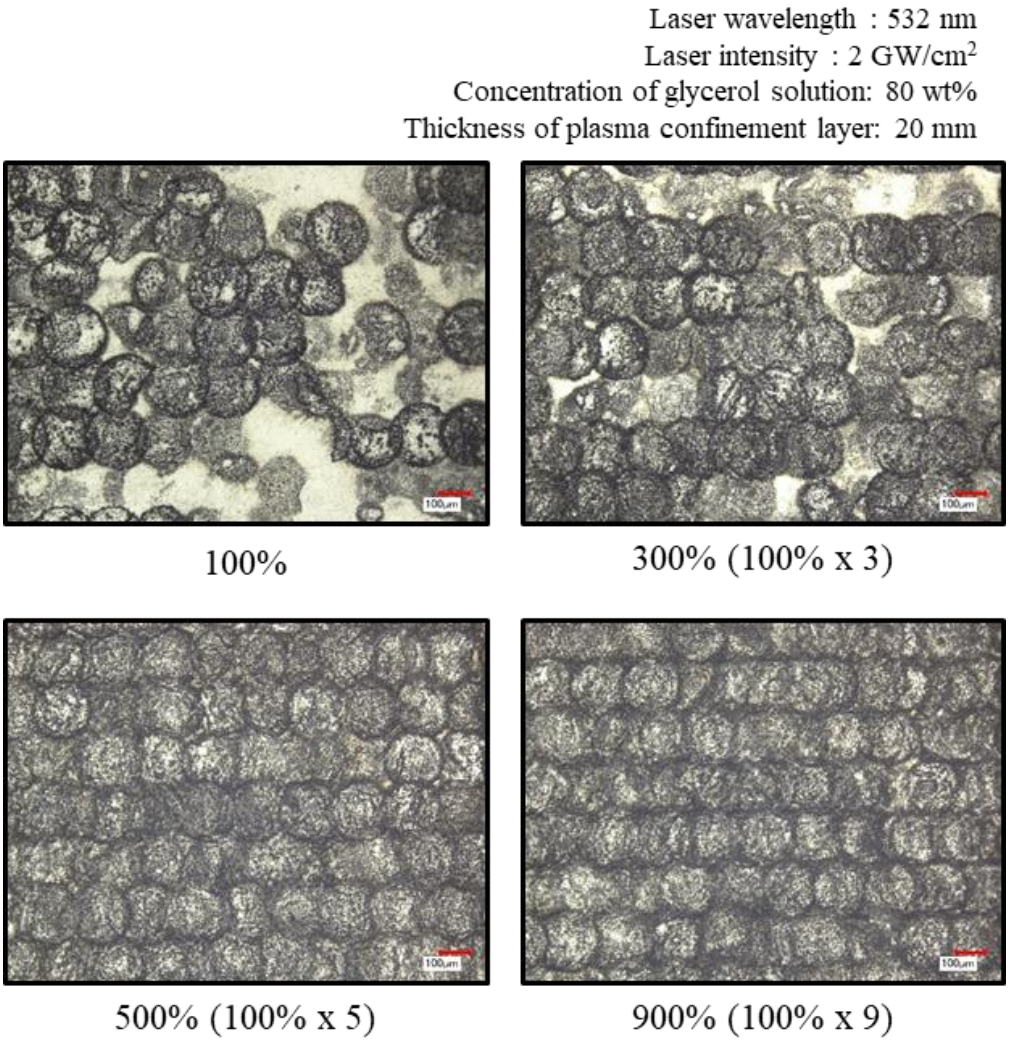

Figure 4.20 Laser-peened surface at different coverages in 80 wt% concentration of aqueous glycerol solution by employing new pattern

4.2.5 Summary

The effectiveness of laser peening treatment is affected by various factors. The highest value of 98 HV was obtained at 900% coverage when the concentration of the aqueous glycerol solution was approximately 20 wt%. In the case of the plasma confinement layer, the acoustic impedance and viscosity of the plasma confinement layer must be balanced to achieve an effective laser peening treatment. Overall, the employment of plasma confinement layer having higher acoustic impedance than water such as glycerol with optimized laser peening parameters can be of great advantage in the field of liquid confining

laser processing. The shock impulse measurement and the observation of the phenomenon that occurred near the metal surface after laser irradiation using high-speed imaging provides a more accurate description of how the viscosity affects the effectiveness of the laser peening process.

Section 4.2 of this dissertation, in part, is a reprint of the material as it appears in "Effects of Laser Peening Parameters on Plastic Deformation in Aqueous Glycerol Solution as Plasma Confinement layer". Journal of Laser Micro/Nanoengineering, 2021, 16:160-165. This work was co-authored by Akihiro Hata, Miho Tsuyama, Manabu Heya, and Hitoshi Nakano. The dissertation author is the first author of this work.

4.3 Effects of laser peening at 1 μm wavelength

The light at 1 μm wavelength is more absorbed than that at 532 nm wavelength in water. However, it still has sufficient interaction with the metal surface and a high dielectric breakdown threshold. Laser peening treatment in the liquid confining medium by using near-infrared wavelength could lead to a generation of strong second shock wave pressure attributed to the collapse of the laser-induced cavitation bubble because of high absorption in liquid. Here, the effects of laser peening at 1 μm wavelength in aqueous glycerol solution have been described in this section.

4.3.1 Overview

By employing an Nd: YAG laser with a pulse width of 5 ns operating at 1064 nm wavelength, the laser peening effects on stainless steel (SUS316L) in glycerol solution as a confining medium is investigated experimentally. The experimental setup including optical arrangement as explained in Section 3.2 was adopted. The concentration of aqueous glycerol solution was varied to control the acoustic impedance of the plasma confinement layer. The degree of plastic deformation on the peened surface was evaluated through the hardness and compressive residual stress to determine the effectiveness of laser peening. In addition, the shock impulse generated due to the confinement of the laser-induced plasma and the collapse of the laser-induced cavitation bubble in various concentrations of glycerol solution was also examined.

4.3.2 Evaluation on plastic deformation after laser peening

The increase in mechanical properties such as hardness and residual stress are desirable in various fields to increase the resistance towards surface-related failure. The influence of the thickness of the plasma confinement layer on the surface hardness of the metal in various concentrations of glycerol solution was investigated. The results obtained were presented in Fig. 4.21. The hardness difference is defined as the increase in the surface hardness at the laser-peened area from its initial hardness. The highest surface hardness of

about 80 HV in 10 wt% concentration of glycerol solution with a thickness of 1 cm was obtained throughout this work. Laser peening treatment was effective when employing a plasma confinement layer with a thickness of 1 cm. It must be noted that the absorption coefficient of water at 1064 nm is higher compared to the 532 nm wavelength. Therefore, it is essential to consider the thickness of the plasma confinement layer when operating at 1064 nm wavelength. In the case, of concentration dependence, the metal hardness increased as the concentration increased from 0 to 10 wt%, and then decreased when the concentration is increased up to 80 wt% for both thicknesses. This shows that laser peening treatment in a lower concentration of glycerol solution (~10 wt%) with a thinner plasma confinement layer was preferable for better laser peening processing.

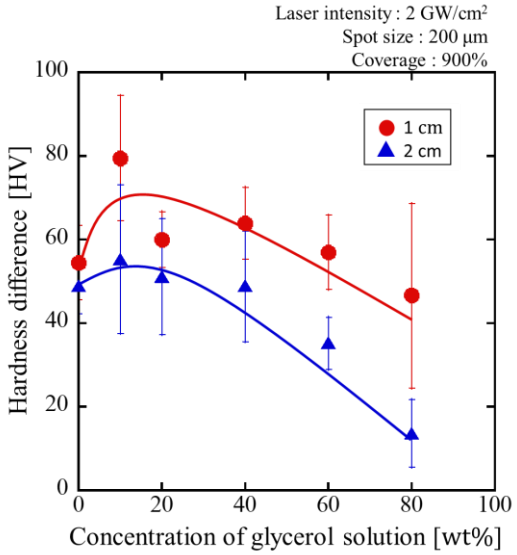

Fig. 4.21 Hardness difference as a function of concentration of glycerol solution at a different thickness of confining medium

The images of laser-peened surfaces after the treatment in various concentrations of aqueous glycerol solution were presented in Fig. 4.22. The coverage and laser intensity were fixed at 900% and 2 GW/cm^2, respectively. Based on the observation on the peened surfaces, it can be assumed that the cause for the hardness reduction at high concentration is due to the presence of a small cavitation bubble as explained in detail in the previous section (see Section 4.2.2).

Figure 4.23 shows the influence of laser intensity on the surface hardness of stainless steel for three different concentrations of glycerol solution (0, 10, and 80 wt%). The laser intensity was adjusted from 0.1 to 4 GW/cm^2. An increase in the laser intensity caused an increase in the surface hardness. This effect corresponds to Eq. (2.2), where the peak pressure of laser-induced plasma in confined mode is proportional to the square root of the laser intensity. Up to 1 GW/cm^2, no remarkable difference in the value of surface hardness

was found for all confining media. However, at $2 - 4\ \mathrm{GW/cm^2}$ of laser intensity, a large difference in hardness value can be seen. The surface hardness is expected to saturate when the laser intensity is more than $4\ \mathrm{GW/cm^2}$. Here, if the laser intensity exceeds the breakdown threshold, the laser light is essentially absorbed within the plasma confinement layer. Based on the result shown in Fig. 4.23, a higher value of surface hardness can be obtained at 10 wt% despite having lower acoustic impedance than 80 wt% concentration of glycerol solution. Therefore, to achieve higher metal hardness, desirable conditions for the plasma confinement layer should be considered.

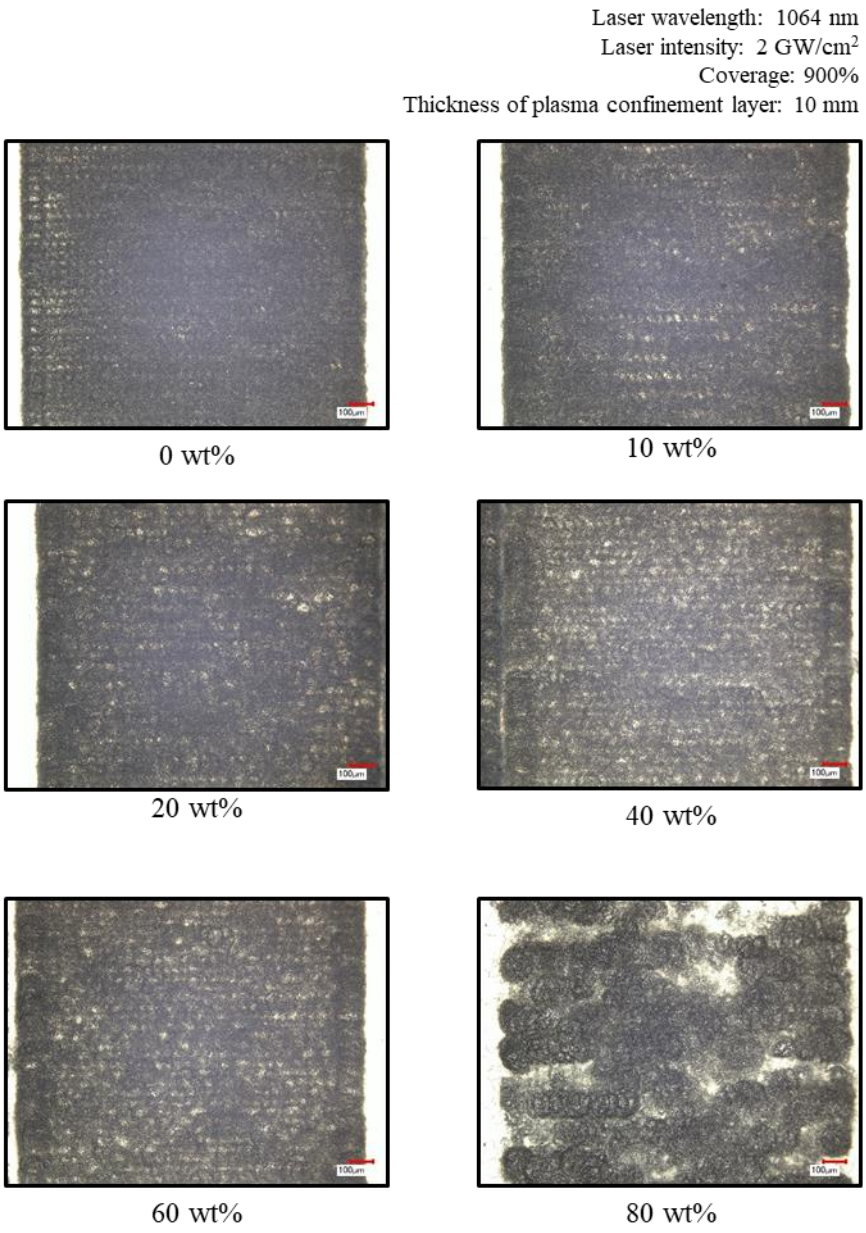

Figure 4.22 Laser-peened surface of stainless steel at various concentrations of glycerol solution

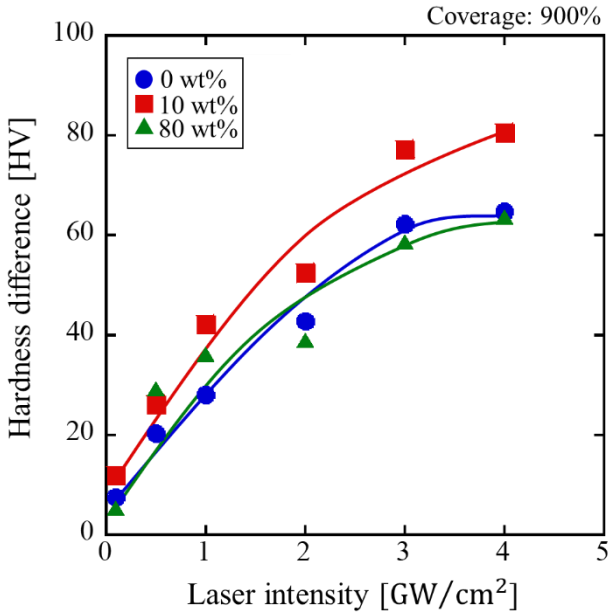

Figure 4.23 Hardness difference as a function of laser intensity

To investigate the effect of concentration on the residual stress induced by laser peening, an X-ray diffraction measurement was performed on the peened surface of the targeted metal. The residual stresses as a function of concentration of glycerol solution at the metal surface (0 μm) and 20 μm in-depth from the metal surface were shown in Fig. 4.24. It must be noted that the compressive residual stresses and tensile residual stress are indicated as negative and positive values, respectively. The highest value of compressive residual stress was found when the concentration is approximately around 10 wt%. Compressive residual stresses were introduced on the metal surface at the concentration of glycerol solution 0 – 60 wt %. However, the compressive residual stress change to tensile stress when the concentration is more than 60 wt%. The properties of the medium seem to be responsible for the tensile residual stress obtained on the surface of the target sample. It is known that the tensile residual stress decreases the fatigue strength and can cause fatigue failure. Concerning the tensile residual stress produced on the metal's surface at 80 wt% of concentration, it is probably due to the low thermal conductivity of confining medium that causes the reduction in heat loss on the plasma and the interface between confining medium and target sample [55]. In this case, when the laser irradiation is stopped, a slow local solidification of melt occurs. This solidification process of melt is slow because of the low thermal conductivity of glycerol solution at high concentration.

Laser peening treatment results in both mechanical and thermal loading of the material. Gill et al. studied the characteristics of surface layers by laser peening and reported that the laser peening without a protective overlay leads to melting and re-solidification on

the surface along with deformation due to the laser shock wave [19]. Installation of protective coating or overlay such as black paint and tape help to protect the surface and avoid the generation of tensile stress on the metal surface. However, it is a time-consuming affair as the coating or overlay causes laser-induced damage during peening and needs to be changed frequently, thus the laser peening process becomes slow and expensive in industrial application.

To evaluate the residual stress at various concentrations beneath the metal surface, 20 μm of the surface layer was removed by electropolishing. Here, compressive residual stresses were obtained at depth of 20 μm regardless of high concentration (80 wt%). At 20 μm in-depth from the metal surface, a peak of compressive residual stress was obtained at a concentration of around 10 wt% due to higher acoustic impedance. The high acoustic impedance of the confining medium contributes to an increase in the intensity of the shock wave pressure that can cause high deformation, thus enhancing the laser peening effect. A confining medium with high acoustic impedance is preferable for obtaining deeper compression. However, when the concentration of glycerol solution is increased, the compressive residual stress decreases, which has almost the same trend as that of hardness (see Fig. 4.21). The reason is probably similar to the effect on hardness, which is influenced by the presence of the small bubble that causes a non-uniform laser peening treatment. This result shows that a low concentration of glycerol solution of around 10 wt% is desirable to obtain high compressive residual stress.

Based on the results shown in Fig. 4.21, aqueous glycerol solution at 10 wt% with a thickness of 1 cm was found to be effective for laser peening processing. Therefore, the residual stress distribution through the depth of the sample that was treated in 10 wt% concentration of glycerol solution was evaluated by measuring the residual stress on the metal after each layer removal through electropolishing. The results obtained were shown in Fig. 4.25. As can be seen, the peak of compressive residual stresses was located at the depth of approximately 20 μm under the metal surface. The compressive residual stress decreases as the depth from the metal surface increases. When depth reaches about 100 μm beneath the surface, the residual stress changes from compressive to tensile.

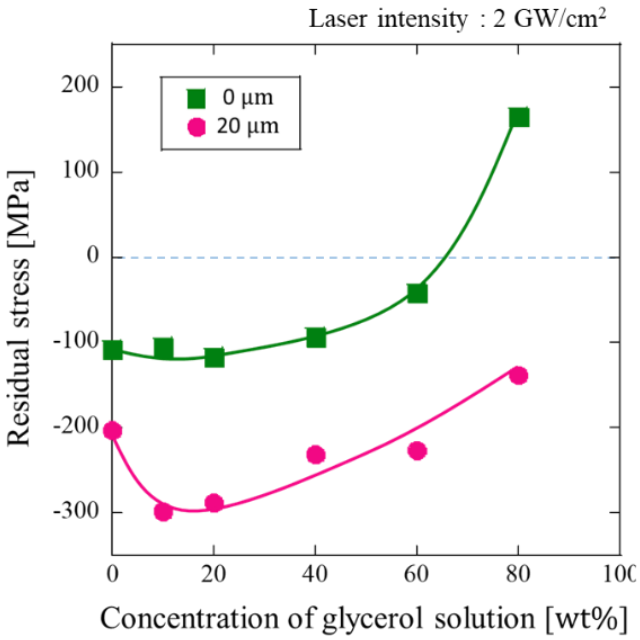

Figure 4.24 Residual stress as a function of concentration of glycerol solution

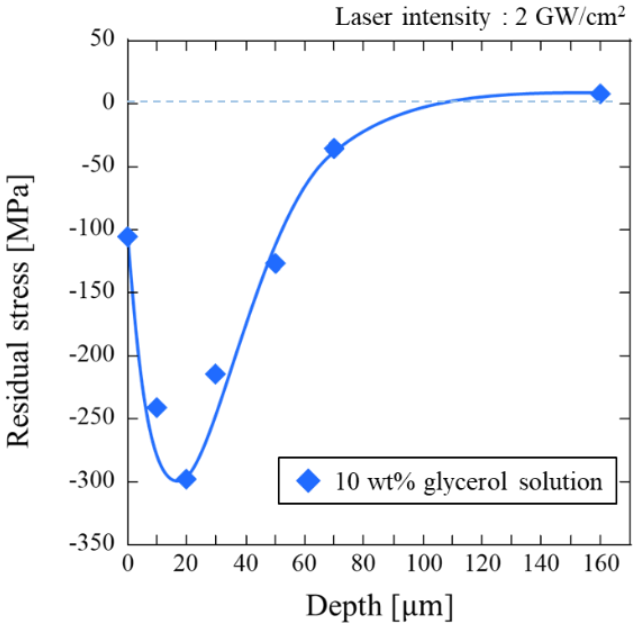

Figure 4.25 Residual stress as a function of depth

4.3.3 Consideration on shock impulse

For a better understanding the influence of liquid properties on the effectiveness on laser peening treatment, the shock impulses generated from the confinement of laser-induced plasma and the collapse of the laser-induced cavitation bubble were measured using a PVDF gauge as described in Section 3.6.2 of Chapter 3. By utilizing Eq. (3.9), the shock impulse can be calculated from the output signal. Figure 4.26 shows the shock impulse generated by

the laser-induced plasma and the laser-induced cavitation bubble as a function of concentration of glycerol solution. The laser intensity and spot size were fixed at 2 GW/cm^2 and 200 μm, respectively. In water as the plasma confinement layer, the shock impulse obtained was plotted at a concentration of 0 wt%. The shock impulses generated from the collapse of laser-induced cavitation bubble P_C were relatively stronger than that from the laser-induced plasma P_L. This indicates that the laser-induced cavitation bubble plays a dominant role in the laser peening treatment in the liquid confining medium at near-infrared wavelength. In the case of laser-induced plasma, the shock impulse increases when the concentration is increased to 10 wt%. As the concentration continues to increase, the shock impulse generated from the confinement of the laser-induced plasma remains almost unchanged. In the case of shock impulse generated from the collapse of a laser-induced cavitation bubble, a higher shock impulse can be obtained compared to water (0 wt%). As in the case of the laser-induced cavitation bubble, the highest magnitude of P_C was obtained at a concentration of around 60 wt%. The influence of the glycerol concentration on the shock impulse generated from the cavitation bubble collapse is explained in detail based on the shock profile.

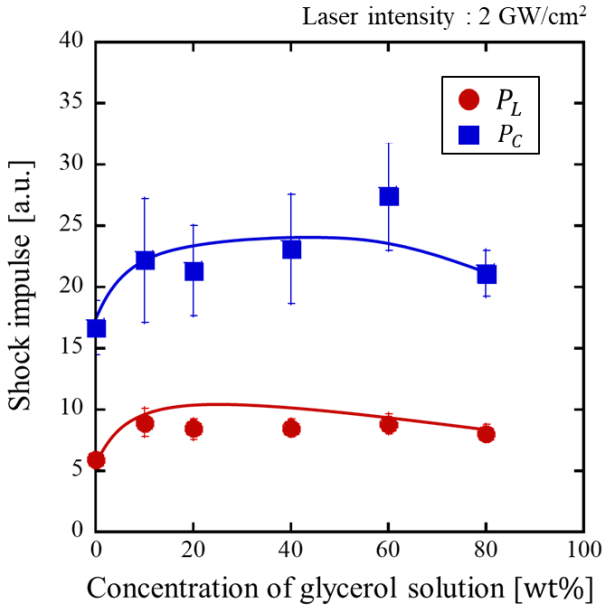

Figure 4.26 Shock impulse of laser-induced plasma and cavitation bubble as a function of concentration of glycerol solution

Figure 4.27 shows the profile of shock impulse generated from the confinement of laser-induced plasma and the collapse of laser-induced cavitation bubble detected by PVDF gauge in aqueous glycerol solution having concentrations of 0, 10, 20, 40, 60, and 80 wt%. The duration of force generated from the laser-induced plasma in several microseconds order.

Therefore, another figure that shows only the shock profile of laser-induced cavitation bubble with a smaller time scale was made (see Fig. 4.28). In the case of shock profiles obtained from the collapse of the laser-induced cavitation bubble, the duration of the force acting on the target is longer which is in the order of several tenths of microseconds. One possible explanation is the high absorptivity in liquid at 1064 nm wavelength. With the aid of the high temperature from the laser-induced plasma, a thin layer of vapor is formed, thus inducing the formation of a large hemispherical cavitation bubble on the surface of the target material. The collapse of the large cavitation bubble leads to the generation of strong shock impulse. As a result, a higher shock impulse produced by the collapse of the laser-induced cavitation bubble compared to the laser-induced plasma is obtained as can be seen in Fig. 4.26. This indicates that the laser-induced cavitation bubble plays a dominant role in the laser peening treatment in the liquid confining medium at about 1 μm wavelength.

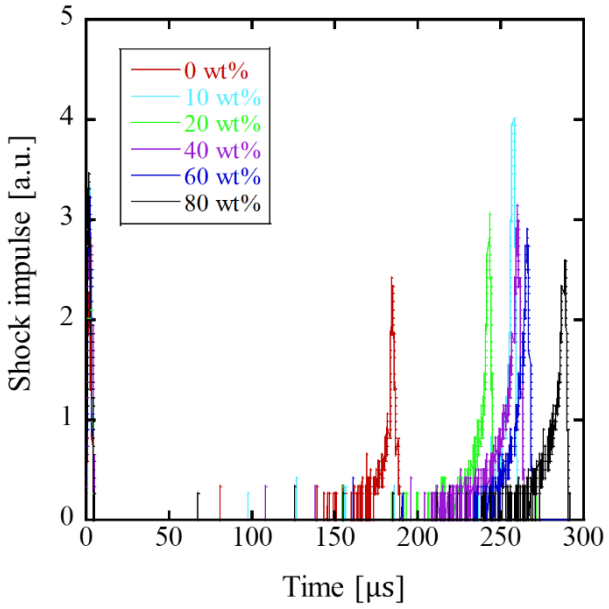

Figure 4.27 The profile of shock impulses generated from both laser-induced plasma and the laser-induced cavitation bubble detected by PVDF gauge in various concentrations of aqueous glycerol solution

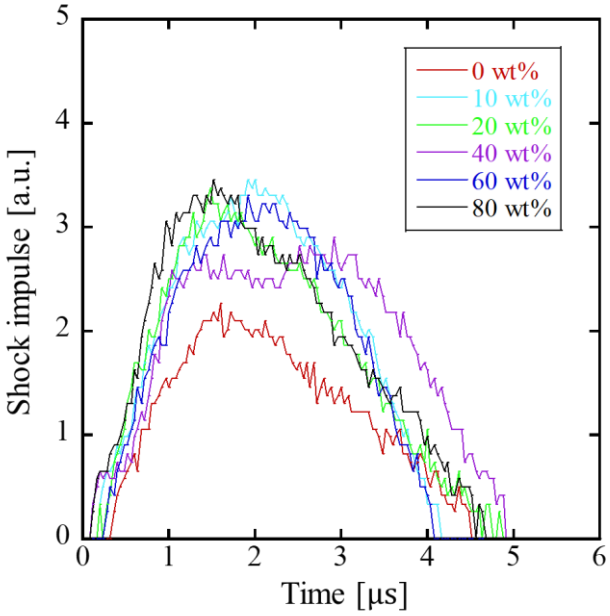

Figure 4.28 Signal of shock impulse generated from laser-induced plasma detected by PVDF gauge in various concentrations of aqueous glycerol solution

It is thought that the results on the shock impulses should correspond to the results on metal hardness. However, the results obtained were different at a high concentration of glycerol solution. This is probably influenced by the number of laser pulses irradiated on the metal surface (i.e., coverage). The pressure measurement was done by evaluating the shock impulse generated from a single laser pulse, whereas the laser peening treatment was done at 900% of coverage. Therefore, the hardness obtained from a single shot laser pulse on the target sample has been investigated to consider the influence of the number of laser shots. Figure 4.27 shows the hardness of the metal's surface from a single shot laser pulse at 2 GW/cm^2 of laser intensity. There is a good correlation between the results of shock impulse measurement and the hardness of the metal's surface from a single shot shown in Figs. 4.26 and 4.29, respectively. This shows that other laser peening parameter such as coverage affects the outcome of the laser peening process depending on the properties of the liquid.

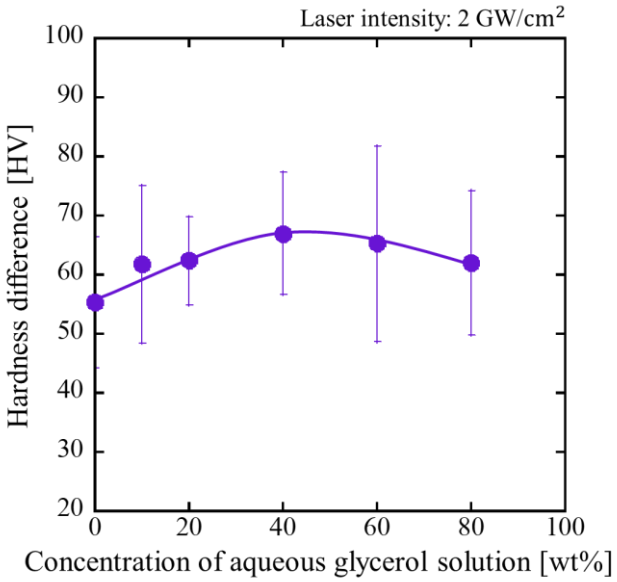

Figure 4.29 Hardness difference as a function of concentration of glycerol solution (One-shot)

Throughout this investigation, it has been found that the laser peening process at 1 μm wavelength is possible with appropriate laser peening parameter when employing plasma confinement layer having higher acoustic impedance than water such as glycerol solution. In addition, high amplitude of the shock impact produced by the confinement of the laser-induced plasma and the collapse of the laser-induced cavitation bubble are obtained at 10 wt% concentration of aqueous glycerol solution with a coverage of 900%.

4.3.4 Summary

The effects of the laser peening treatment at 1064 nm wavelength in an aqueous glycerol solution were investigated. The results of this work demonstrate a high potential of glycerol solution at a concentration of around 10 wt% being applied as a confining medium. Our results on shock impulse measurement by using a PVDF gauge sensor implicates that glycerol solution is an effective confining medium due to the high amplitude of the shock impulse generated by the laser-induced plasma and the collapse of the laser-induced cavitation bubble. A high magnitude of the shock impulse from the collapse of the laser-induced cavitation bubble is beneficial to induce strong compressive residual stress in the treated material. However, through the evaluation of the surface hardness and residual stresses of the peened surface, it was found that the effectiveness of laser peening treatment significantly depends on the laser peening parameter. Therefore, this investigation shows that the effectiveness of laser peening treatment in glycerol solution using 1064 nm wavelength can be obtained with the employment of desirable laser peening conditions.

4.4 Effects of adjusting the viscosity of glycerol solution on laser peening

A plasma confinement layer having high acoustic impedance is desirable to enhance the laser peening effect. However, in Section 4.1, it has been described that employing a high concentration of glycerol solution as a plasma confinement layer results in a decrease of laser peening effect due to high viscosity. When a plasma confinement layer in a highly viscous state is used, the cavitation bubble in a steady-state rises slowly toward the water surface and stays on the optical path of the laser, causing scattering of the laser light. Although glycerol solution is a highly viscous solution, its viscosity decreases as the temperature of the aqueous solution is raised. Therefore, in this study, an approach to increase the effectiveness of laser peening treatment by controlling the temperature of the plasma confinement layer was conducted. The effects of adjusting the viscosity of the plasma confinement layer by controlling its temperature on laser peening were evaluated and described.

4.4.1 Overview

Since the viscosity of the aqueous glycerol solution at a high concentration affects the efficiency of the laser peening process, the temperature of the solution was increased to decrease its viscosity. Figure 4.30 shows the relationship between the concentration and viscosity of the glycerol aqueous solution at each temperature ranging from 30 to 80 °C which were measured by using an Ostwald's viscometer. A bigger difference in viscosity can be seen when the temperature of the aqueous glycerol solution is at 80 wt% is increased from 30 to 80 °C compared to lower concentrations. The decrease in viscosity is desirable to enhance the laser peening process in the liquid confining medium.

To investigate the effects of adjusting the viscosity of glycerol solution on the laser peening process, the laser peening condition is explained as follows. Nd: YAG laser with wavelength 532 nm and 4 ns pulse width was used and the experimental setup including optical arrangement as explained in Section 3.2 was adopted. The laser intensity, coverage, and thickness of the plasma confinement layer were fixed to be 2 GW/cm^2, 500%, and 20 mm, respectively. The contents of this section are described as follows. Laser peening treatment was performed on stainless steel by changing the concentration and temperature of the plasma confinement layer, then the plastic deformation that occurred on the surface of the metal is evaluated through Vickers hardness and residual stress measurement.

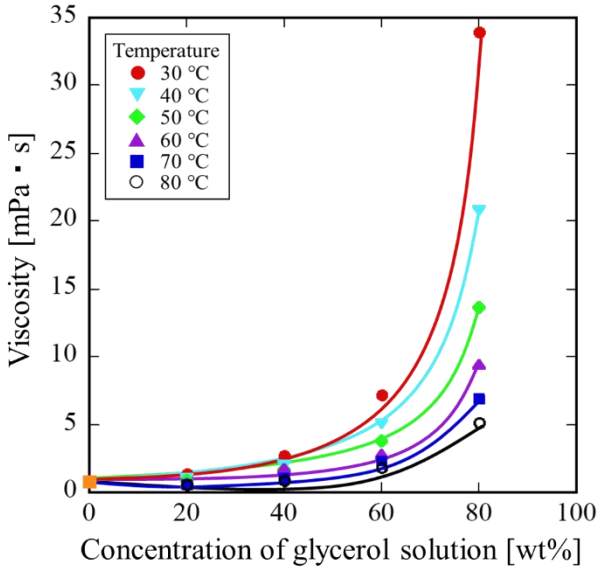

Figure 4.30 Viscosity of glycerol solution as a function of concentration at various temperature

4.4.2 Evaluation on plastic deformation of laser peening

The effects of controlling the temperature of aqueous glycerol solution to adjust the viscosity on the effectiveness of the laser peening process were evaluated by measuring the surface hardness of the target sample. Figure 4.31 shows the hardness difference as a function of glycerol solution at different temperatures. Hardness difference is defined as the difference between the hardness on the peened surface and the initial hardness. The data plotted at 0 wt% concentration is the result of the hardness of the metal surface after laser peening treatment in water at 30 °C. In order to control the viscosity of the aqueous glycerol solution, the temperature was changed from 30 to 80 °C for all concentrations (20, 40, 60, and 80 wt%). As a result, the surface hardness of the metal at all concentrations increases as the temperature rises. The results obtained and described in the previous section 4.2 (see Fig. 4.7) are inconsistent with the data shown in Fig. 4.31 at a low temperature of about 30 °C. The slight difference in the materials condition of the target sample or the properties of the plasma confinement layer probably influences the effects of laser peening. However, when the temperature of the aqueous solution is at 80 °C, the results show the same trend which has the highest value of surface hardness at the concentration of about 20 wt%. Laser peening treatment is most effective when the concentration is about 20 wt%.

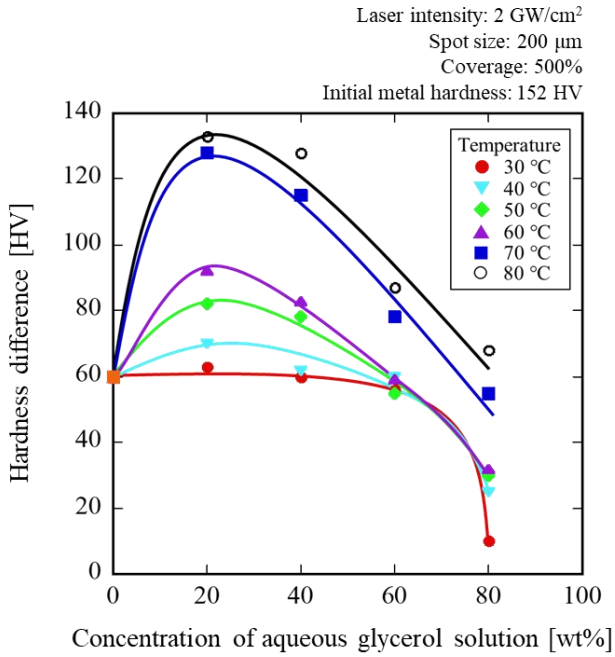

Figure 4.31 Hardness difference as a function of glycerol solution at different temperatures

The X-ray diffraction method was used for residual stress measurement. About 20 μm of the surface layer was removed by electropolishing. The residual stress generated at about 20 μm in-depth near the surface region of the sample subjected to the laser peening treatment was measured when the temperature of the glycerol aqueous solution was adjusted from 30 to 80 °C at various concentrations. The results obtained are shown in Fig. 4.32. The negative value of residual stress in Fig. 4.33 denotes compressive residual stress induced by the laser peening treatment. When the residual stress value is negative, the residual stress in the compression direction becomes the residual stress. The residual stress value in the compression direction increases as the temperature rises, as shown in Fig. 4.32.

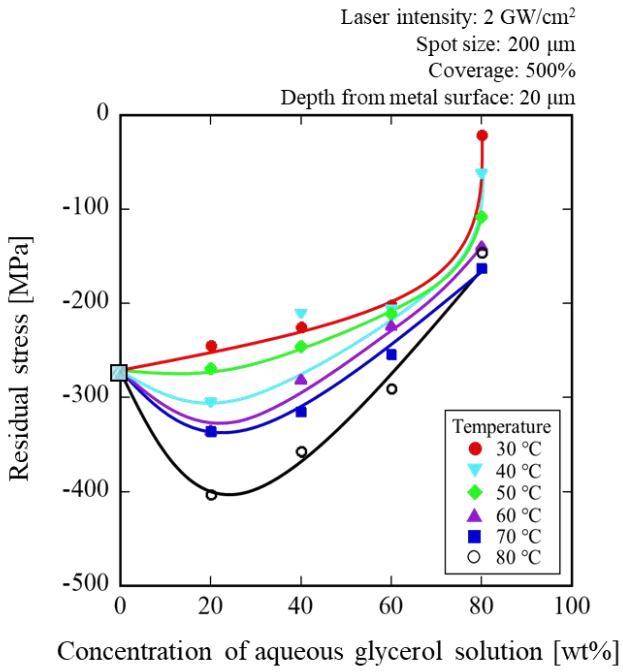

Figure 4.32 Residual stress as a function of concentration of glycerol solution at different temperature

4.4.3 Consideration on shock impulse

The shock impulse generated from both the laser-induced plasma and the collapse of the laser-induced cavitation bubble were measured by using a PVDF gauge sensor as described in Section 3.6.2 of Chapter 3 to examine the reasons for the highest surface hardness obtained at about 20 wt% concentration of glycerol solution.

Figures 4.33 and 4.34 show the shock impulse of laser-induced plasma and the collapse of the laser-induced cavitation bubble at different concentrations and temperatures, respectively. From Fig. 4.33, it was found that the maximum value of shock impulse generated from the laser-induced plasma is obtained at 20 wt% concentration of aqueous glycerol solution. In addition, the characteristics of the shock impulse have almost the same trend as that of hardness. The magnitude of the ablation pressure peaked at 20 wt%, indicating that it is necessary to consider not only the acoustic impedance dependence but also the viscosity. However, in the case of shock impulse from the cavitation bubble shown in Fig. 4.34, there is no strong dependence on the concentration of the solution and temperature.

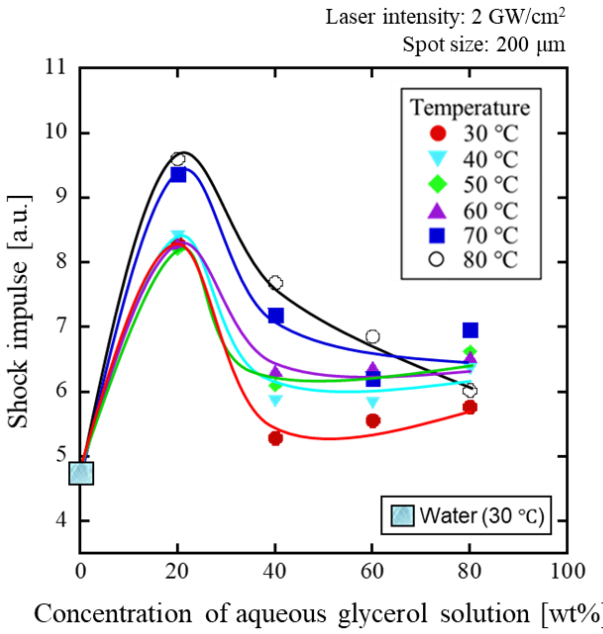

Figure 4.33 Shock impulse of laser-induced plasma as a function of glycerol solution at different temperature

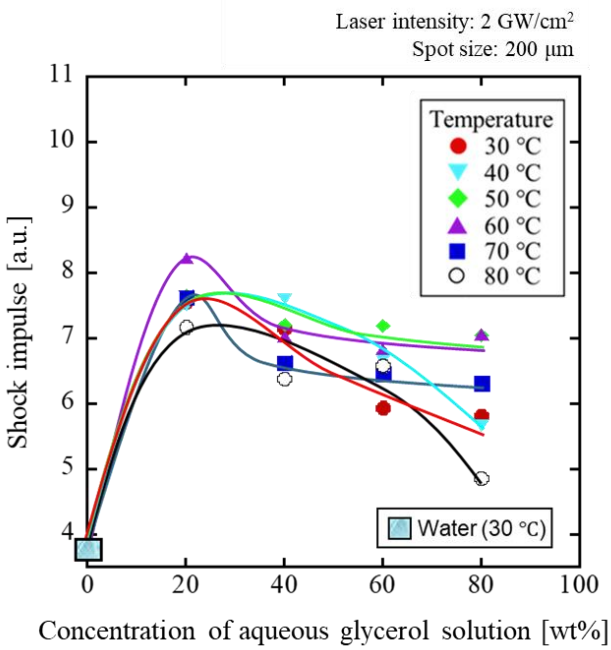

Figure 4.34 Shock impulse of laser-induced cavitation bubble as a function of glycerol solution at different temperature

4.4.4 Summary

In this study, an aqueous solution of glycerin was used for the plasma confinement layer, and the hardness and residual stress of the sample were evaluated when the temperature was changed to 30 to 80 °C. Based on the evaluation of the surface hardness

and compressive residual stress of the target sample, laser peening treatment at concentration and temperature of 20 wt% and 80 °C, respectively were found to be effective. The study in this part shows that by controlling the temperature of the aqueous glycerol solution, the viscosity of the plasma confinement layer can be adjusted to increase the efficiency of laser peening processing.

Chapter 5: Conclusions

5.1 Summary of the results

The effects of controlling the plasma confinement layer and laser peening parameters on the plastic deformation of stainless steel were investigated systematically. The plastic deformation was evaluated through hardness and residual stress. Throughout this study, it has been found that by controlling the temperature, liquid properties, and thickness of the plasma confinement layer, an efficient laser peening process can be achieved. In the case of temperature control, instead of replacing water with other solutions having higher acoustic impedance, the acoustic impedance of water can be varied by adjusting its temperature. On the other hand, a transparent confining medium such as glycerol is effective as an alternative for substituting water as a plasma confinement layer because it can enhance the shock wave pressure in laser-induced shock processing due to higher acoustic impedance. However, the acoustic impedance and viscosity of the plasma confinement layer must be balanced to achieve an effective laser peening treatment.

In addition, the effects of laser peening parameters such as laser intensity, coverage, and laser wavelength on the plastic deformation of stainless steel in the liquid confining medium were studied systematically. Suitable parameters have been found under the control of the plasma confinement layer.

Dual shock impact can be obtained from the confinement of laser-induced plasma and the collapse of laser-induced cavitation bubble when employing a liquid confining medium. The laser peening effect can be estimated by measuring the shock impulse generated from the confinement of laser-induced plasma and the collapse of the laser-induced cavitation bubble by using a PVDF gauge. High shock impulses generated from the laser-induced plasma and the collapse of the cavitation bubble are attributed to the optimum condition of the plasma confinement layer.

This research enhances the understanding of the mechanisms of the laser peening process, particularly in the liquid confining medium. In addition, the application of the proposed technique in this study that considers properly the amplitude of the shock wave pressure, and the shock loading time of laser-induced plasma and laser-induced cavitation bubble will result in high-efficiency laser peening treatment and provide maximum benefits in various applications.

5.2 Future works

The plasma confinement layer helps to improve the mechanical properties of engineering surfaces that are employed in a variety of fields. Nowadays, understanding the mechanism of laser peening in a liquid confining medium is a challenging task. For that reason, further work involving simulations to investigate the mechanisms of laser-induced

plasma and laser-induced cavitation bubbles in a liquid confining medium should be planned soon. For an accurate estimation, it is desirable to have prior knowledge of the expected state of plasma caused by laser-induced plasma and laser-induced cavitation bubbles while constructing the database. With a combination of experimental observations, numerical simulations, and theoretical knowledge, the selection of the most effective processing parameters becomes much easier. As a result, an effective laser peening process can be achieved.

References

[1] M. Kahlin, H. Ansell, D. Basu, A. Kerwin, L. Newton, B. Smith, J.J. Moverare, Int. J. Fatigue 134 (2020) 105497.

[2] M. John, P.R. Kalvala, M. Misra, P.L. Menezes, Materials (Basel). 14 (2021) 1–30.

[3] L. Hackel, J.R. Rankin, A. Rubenchik, W.E. King, M. Matthews, Addit. Manuf. 24 (2018) 67–75.

[4] C.F. Yao, X.T. Dou, D. Wu, Z. Zhou, J. Zhang, Adv. Mech. Eng. 8 (2016) 1–10.

[5] R. Fabbro, J. Fournier, P. Ballard, D. Devaux, J. Virmont, J. Appl. Phys. 68 (1990) 775–784.

[6] R. Fabbro, P. Peyre, L. Berthe, X. Scherpereel, J. Laser Appl. 10 (1998) 265–279.

[7] P. Peyre, L. Berthe, X. Scherpereel, R. Fabbro, E. Bartnicki, J. Appl. Phys. 84 (1998) 5985–5992.

[8] L. Berthe, R. Fabbro, P. Peyre, L. Tollier, E. Bartnicki, J. Appl. Phys. 82 (1997) 2826–2832.

[9] H. Nakano, M. Tsuyama, S. Miyauti, T. Shibayanagi, M. Tsukamoto, N. Abe, J. Laser Micro Nanoeng. 5 (2010) 175–178.

[10] H. Soyama, Metals (Basel). 11 (2021).

[11] S. Prabhakaran, S. Kalainathan, Mater. Des. 107 (2016) 98–107.

[12] H. Zhang, X. Ren, Y. Tong, E. Asuako Larson, S. Adu-Gyamfi, J. Wang, X. Li, Results Phys. 12 (2019) 1204–1211.

[13] D. Liu, Y. Shi, J. Liu, L. Wen, Surf. Coatings Technol. 378 (2019) 124824.

[14] J. Zhu, X. Jiao, C. Zhou, H. Gao, Energy Procedia 16 (2012) 153–158.

[15] A. Salimianrizi, E. Foroozmehr, M. Badrossamay, H. Farrokhpour, Opt. Lasers Eng. 77 (2016) 112–117.

[16] C.J. Yocom, X. Zhang, Y. Liao, Opt. Laser Technol. 108 (2018) 32–45.

[17] B.P. Fairand, A.H. Clauer, R.G. Jung, B.A. Wilcox, Appl. Phys. Lett. 25 (1974) 431–433.

[18] P. Ballard, J. Fournier, R. Fabbro, J. Frelat, P. Ballard, J. Fournier, R. Fabbro, J.F. Residual, S. Induced, (1991).

[19] A.S. Gill, A. Telang, V.K. Vasudevan, J. Mater. Process. Technol. 225 (2015) 463–472.

[20] X. Hong, S. Wang, D. Guo, H. Wu, J. Wang, Y. Dai, X. Xia, Y. Xie, Opt. Lasers Eng. 29 (1998) 447–455.

[21] Q. lin Xiong, T. Shimada, T. Kitamura, Z. Li, Opt. Laser Technol. 131 (2020).

[22] K. Elango, J.S. Hoppius, L.M. Kukreja, A. Ostendorf, E.L. Gurevich, Surf. Coatings Technol. 397 (2020) 125988.

[23] J. Radziejewska, M. Strzelec, R. Ostrowski, A. Sarzyński, Opt. Lasers Eng. 126

(2020).

[24] C. Le Bras, A. Rondepierre, R. Seddik, M. Scius-Bertrand, Y. Rouchausse, L. Videau, B. Fayolle, M. Gervais, L. Morin, S. Valadon, R. Ecault, D. Furfari, L. Berthe, Metals (Basel). 9 (2019) 1–13.

[25] Y. Sano, K. Akita, K. Masaki, Y. Ochi, I. Altenberger, B. Scholtes, J. Laser Micro Nanoeng. 1 (2006) 161–166.

[26] Y. Sano, N. Mukai, M. Obata, 3rd Conf. Shot Peen. Osaka (2008).

[27] Y. Sano, K. Akita, T. Sano, Metals (Basel). 10 (2020) 1–12.

[28] Y. Sano, Metals (Basel). 10 (2020).

[29] D. Glaser, C. Polese, Appl. Phys. A Mater. Sci. Process. 123 (2017) 1–10.

[30] M. Senegačnik, K. Kunimoto, S. Yamaguchi, K. Kimura, T. Sakka, P. Gregorčič, Ultrason. Sonochem. 73 (2021).

[31] J. Gu, C. Luo, P. Ma, X. Xu, Y. Wu, X. Ren, Appl. Surf. Sci. 562 (2021) 150242.

[32] H. Soyama, J. Mater. Process. Technol. 269 (2019) 65–78.

[33] I. Akhatov, O. Lindau, A. Topolnikov, R. Mettin, N. Vakhitova, W. Lauterborn, Phys. Fluids 13 (2001) 2805–2819.

[34] L. Martí-López, R. Ocaña, E. Piñeiro, A. Asensio, Phys. Procedia 12 (2011) 442–451.

[35] J. Long, M.H. Eliceiri, L. Wang, Z. Vangelatos, Y. Ouyang, X. Xie, Y. Zhang, C.P. Grigoropoulos, Opt. Laser Technol. 134 (2021) 106647.

[36] J. Gu, C. Luo, Z. Lu, P. Ma, X. Xu, X. Ren, Ultrason. Sonochem. 72 (2021) 105441.

[37] W. Garen, F. Hegedűs, Y. Kai, S. Koch, B. Meyerer, W. Neu, U. Teubner, Shock Waves 26 (2016) 385–394.

[38] N. Dabir-Moghaddam, Z. Liu, B. Wu, J. Appl. Phys. 121 (2017) 1–11.

[39] J. Long, M. Eliceiri, Z. Vangelatos, Y. Rho, L. Wang, Z. Su, X. Xie, Y. Zhang, C.P. Grigoropoulos, Opt. Express 28 (2020) 14300.

[40] E.V.S. Michael Bass, Casimer DeCusatis, Jay Enoch, Vasudevan Lakshminarayanan, Guifang Li, Carolyn MacDonald, Virendra Mahajan, Handbook of Optics, McGraw-Hill Education, 2009.

[41] N.S. Masroon, A. Hata, M. Tsuyama, M. Heya, H. Nakano, Optik (Stuttg). 242 (2021) 167097.

[42] N.S. Masroon, H. Hirata, M. Tsuyama, M. Heya, H. Nakano, J. Laser Micro Nanoeng. 16 (2021) 160–165.

[43] T.T.P. Nguyen, R. Tanabe, Y. Ito, Opt. Laser Technol. 100 (2018) 21–26.

[44] M. Tsuyama, N. Ehara, K. Yamashita, M. Heya, H. Nakano, Appl. Phys. A Mater. Sci. Process. 124 (2018) 1–6.

[45] F. Bauer, (2004) 1121–1124.

[46] P. Peyre, L. Berthe, R. Fabbro, A. Sollier, J. Phys. D. Appl. Phys. 33 (2000) 498–503.

[47] H. Kawai, Jpn. J. Appl. Phys. 8 (1969) 975–976.

[48] A. V. Shirinov, W.K. Schomburg, Sensors Actuators, A Phys. 142 (2008) 48–55.

[49] Ian P.Jones, Material Science for Electrical and Electronic Engineers, Oxford University Press, 2001.

[50] M. Tsuyama, Y. Kodama, Y. Miyamoto, I. Kitawaki, M. Tsukamoto, H. Nakano, J. Laser Micro Nanoeng. 11 (2016) 227–231.

[51] X. mei Liu, Z. Long, J. He, B. Bei Li, X. hua Liu, J. yun Zhao, J. Lu, X. wu Ni, Optoelectron. Lett. 9 (2013) 317–320.

[52] K. Peng, F.G.F. Qin, R. Jiang, S. Kang, Ultrason. Sonochem. 69 (2020) 105253.

[53] T. Takata, M. Enoki, P. Chivavibul, A. Matsui, Y. Kobayashi, Mater. Trans. 57 (2016) 1776–1783.

[54] X.M. Liu, J. He, J. Lu, X.W. Ni, Jpn. J. Appl. Phys. 48 (2009).

[55] P. Ouyang, P. Li, E.G. Leksina, S. V. Michurin, L. He, Appl. Surf. Sci. 360 (2016) 880–888.

[56] M. Ivanenko, M. Werner, S. Afilal, M. Klasing, P. Hering, Med. Laser Appl. 20 (2005) 13–23.

[57] L. Ke, H. Zhu, W. Lei, Z. Cheng, Photonics Optoelectron. Meet. 2009 Ind. Lasers Appl. 7515 (2009) 75150G.

[58] A. Salama, L. Li, P. Mativenga, D. Whitehead, Appl. Phys. A Mater. Sci. Process. 122 (2016).

[59] K. Uno, H. Hayashi, T. Akitsu, T. Jitsuno, J. Infrared, Millimeter, Terahertz Waves 34 (2013) 217–224.

[60] K. Uno, K. Nakamura, T. Goto, T. Jitsuno, J. Infrared, Millimeter, Terahertz Waves 30 (2009) 1123–1130.

[61] K. Uno, T. Jitsuno, Opt. Laser Technol. 101 (2018) 195–201.

[62] K. Uno, S. Watarai, Y. Kodama, K. Yoneya, T. Jitsuno, Opt. Laser Technol. 148 (2022) 107745.

[63] A. Kluge, H. Gueldner, T. Trompa, D. Mory, IEEE Trans. Dielectr. Electr. Insul. 22 (2015) 1954–1962.

Appendix

Introduction

A CO_2 laser is a gas laser that produces a strong infrared light at a wavelength ranging from 9.4 μm to 11.6 μm. The excitation schemes used for a CO_2 laser are classified into longitudinal and transverse excitation schemes according to the structure of the discharge tube. Pulsed, DC, or RF discharge is used for the pumping of CO_2 laser. Pulsed lasers, of course, can deliver much higher values of power density in a short pulse. In this regard, our research will be focused on the pulsed CO_2 laser.

Pulsed CO_2 laser such as transversely excited atmospheric (TEA) CO_2 laser has received attention because of their successful applications. In general, TEA CO_2 laser emits pulses with high output energy and short pulse width (typically a spike pulse with a pulse width of about 100 ns and a pulse tail of several microseconds). It is used in various applications including laser ablation in material processing, medical surgery, light detection and ranging (LIDAR), surface cleaning, and many more [56–58].

However, due to the complexity, high cost, and ongoing maintenance requirements, TEA CO_2 laser has presented significant challenges for many users and its applications are limited for huge companies or businesses because of the high investment needed. Therefore, there is a high demand for simple, compact, and affordable pulsed CO_2 lasers.

Recently, Uno et al. has reported that a longitudinally excited CO_2 laser using a capacitor transfer circuit, produced the output energy of 50 mJ with a pulse width of about 100 ns and a pulse tail length of 60 μs. Laser pulses produced by the longitudinally excited CO_2 laser were irradiated onto a human tooth and a glass plate. The results show that the human tooth without carbonization and glass marking without cracks can be realized [59]. In the longitudinal excitation scheme, the discharge is produced along the direction of the laser axis, and the electrodes are well separated, thus giving a small discharge cross-section. The long discharge length provides a high breakdown voltage at a low gas pressure. Laser oscillation at low gas pressure can be allowed by the uniform discharge due to the fast electron drift velocity. In addition, the discharge uniformity is not affected by the residual charge because a diffused streamer discharge takes place in a discharge tube. This scheme does not require a preionization system or a fast gas flow system [60–62]. Since the longitudinal excitation scheme has essential advantages of lower cost and greater compactness than the transverse excitation scheme, a simple, compact, and affordable pulsed gas laser can be realized.

The discharge switch is the most important part of the discharge-pumped pulsed laser to rapidly switch out the high voltage pulse for efficient pumping. High voltage switches such as a spark gap and a thyratron have been usually utilized for TEA CO_2 laser to generate short-pulsed discharge. A spark gap switch is simple and low cost, consisting of

two conducting electrodes separated by a gap usually filled with a gas such as nitrogen. This is designed to allow the electric spark to pass between the conductors. Uno et al. use a spark gap switch that is capable to switch out of the high voltage with a fast rise time of less than 100 ns for the operation of the longitudinally excited gas laser [60–62]. However, the spark gap switch is operated in the arc mode, and it suffers from the recovery problem, causing short service life and low efficiency for the high-repetition operation. In addition, electrodes corrosion is the most common form of damage in the spark gap switch caused by the repeated heavy discharge. Like a spark gap switch, thyratron is also a gas-filled switch. Thyratron shows high performance when working in high repetitive operation because of its faster deionization time. However, thyratron is expensive and has limited service time as well due to electrode erosion and fill gas degradation. Both switches can no longer meet the demands for industrial mass production by TEA CO_2 laser.

Current fabrication technology for high-power semiconductors easily makes devices with high breakdown voltage, high current handling, high efficiency in highly repetitive operation, and fast switching times. The solid-state switch presents significant advantages, compared to the spark gap and thyratron, such as a long lifetime, faster switching time, and stable for high-repetition operation. As the result of recent technological advances in semiconductor power devices, the solid-state switch has been applied to gas laser excitation and plasma generation [63]. However, the solid-state switch having the capability to drive the high voltage and large current that is available in the market today is a high-cost product. It prohibits the progress of the pulsed CO_2 laser for the company in the manufacturing, particularly, small and medium-sized companies. Therefore, an affordable and flexible fast high-voltage solid-state switch (FHVSS) has been required for the pulsed gas lasers. In other words, a combination of a longitudinally excited laser with a FHVSS is a promising approach for realizing industrial mass production using a pulsed CO_2 laser.

Throughout these appendices, a simple and flexible method to realize the pulsed CO_2 laser driven by laboratory-developed FHVSS is presented. The longitudinal excitation scheme has been selected in this study. FHVSS consists of a single gate drive circuit and series-connected IGBTs, which is capable to replace the spark gap switches and thyratrons. Laser oscillation has been successfully demonstrated using FHVSS at 10.6 μm. A simple and compact pulsed CO_2 laser has been demonstrated and presented in this dissertation.

Appendix A: Fast high-voltage solid-state switch (FHVSS)

A.1 Overview

Current fabrication technology for high-power semiconductors easily makes devices with high breakdown voltage, high current handling, high efficiency in highly repetitive operation, and fast switching times. Examples include the metal-oxide-semiconductor field-effect transistor (MOSFET) and insulated-gate bipolar transistor (IGBT). To meet the demand for a simple and low-cost solid-state switch having a high voltage rating and fast switching time that can also provide stable operation, laboratory-made fast high-voltage solid-state switch (FHVSS) has been developed. A simple, low-cost, and flexible method to produce FHVSS that can switch out multiple kilovolts in several tens of nanoseconds is presented in this chapter.

A.2 Avalanche transistor circuit

In general, the charging speed of the large input capacitance needed by a MOSFET or an IGBT determines the switching time. Therefore, the construction of the gate drive circuit is important for realizing fast switching in both semiconductor devices. Due to the demand for physically small circuits with low cost, the method reported by Baker et al., which involves the connection of an avalanche transistor circuit to a MOSFET gate, was applied to achieve fast switching in several nanoseconds.

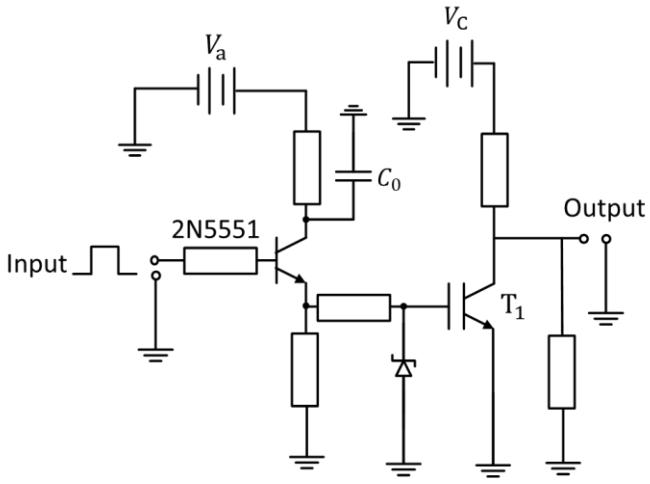

Figure A-1 Schematic circuit diagram of single IGBTT (T_1) coupled with an avalanche transistor circuit.

Figure A-1 shows the circuit for demonstrating fast switching IGBT by using an avalanche transistor circuit. Commercially IGBT, IRG7PH42UD (1,200 V, 80 A) with an

input capacitance of approximately 3,338 pF was used because it is inexpensive and readily on the Internet. The avalanche transistor is connected to the IGBT (T_1) to provide a pulse with a fast rise time to charge the input capacitance of T_1. The avalanche transistor 2N5551 was selected because it is inexpensive and readily available on the Internet. The 2N5551 generates an avalanche effect at reverse voltage V_a of 280 V or greater. When V_a exceeding 280 V triggering pulses from the pulse generator is applied to the avalanche transistor circuit, the 2N5551 is operated in the avalanche mode and a switching time of 5 ns or lower is easily achievable. However, consideration of the amount of capacitance C_0 that is connected to the collector of the avalanche transistor is necessary. C_0 must be large enough to supply the amount needed to turn on T_1. In addition, a Zener diode was connected between the gate and the emitter of T_1 to protect the gate from excessive voltage.

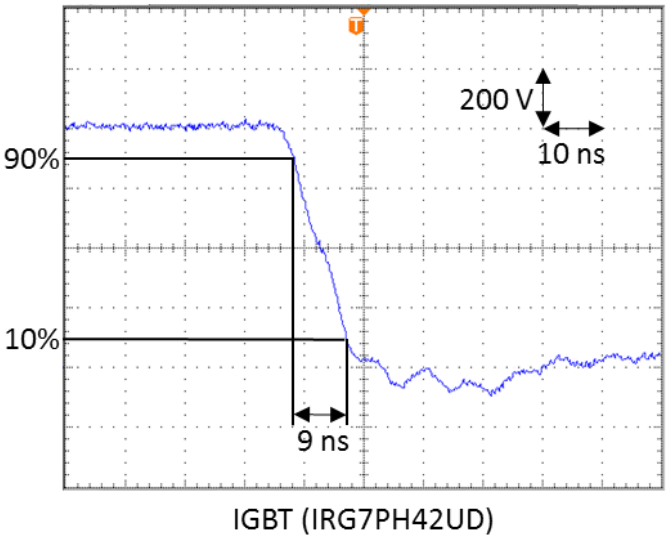

Figure A-2 Switching waveform of FHVSS using IGBT (1-stage)

The charge stored in C_0 delivers a voltage pulse with a rise time of nanoseconds to the gate of T_1 when the avalanche transistor turns on. The input capacitance of T_1 is quickly charged by the voltage pulse, then causing T_1 to turn on rapidly. In this experiment, V_C, V_a and C_0 were set to be 2400 V, 300 V, and 680 pF, respectively. The pulse generator (Agilent 33220A) generated input pulses with a pulse width of 100 μs and frequency of 1 Hz. Figure A-2 shows the switching waveform of the single IGBT measured at the collector of T_1 using a high voltage probe (Tektronik TDS 3054C). A switching time of 9 ns was achieved at 10-90% from the output voltage of 800 V. Based on the specification datasheet of the IGBT, the switching time of the IGBT is 15 ns during standard operation. In this regard, the gate drive circuit made by using an avalanche transistor improves switching performance simply and cost-effectively.

A.3 Fast high-voltage solid-state switch using MOSFET

A commercially available MOSFET, 2SK3301 (900 V, 1 A) with an input capacitance of about 165 pF is used because it is inexpensive and easily available on the web for about 70 JPY. Figure A-3 shows the circuit topology for FHVSS using MOSFET. Five MOSFETs are connected in series to drive about 5 kV of DC voltage. Capacitors (C_1−C_4) are set to be 100 pF. Resistors are connected in parallel to the drain-source of each MOSFET to allow equal biasing at all stages. A Zener diode was connected between the gate and the emitter of each MOSFET to protect the gate from excessive voltage. Avalanche transistor circuit is connected to the gate terminal of M_1 to charge the input capacitance rapidly and enhance the switching speed of the solid-state switch.

This FHVSS was operated in a multi-step sequence by triggering pulses from a single-gate circuit using the avalanche transistor. The basic theory of multistage switching is explained as follows. When the bottom gate of M_1 turns on, the voltage difference between the ground and the source of M_2 is generated. The capacitors that are connected between the gate terminal of every MOSFET are discharged from C_1 to C_4, then turned on the MOSFET from M_2 to M_5 in sequence, finally switches out the high voltage.

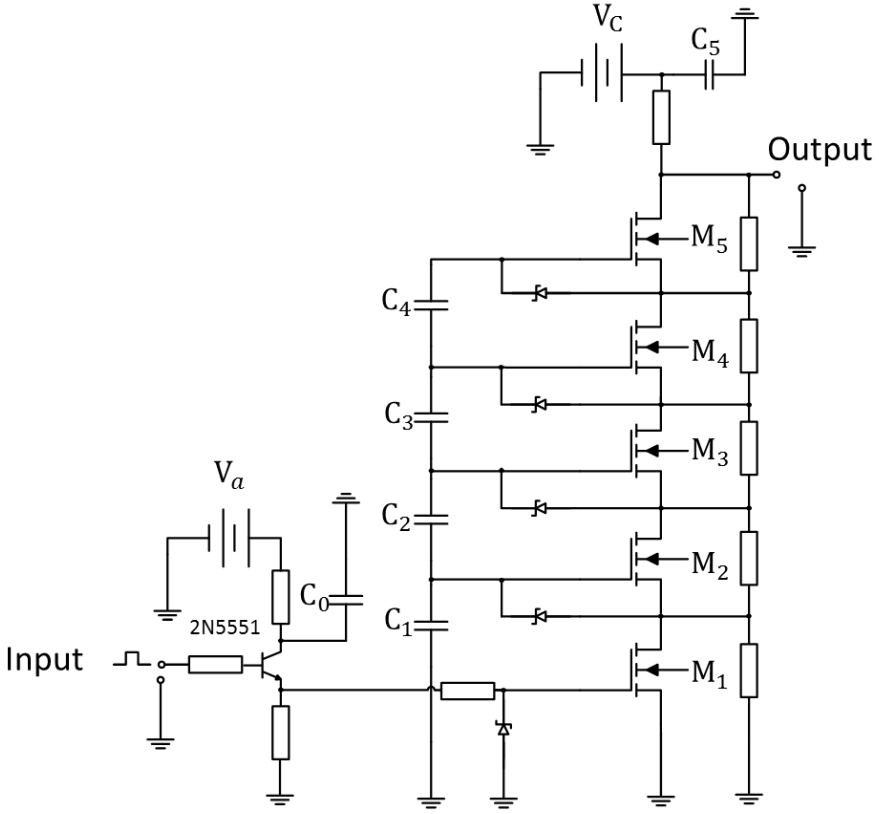

Figure A-3 Schematic circuit diagram of FHVSS using MOSFETs (5-stages)

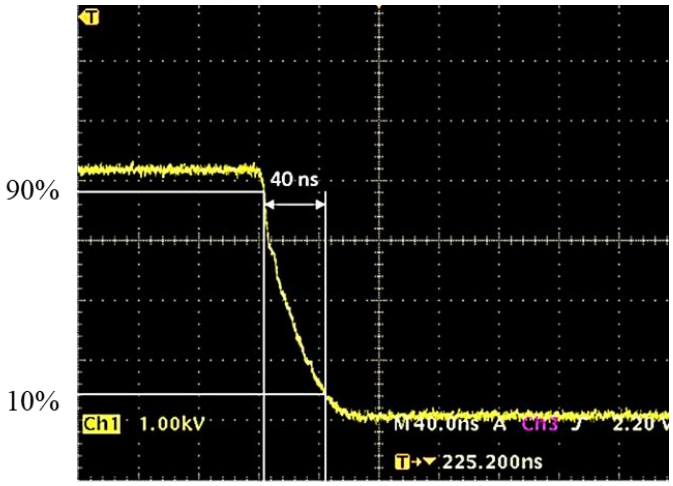

Figure A-4 Switching waveform of FHVSS using MOSFETs (5-stages)

The switching characteristic of FHVSS consisted of avalanche transistor circuit and series-connected MOSFET is measured at the collector of M_5 using high voltage probe (Tektronik TDS 3054C). Figure A-4 shows that the voltage fell from 90% to 10% in 40 ns when 5 kV of DC voltage is applied. Generally, MOSFETs rated at over 1 kV and 20 A are inexpensive and can achieve a switching time of several nanoseconds. However, since MOSFETs must be connected in series for applications with several kilovolts or more, the influence of high on-resistance during switching performance cannot be ignored.

A.4 Fast high-voltage solid-state switch using IGBT

IGBTs have no on-resistance limitation when connected in series; thus, they have an advantage for the construction of solid-state switches and can replace spark gap and thyratron switches in pulsed laser applications. By connecting several IGBTs in series, a solid-state switch with high working voltage and fast switching time can be realized.

The circuit topology of an FHVSS consisting of avalanche transistor and series-connected IGBTs is shown in Fig. A-5. *n* in FHVSS circuit configuration shown in Fig. A-5, represents the number of stages of IGBT. The operating voltage of FHVSS is determined by the collector-emitter voltage of a single IGBT and the number of stages of IGBT.

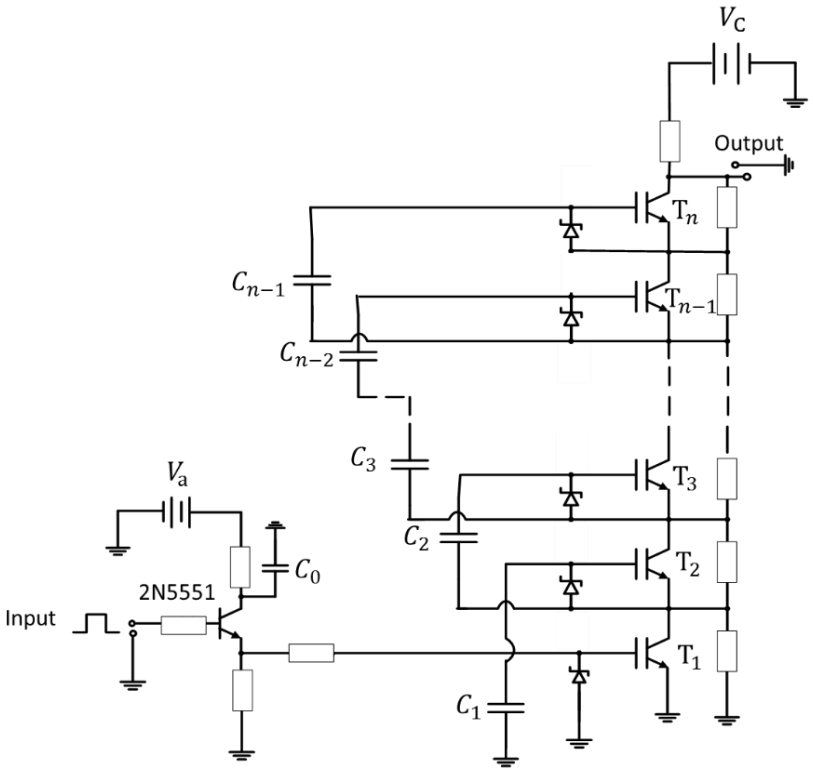

Figure A-5 Schematic circuit diagram of FHVSS using IGBTs

The operation method of FHVSS is explained as follows. DC voltage, V_C is applied between the collector of T_n and ground. At the same time, all the capacitors $(C_1 - C_{n-1})$ connected to the gate terminal of each IGBT $(T_1 - T_n)$ are charged. The voltage pulses with a rise time of nanoseconds produced by the avalanche transistor quickly charge the input capacitance of T_1, then T_1 turns on rapidly. When T_1 turns on, a voltage potential is generated between the gate and emitter of T_2 in the second stage. At that moment, when the terminal voltage of C_1 is sufficiently high enough to drive the gate of T_2, T_2 is turned on due to the discharge of C_1. Repeating this process allows the successive activation of IGBTs sequentially from T_3 to T_n.

Commercially available discrete IGBT (IRG7PG42UD, IRG7PG35UPb) with a collector-emitter voltage of 1200 V has been selected. The input capacitance of IRG7PG42UD[4)] and IRG7PG35UPb are 3338 pF and 1940 pF, respectively. To verify the capability of FHVSS to operate at high working voltage by the method of increasing the number of stages of IGBT, two FHVSS consisting of 5-stages and 8-stages were constructed. The operating voltage for FHVSS consisted of 5-stages and 8-stages of IGBT were estimated to be 7 kV and 10 kV, respectively.

In the FHVSS, it must be noted that the consideration of the amount of capacitance C_0 that is connected to the collector of the avalanche transistor is necessary. C_0 must be large enough to supply the amount of charge needed to turn on T_1. The value of C_0 was

experimentally set to be 680 pF. Moreover, the gate capacitors ($C_1 - C_{n-1}$) play an important role in multistage switching. The amount of gate capacitance is determined by the voltage across the gate terminal of each IGBT. As the stage level increases, the voltage across the gate terminal of IGBT ($T_2 - T_n$) is getting higher. In this regard, the amount of gate capacitance required for turning on the IGBTs from T_2 to T_n is getting smaller. Thus, selecting an appropriate capacitance is advantageous for achieving a faster switching time. The amount of capacitance connected to the gate terminal of IGBTs was summarized in Tables A-1 and A-2. In addition, a Zener diode was connected between the gate and the emitter of each IGBTs to protect the gate from excessive voltage. The resistor was connected parallel to the collector-emitter of each IGBT to allow equal biasing at all stages.

Table A-1 Capacitance value in FHVSS consisted of 5-stages of IGBT (IRG7PG42UD)

C_0	680 pF
C_1	220 pF
C_2	167 pF
C_3	130 pF
C_4	100 pF

Table A-2 Capacitance value in FHVSS consisted of 8-stages of IGBT (IRG7PG35UPb)

C_0	680 pF
C_1	430 PF
C_2	330 pF
C_3	220 pF
C_4	167 pF
C_5	147 pF
C_6	133 pF
C_7	100 pF

Figure A-6 shows the switching characteristic of FHVSS measured at the collector of T_n using the high-voltage probe (Tektronix P6015A) having a frequency response of 75 MHz. The switching time is evaluated from 10-90% of the output voltage. From the result shown in Fig. A-6, we can see that the operating voltage of FHVSS can be increased easily by increasing the number of stages of IGBT. Despite increases in the number of stages of IGBT, the switching time of FHVSS in several nanoseconds still can be maintained. Developed FHVSS that can switch out a high voltage in several nanoseconds, which is almost the same as the performance of spark gap switch can be implemented in the longitudinally excited CO_2 laser. In addition, this FHVSS is simple and affordable because a gate drive circuit is not required for each IGBT and low-priced IGBTs are used.

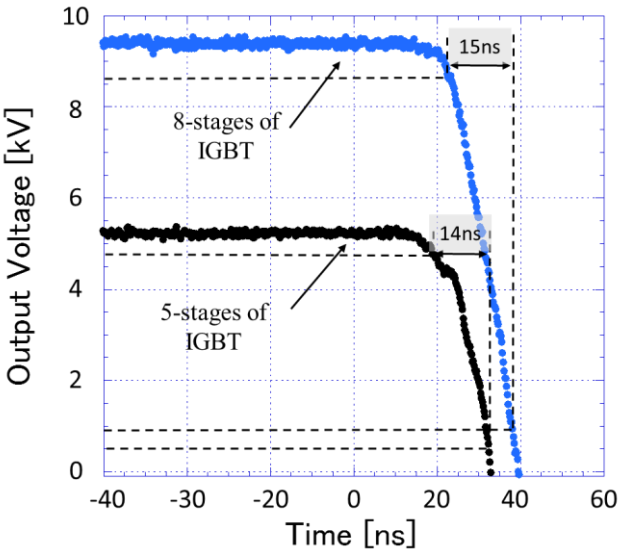

Figure A-6 Switching waveform of FHVSS consisting of 5-stages and 8-stages of IGBTs

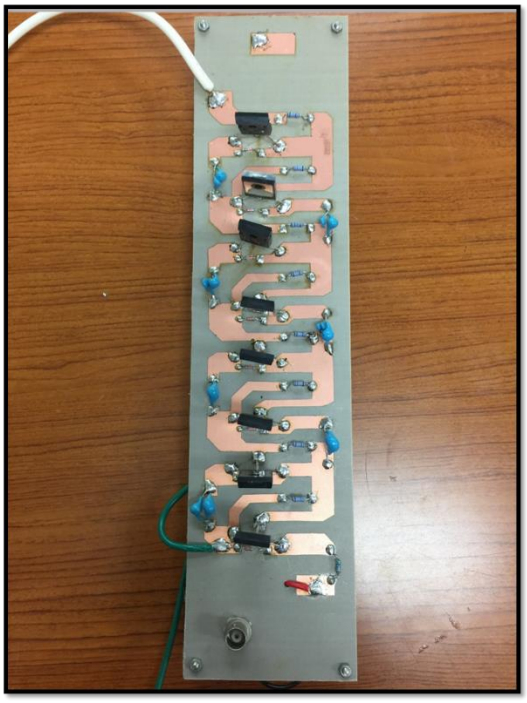

Fig. A-7 Picture of series-connected of IGBTs

A.5 Summary

In this chapter, simple, low-cost, and flexible FHVSS consisting of avalanche transistor circuits and series-connected MOSFET or IGBT have been demonstrated. FHVSS has great flexibility for increasing the drive voltage in principle. In addition, FHVSS is compact because a gate drive circuit for each IGBT is not required. For the construction of FHVSS, IGBT is more preferable than MOSFET because the on-resistance does not affect the series connection of IGBT. This allows the construction of a series connection of IGBT

for the operation that involves several tenths of kilovolts. By using an avalanche transistor for the gate drive circuit, fast switching has been achieved despite the series-connected operation. Moreover, the circuit made of the avalanche transistor improves switching performance in a simple and cost-effective manner. The allowable operating voltage for the switching can be simply increased by increasing the number IGBTs in a series connection depending upon the desired working voltage. Since the spark gap switch is usually operated at several tens of nanoseconds in switching time at the high voltage around 10 kV, FHVSS can be implemented to the pulsed-gas laser to replace the spark gap switch and function as a discharge switch to provide stable laser oscillation.

Appendix B: Longitudinally excited CO_2 laser controlled by fast high-voltage solid-state switch using MOSFET

B.1 Overview

In this chapter, FHVSS consisted of avalanche transistor circuit and series-connected of MOSFET is installed in longitudinally excitation scheme. FHVSS is connected to the trigger electrode to provide spike energy, then induced the discharge inside the laser tube.

B.2 Experimental method

The longitudinally excited CO_2 laser controlled by an FHVSS is schematically shown in Fig. B-1, consisting of high voltage DC power supply, diode, charging resistor, capacitor, laser tube, and FHVSS. In this experiment, FHVSS consisted of 5 series-connected MOSFETs is used. Metal electrodes were attached to both ends of the discharge tube. A high reflective mirror and ZnSe output coupler with reflectivity of 70% formed a resonator. A mixed (CO_2: 7%, N_2: 14%, He: 79%) gas is filled in a discharge tube with an inner and outer diameter of 13 mm and 17 mm, respectively and it is continuously circulated. The trigger electrode was made of a copper sheet and wrapped at the outer wall of the laser tube. The trigger electrode located between the two main electrodes is connected in series with the FHVSS and labeled as T (see Fig. 4-1). The FHVSS indicated in Fig. B-1, is operated as a trigger switch.

The operation of a longitudinally excited CO_2 laser based on the spike and sustainer technique is explained as follows. DC voltage E_1 was applied to the laser tube. Capacitor C connected parallel with the laser tube as shown in Fig. 4-1 was charged by the current that flows from E_1. At the same time, a positive voltage pulse generated by the pulse generator was used to trigger the FHVSS. E_2 was set to be 5 kV. When the FHVSS is switched, the discharge is induced in the discharge tube, producing laser oscillation. In this experiment, laser output energy was measured with an energy detector (Gentex ED-200), and the voltage waveform was measured with a high voltage probe coupled with an oscilloscope (Tekronik P6015A) having a frequency response of 75 MHz.

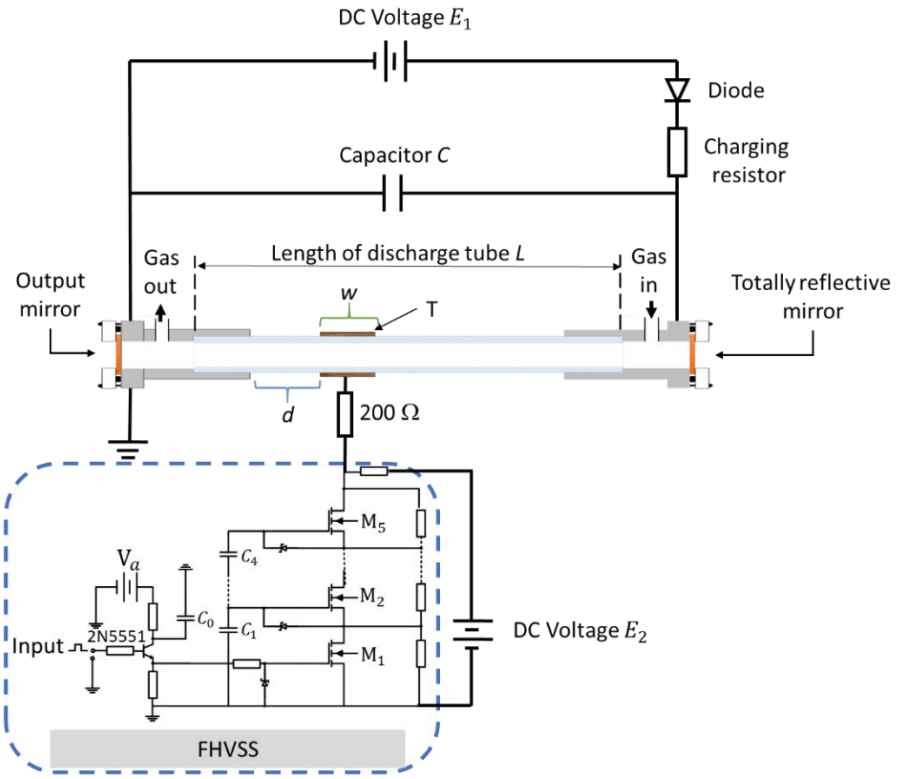

Figure B-1 Schematic diagram of longitudinally excited CO_2 laser controlled by FHVSS using MOSFET

B.2.1 Capacitance between trigger and ground electrode C_d (distance between trigger and ground electrode d)

Figure B-2 shows the schematic diagram to calculate capacitance between trigger and ground electrode C_d. Based on Fig. B-2, a, b, and c represent the inner diameter of the discharge tube, the outer diameter of the discharge tube, and the outer diameter of the intermediate electrode, respectively. (a: 13 mm, b: 17 mm, c: 17.2 mm). To calculate the capacitance C_d formed in between the intermediate and ground electrodes, it is considered to divide into primary capacitance C_1 and secondary capacitance C_2 as shown in Fig. B-2. The area of cylindrical side surfaces S_A are

$$S_A = \pi\left(\frac{b}{2}\right)^2 - \pi\left(\frac{a}{2}\right)^2 \tag{B.1}$$

By using the basic formula of parallel plate capacitor, $C = \varepsilon\frac{S}{d}$, capacitance C_d, formed between the intermediate and ground electrodes can be calculated.

By substituting the area of cylindrical side surfaces S_A, in the basic formula of parallel plate capacitor, primary capacitance C_1 can be calculated.

$$C_1 = \varepsilon\frac{S_A}{d} \tag{B.2}$$

When $\varepsilon = \varepsilon_0\varepsilon_{r1}$, the primary capacitance C_1 is

$$C_1 = \varepsilon_0\varepsilon_{r2}\frac{S_A}{d} \tag{B.3}$$

C_2 was also calculated by using the basic formula of parallel plate capacitor, same as C_1.

$$C_1 = \varepsilon\frac{S_B}{d} \tag{B.4}$$

When $\varepsilon = \varepsilon_0\varepsilon_{r2}$,

$$C_2 = \varepsilon_0\varepsilon_{r2}\frac{S_B}{d} \tag{B.5}$$

C_1 and C_2 were assumed to be connected in parallel. The total capacitance of parallel-connected capacitors is equal to the sum C_1 and C_2.

$$C_d = C_1 + C_2 \tag{B.6}$$

The equation can be expressed in a more definite way

$$C_d = \frac{\varepsilon_0}{d}(\varepsilon_r S_A + S_B) \tag{B.7}$$

where S_A and S_C are an area of cylindrical side surfaces, ε_0 is the permeability of free space, and ε_r is the relative permeability of dielectric material. The permeability of free space is 8.854×10^{-12} [F/m]. Here, the relative permeability of air and pyrex glass are 1 and 4.8, respectively.

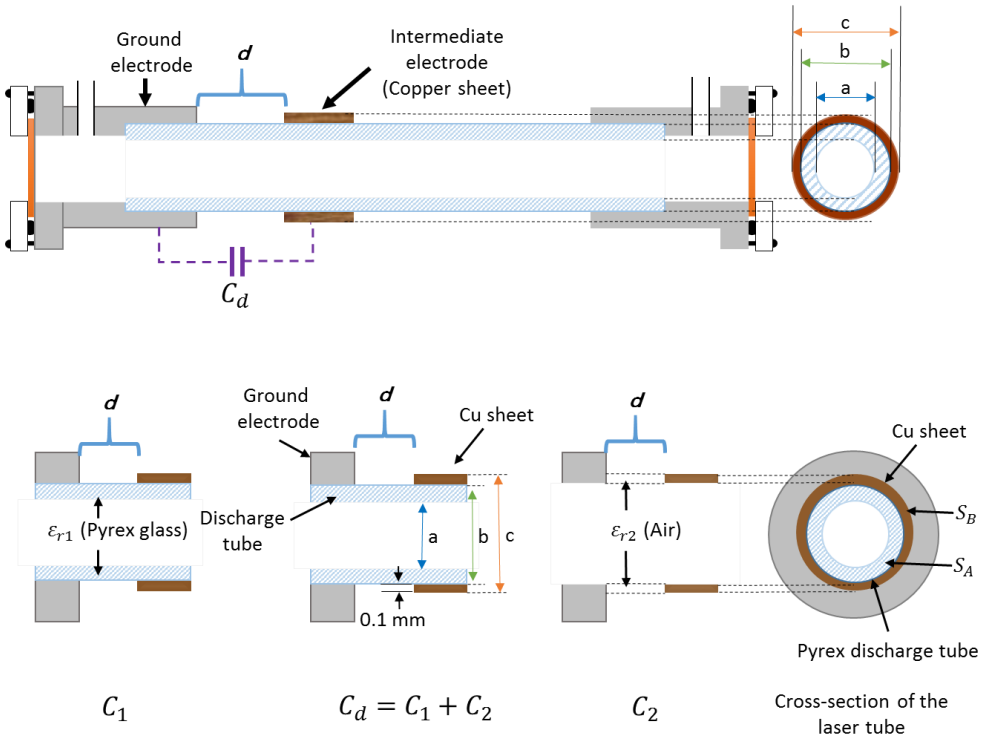

Fig B-2 Schematic diagram to calculate the trigger capacitance C_d

B.2.2 Wall coupling capacitance C_w (length of intermediate electrode w)

Based on Fig. B-3, a and b indicate the inner diameter of the discharge tube and the outer diameter of the discharge tube. (a: 13 mm, b: 17 mm). The wall coupling capacitance C_w can be expressed as

$$C_w = \frac{2\pi\varepsilon_0\varepsilon_r}{ln\frac{b}{a}} w[F] \tag{B.8}$$

where ε_0 is the permeability of free space, ε_r is the relative permeability of dielectric material, and w is the length of trigger electrode. Here, the relative permeability of pyrex glass is 4.8.

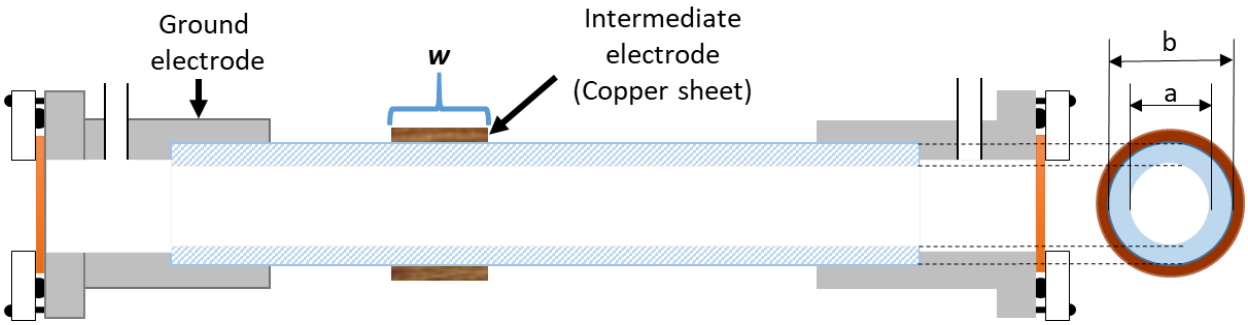

Figure B-3 Schematic diagram to calculate wall coupling capacitance C_w

B.3 Results and Discussions

The discharge tube length was set as a parameter for this experiment. The operating voltage of 30 cm and 40 cm-length discharge tubes to produce laser oscillation were experimentally fixed to be 10 kV and 20 kV, respectively. The characteristics of laser output energy were examined under some parameters which are applied voltage, capacitance C, gas pressure, the capacitance between trigger and ground electrode, and capacitance of wall coupling to find optimum conditions to produce high output energy.

Laser output energy depends on the capacitance C that is connected parallel with the laser tube. Gas pressure, wall coupling capacitance C_w, and trigger capacitance C_d were fixed to be 3.0 kPa, 8 pF cm (w = 1 cm), and 0.65 pF (d = 1 cm), respectively. The capacitance of 570 pF, 700 pF, 900 pF, 1140 pF, 2000 pF, and 2700 pF were used. The electrical energy was estimated. The horizontal axis that shows the electrical energy stored in the C, was calculated by $CV^2/2$, where C and V are the capacitance and applied voltage E_1, respectively. Although the amount of capacitances used in this experiment is the same for both laser tubes with discharge lengths of 40 cm and 30 cm, it must be noted that the calculation of electrical energy is different because the voltage applied to E_1 is different.

Figure B-4 shows the dependence of electrical energy on laser energy. The higher the electrical energy, the higher the laser energy. Laser energy produced by the 40 cm length discharge tube is higher than the 30 cm length due to the longer laser cavity. However, in the

case of a 40 cm-length discharge tube, laser energy decreases as the electrical energy is more than 400 mJ. This shows that laser oscillation becomes unstable due to residual charge when electrical energy is getting higher.

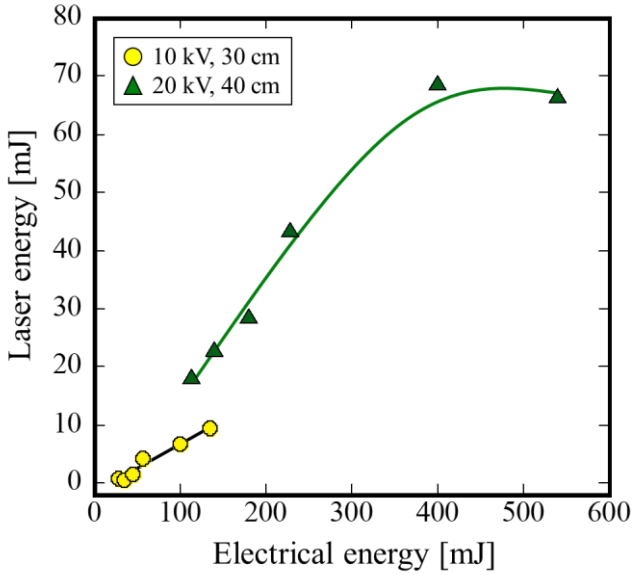

Figure B-4 Dependence of electrical energy on laser energy (L = 30 cm, 40 cm)

Fig B-5 shows the dependence of laser output energy on gas pressure for 30 cm and 40 cm-length discharge tubes. Gas pressure, wall coupling capacitance C_w, and trigger capacitance C_d were fixed to be 700 pF, 8 pF (w = 1 cm), and 0.649 pF (d = 1 cm), respectively. Figure B-5 shows the laser output energy as a function of gas pressure. In addition, the applied voltage E_1 for a 40 cm-length discharge tube is varied. When the gas pressure was supplied at low pressure, the laser output energy becomes low due to low gas density. Laser energy has a peak value of 23 mJ at gas pressure around 3 kPa to 3.5 kPa when 20 kV is being applied (see Fig. B-5).

Laser energy decreases as the gas pressure flowed more than 3.5 kPa. Laser energy increases with an increase in gas pressure until it reaches the peak value at optimum gas pressure. However, when the gas pressure flowing inside the laser tube is more than the optimum gas pressure, laser energy decreases due to the high discharge impedance caused by high gas density. Also, from Fig. B-5, when the voltage applied to the 40 cm-length discharge tube is increased, the optimum gas pressure increases. This can be explained by using Paschen's law equation, where $V = pd$. Here, we can assume that V, p, and d denote represent applied voltage, gas pressure, and discharge length, respectively. As the discharge length remains constant, when the applied voltage increases, the gas pressure increases. We can conclude that the optimum pressure depends on the applied voltage and discharge length.

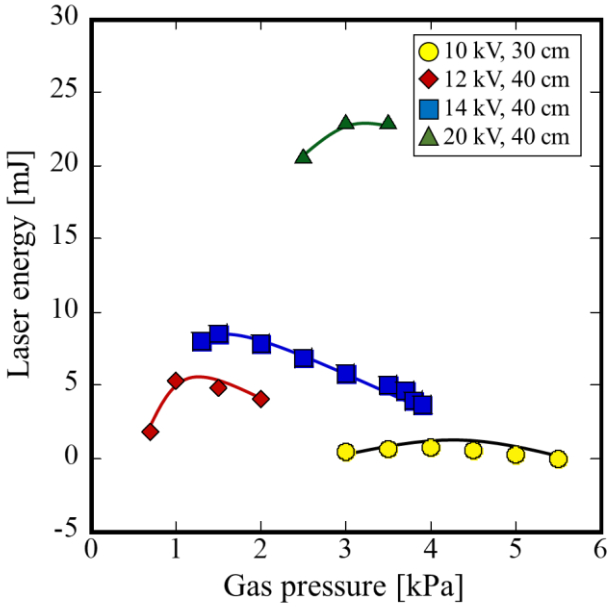

Figure B-5 Dependence of gas pressure on laser energy (L = 30 cm, 40 cm)

In this experiment, 40 cm-length of discharge tubes were used. The applied voltage, capacitance C, and length of wall coupling capacitance C_w were fixed to be 20 kV, 700 pF, and 8 pF (1 cm), respectively, to examine laser energy dependence on trigger capacitance C_d. Distance between the trigger and ground electrode which are 0.5 cm, 1.0 cm, 1.5 cm, and 2.0 cm corresponds to the 0.65 pF, 0.32 pF, 0.22 pF, and 0.16 pF, of capacitance C_d respectively. As shown in Fig. 4-6, the laser oscillates when the trigger capacitance C_d is within 0.16 pF to 0.65 pF. However, when trigger capacitance is set to less than 0.16 pF (d more than 2 cm), the laser oscillation did not occur. As the trigger capacitance decreases, the charge is insufficient to trigger the discharge. Hence, optimum trigger capacitance C_d is necessary for this laser scheme.

In this experiment, 40 cm-length of discharge tube was used. The applied voltage, capacitance C, and trigger capacitance C_d were fixed to be 20 kV, 700 pF, and 0.65 pF (d=1 cm), respectively. Wall coupling capacitance C_w of 8 pF, 16 pF, 24 pF, and 32 pF were used to examine laser energy dependence on wall coupling capacitance C_w. As shown in Fig. B-7, it can be seen that the laser oscillates when the wall coupling capacitance C_w is within 8 pF cm to 32 pF. When the wall coupling capacitance C_w is set more than 32 pF, the laser oscillation did not occur due to high capacitance. It can be deduced that the amount of coupling capacitance C_w in the range of approximately about 8 pF to 32 pF is required to initiate the discharge inside the laser tube using the FHVSS.

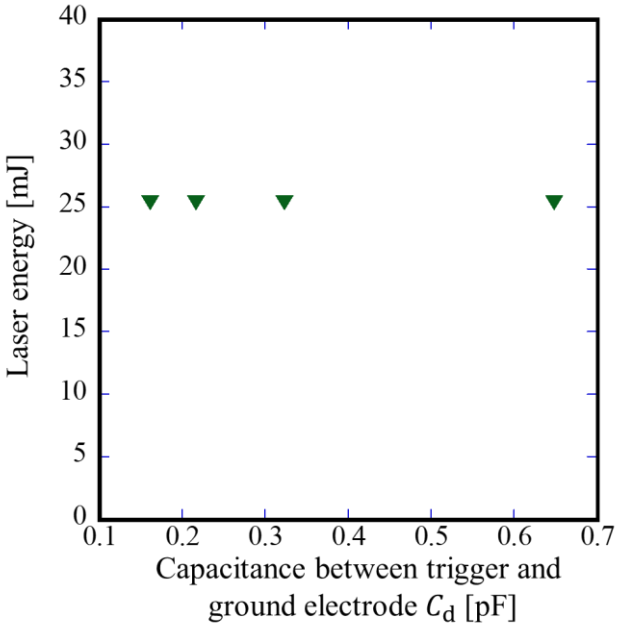

Figure B-6 Dependence of laser energy on trigger capacitance C_d (L = 40 cm)

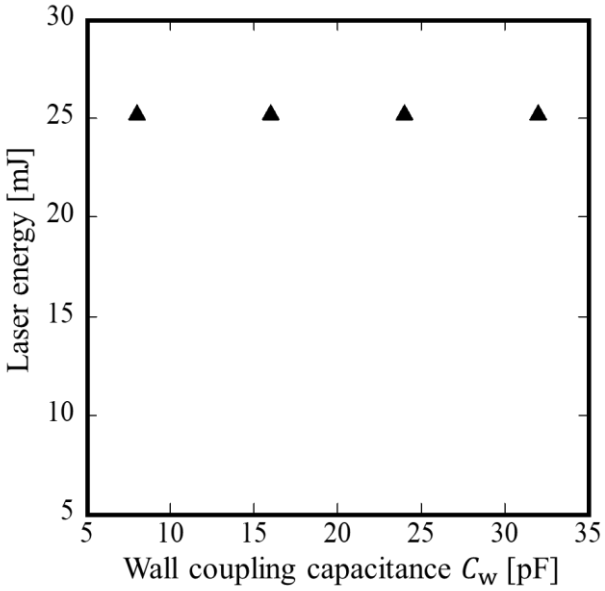

Figure B-7 Dependence of laser energy on wall coupling capacitance C_w (L = 40 cm)

B.4 Summary

A simple longitudinally excited CO_2 laser controlled by FHVSS using the spike and sustainer technique has been developed. FHVSS can provide stable laser operation. Hence, the spark gap switchless operation has been realized. In this laser scheme, the maximum energy of about 60 mJ has been obtained by using a 40 cm-length discharge tube. Based on the results, we can conclude that longer discharge length and higher electrical energy

produced high power of laser oscillation. Additionally, this laser scheme can successfully make an oscillation at several conditions, which include optimum electrical charge, gas pressure, wall coupling capacitance, and capacitance between trigger and electrode.

Appendix C: Longitudinally excited CO_2 laser driven by fast high-voltage solid-state switch using IGBT

C.1. Introduction

A simple and compact longitudinally excited CO_2 laser driven by FHVSS has been presented in this chapter. Compared to the method described in Chapter 4, the laser configuration described in this chapter only requires one DC voltage power supply to operate the laser. This can lead to simplicity and cost-effectiveness for the construction of pulsed CO_2 lasers. FHVSS is employed to induce the main discharge in the laser system presented in this chapter.

It has been reported that Uno et al. used a tandem scheme constituted of two 30 cm-length discharge tubes connected with an intermediate electrode to decrease the operating voltage and to realize a large discharge volume with a short discharge length. The idea of the tandem scheme proposed by Uno et al has been employed in this laser scheme. In addition, the results obtained from the short single scheme are compared with the tandem scheme.

C.2. Longitudinally excited CO_2 laser driven by fast high-voltage solid-state switch using IGBT (Single scheme)

The longitudinally excited CO_2 laser driven by FHVSS consisted of a DC power supply, resistors, a capacitor C_L, a laser tube, and a FHVSS as shown in Fig. C-1. Metallic electrodes and resonator mirrors are attached to both ends of the discharge tube, forming a laser tube. A total reflective spherical mirror with a radius of curvature of 20 m and flat output mirror with a reflectivity of 80% is also attached to both ends of the discharge tube, forming a resonator. A mixed (CO_2:N_2:He = 1:1:2) gas is filled in the laser tube and it is continuously circulated.

The operation of longitudinally excited CO_2 laser driven by FHVSS is explained as follows. DC voltage V_C is applied to the FHVSS and a capacitor C_L that is connected in series with the laser tube is. Capacitor C_L is charged by the current that flows from the DC voltage power supply. When the FHVSS is rapidly switched out, the charges stored in C_L are quickly discharged, then the voltage difference between the laser tube and the ground is generated. Rapid discharge takes place in the laser tube, producing laser oscillation. In this experiment, laser output energy was measured with an energy detector (Gentex ED-200), and the voltage waveform was measured with a high voltage probe coupled with an oscilloscope (Tekronik P6015A) having a frequency response of 75 MHz.

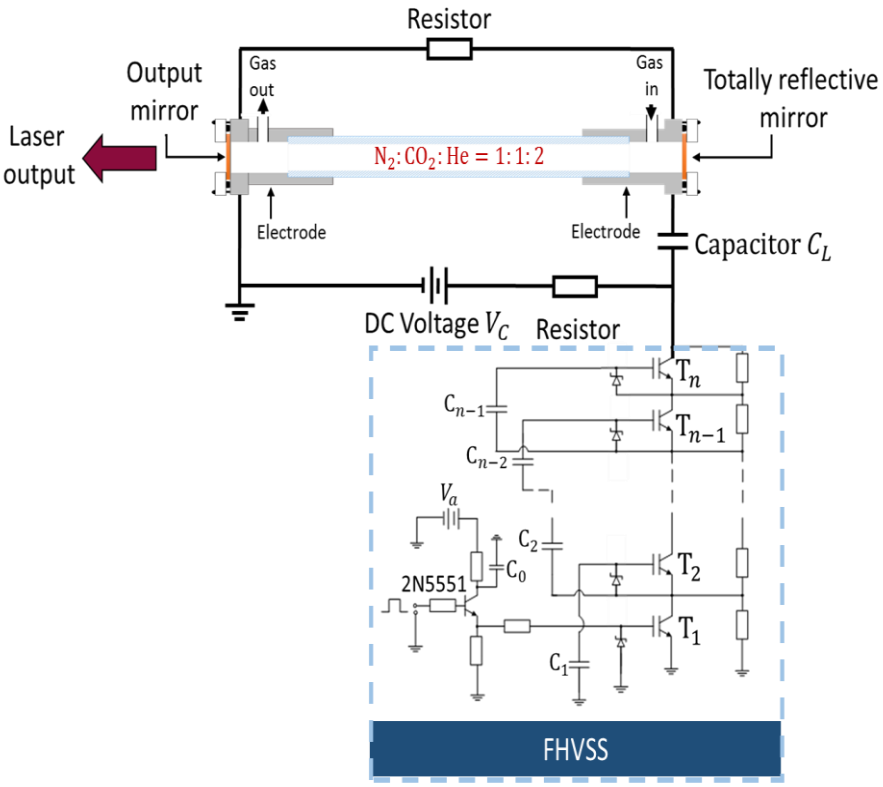

Figure C-1 Schematic diagram of longitudinally excited CO_2 laser driven by FHVSS using IGBTs

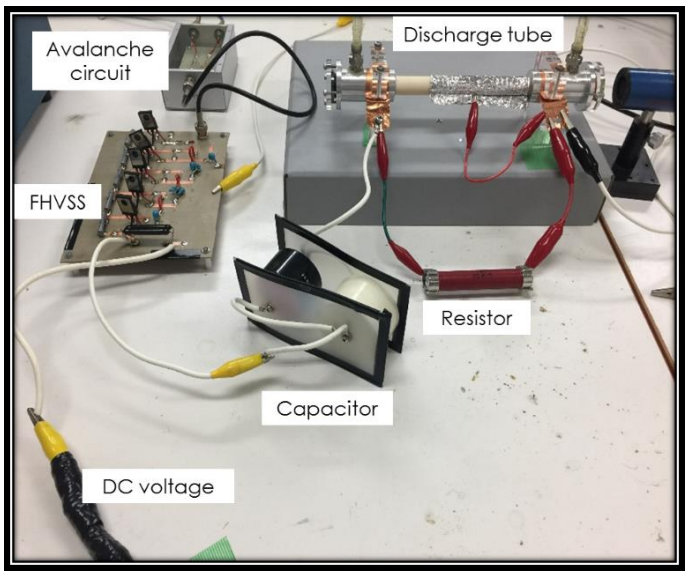

Figure C-2 Picture showing the designed laser system used during the characterization of the laser

C.3. Results and discussions on comparison between 20 cm and length and 30 cm-length discharge tube in a single scheme

The operating voltage needed to initiate the discharge process inside the laser tube depends on the length of the discharge tube. A longer discharge length requires a higher operating voltage. The operating voltage of 20 cm and 30 cm-length discharge tubes were experimentally fixed to be 7 kV and 10 kV, respectively. In consequence, FHVSS consisted of 5-stages of IGBT is used to operate 20 cm-length discharge tube. Meanwhile, FHVSS consisted of 8-stages of IGBT is used to operate a 30 cm-length discharge tube. Both lasers were successfully oscillated and produced laser energy of several mJ.

5-5-1 Relation between gas pressure, discharge current, and laser output energy

Figure C-3 shows the dependence of laser output energy on gas pressure. This experiment was also carried out to find out the laser energy varied with the length of the discharge tube. In this case, C_L was fixed to be 2000 pF. Laser output energy reaches a maximum value of 3 mJ at a gas pressure around 1.3 kPa for a 20 cm-length discharge tube. On the other hand, laser output energy reaches a maximum value of 12.8 mJ at gas pressure around 2.8 kPa for a 30 cm-length discharge tube. When the gas pressure flowed inside the laser tube is low, the laser energy decreases due to low gas density. However, when the gas pressure is more than the optimum gas pressure needed inside the laser tube, laser energy decreases due to the high discharge impedance caused by high gas density. Therefore, the optimum gas pressure is needed to produce high laser energy. Laser output energy for the laser system consisted of 30 cm-length discharge tube is higher than 20 cm-length discharge tube is due to the longer discharge length. The longer the discharge length, the larger the laser output energy. However, a longer discharge length requires a high operating voltage for laser oscillation.

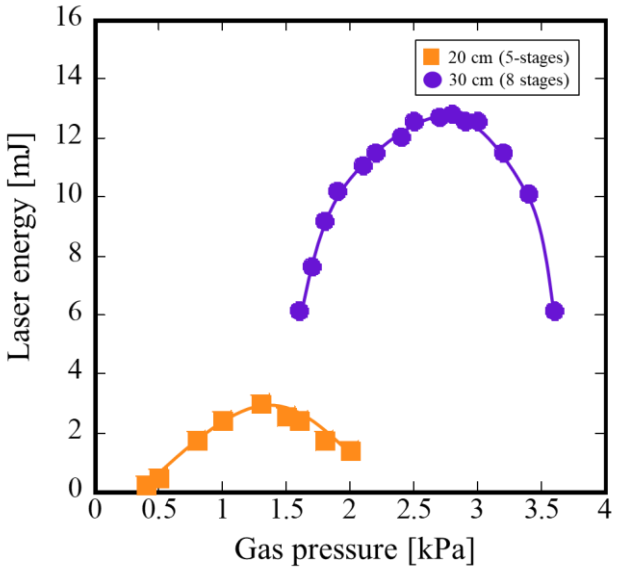

Figure C-3 Dependence of gas pressure on laser energy (L = 20 cm, 30 cm)

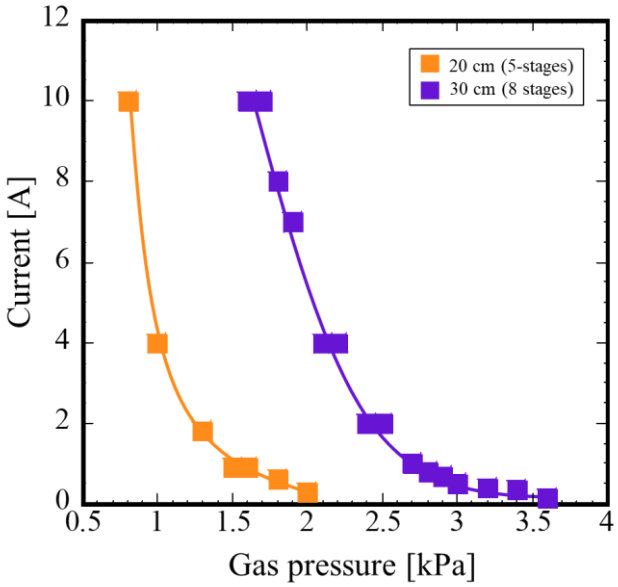

Figure C-4 Dependence of gas pressure on current (L = 20 cm, 30 cm)

The discharge current dependence on the gas pressure was observed. Figure C-4 shows the dependence of gas pressure on discharge current in 20 cm and 30-cm length discharge tubes. In this case, C_L was fixed to be 2000 pF. We can see clearly that the discharge current is decreased when the gas pressure inside the laser tube increased. This is due to the high discharge impedance inside the laser tube caused by high gas density.

Figure C-5 shows the relation between gas pressure, discharge current, and laser energy of the longitudinally excited CO_2 laser with a discharge length of 30 cm. In this case, C_L was fixed to be 2000 pF. The discharge current flow inside the laser tube is lower when the gas pressure is higher. Laser output energy reaches a maximum value of 12.8 mJ at gas pressure around 2.8 kPa and a discharge current of about 1A. The optimum gas pressure is needed to produce high laser energy.

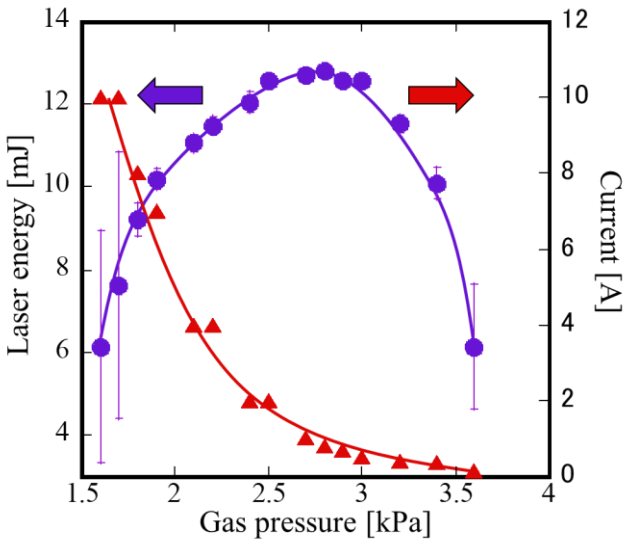

Figure C-5 Relation between gas pressure, current, and laser energy (L = 30 cm)

5-3-3 Relation between electrical energy and laser output energy

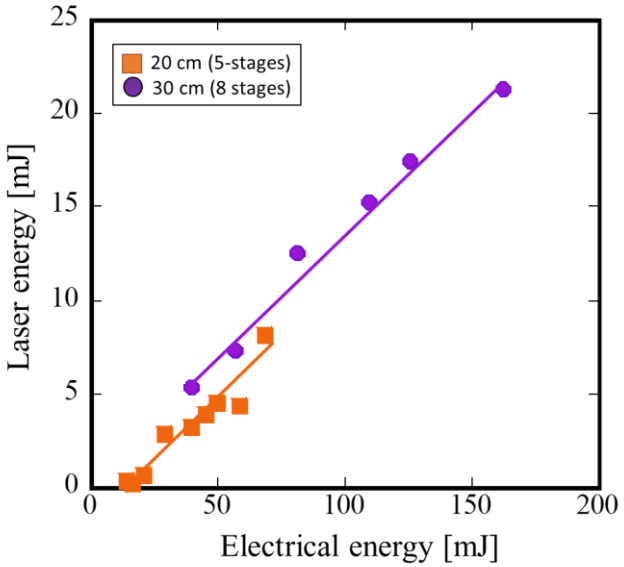

Figure C-6 Influence of electrical energy on laser energy

Figure C-6 shows the dependence of laser output energy on electrical energy. The gas pressure inside the 20 cm and 30 cm-length of discharge tube were kept constant at 1.3 kPa and 2.8 kPa, respectively. The horizontal axis that shows the electrical energy stored in the C_L, was calculated by $CV^2/2$, where C and V are the capacitance and applied voltage, respectively. The results obtained indicate that laser energy increases with increasing electrical energy. The energy efficiency for 20 cm and 30 cm-length discharge tube were

estimated to be 12.5% and 13.2%, respectively, from the fitting line to the data shown in Fig. C-6.

5-3-3 Relation between capacitance C_L and pulse width of discharge waveform

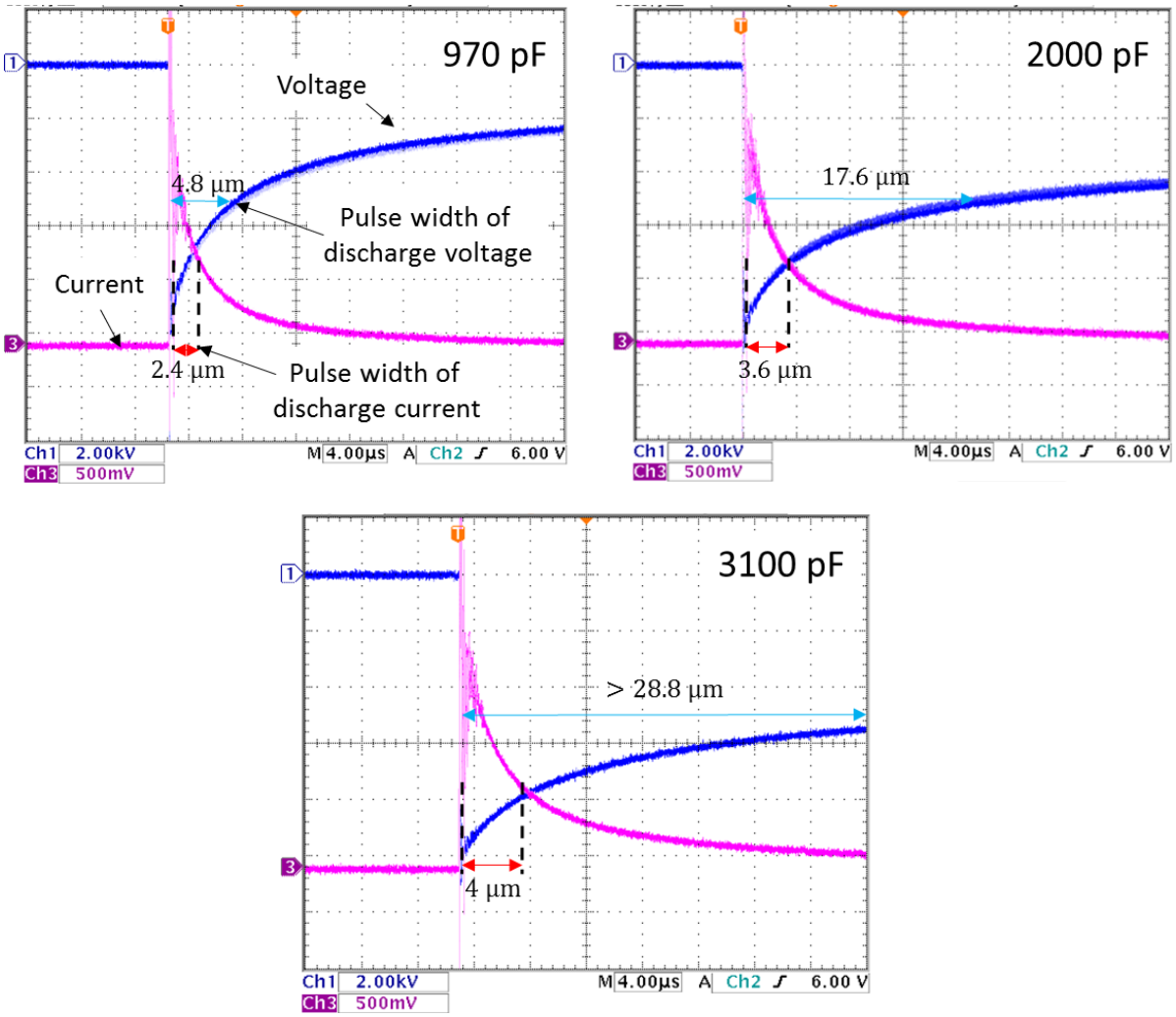

Figure C-7 Waveform of discharge voltage and current (L = 30 cm)

Figure C-7 shows the waveform of voltage and current in a laser system with a 30-cm length discharge tube were observed at the time scale of 4 µs. The gas pressure inside the laser tube was kept constant at 2.8 kPa. Based on the picture of waveforms shown in Fig C-7, we can see clearly that the pulse width of discharge voltage and discharge current increases when increasing in electrical energy. A large amount of capacitance took a long time for charging. However, the longer charging time does not solely depend on the amount of capacitance. The gas pressure inside the laser tube also affects the charging time of capacitance. The increase in the pulse width of discharge current can be explained by using a formula, $Q = It$, where Q is the amount of charge, I is the amount of current flow and t is

time. When the current flow remains constant, the pulse width of the current increases as the amount of capacitance increases.

C.4. Longitudinally excited CO_2 laser driven by fast high-voltage solid-state switch using IGBT (Tandem scheme)

The schematic illustration of a longitudinally excited CO_2 laser driven by an FHVSS is shown in Fig. C-8, consisting of a high voltage DC power supply, resistors, capacitor, laser tube, and FHVSS. The tandem scheme is constituted of two ceramic discharge tubes of the same length and connected to an intermediate electrode. The inner and outer diameters of the discharge tube are 13 mm and 17 mm, respectively. The two discharge tubes with a length of 20 cm each were used. Metallic electrodes and resonator mirrors are attached to both ends of the discharge tube, forming a laser tube. Both electrodes were connected to the ground. A total reflective spherical mirror with a radius of curvature of 20 m and flat output mirror with a reflectivity of 80% is also attached to both ends of the discharge tube, forming a resonator. Therefore, the active length of this tandem scheme was 50 cm (Active length was measured from the output mirror to the total reflective mirror). A mixed (CO_2:N_2:He = 1:1:2) gas is filled in the laser tube and it is continuously circulated. Developed FHVSS that consisted of 5-stages of IGBT (IRG7PH42UD) that can be operated at 7 kV of DC voltage is used in this experiment.

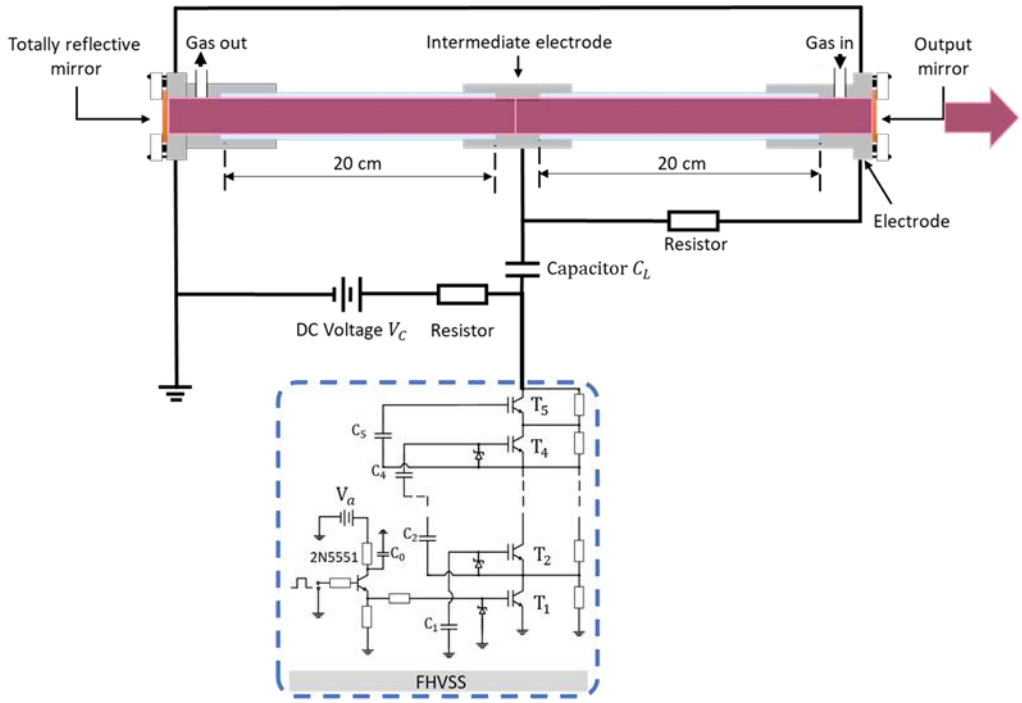

Fig. C-8 Schematic diagram of longitudinally excited CO_2 laser driven by FHVSS using IGBTs in the tandem scheme

The operation of longitudinally excited CO_2 laser driven by FHVSS in a tandem scheme is explained as follows. DC voltage is applied to the FHVSS and a capacitor C_L that is connected to the intermediate electrode. Capacitor C_L is charged by the current that flows from the DC voltage power supply. The DC voltage power supply also charges the capacitors in the FHVSS. When the FHVSS is rapidly switched out, the charges stored in C_L is quickly discharged, then the voltage difference between the laser tube and the ground is generated. Rapid discharge takes place in the laser tube, producing laser oscillation. In this experiment, laser output energy was measured with an energy detector (Gentex ED-200), and the voltage waveform was measured with a high voltage probe coupled with an oscilloscope (Tekronik TDS 3054C).

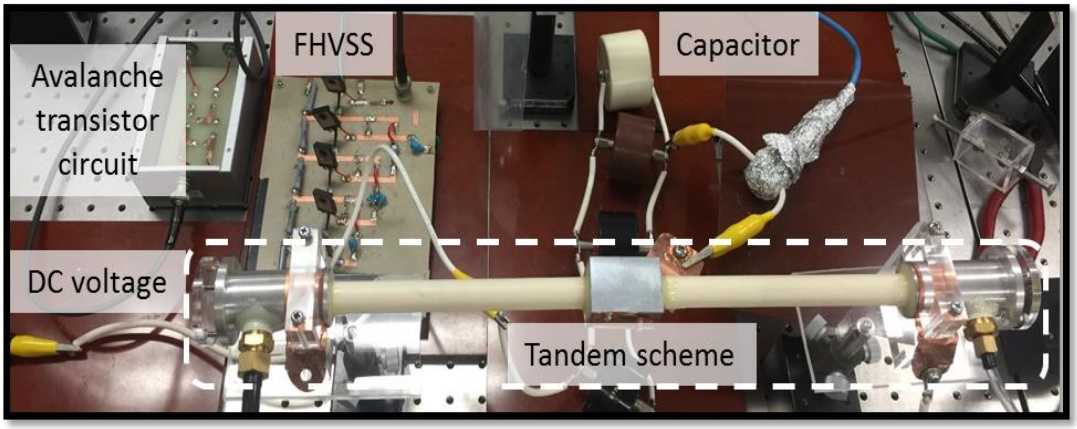

Figure C-9 Picture showing the laser system in the tandem scheme

C.5. Results and discussions on comparison between single scheme (L = 20 cm) and tandem scheme

To compare the significance of each laser scheme. The operating voltage for both schemes was experimentally fixed to be 7 kV and FHVSS consisted of an avalanche transistor circuit and five series-connected of IGBT (IRG7PH42UD) is utilized.

Figure 5-10 shows the dependence of laser output energy on gas pressure in a single and tandem scheme. In this case, C_L was fixed to be 2000 pF. Laser output energy reaches a maximum value (marked with a circle-dotted line in Fig. 6-3) of approximately 3 mJ and 1.3 mJ for single and tandem schemes, respectively. When the gas pressure flowed inside the discharge tube is low, the laser output energy decreases due to low gas density. When the gas pressure flowed inside the laser tube is more than the optimum gas needed, laser output energy decreases due to the high discharge impedance caused by high gas density. The single scheme shows a peak value at 1.3 kPa, whereas the tandem scheme shows a peak value at 1 kPa. The optimum gas pressure for a tandem scheme is lower than a single scheme.

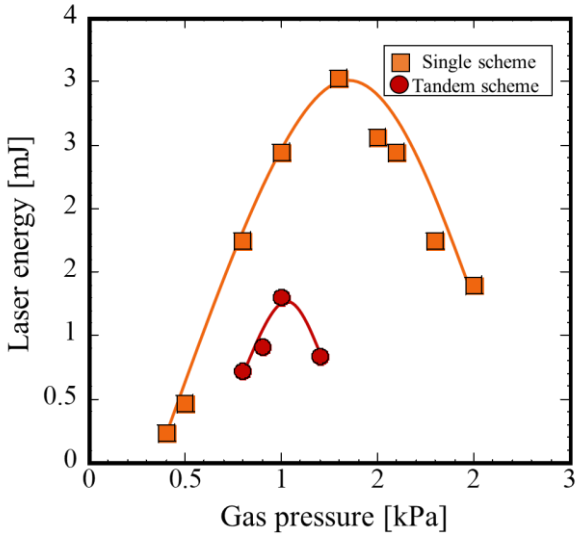

Fig. C-10 Relation between gas pressure and laser energy in single and tandem scheme

As shown in Fig. C-10, the pressure range in a tandem scheme that allows laser oscillation to occur is between 0.8 kPa to 1.2 kPa. On the other hand, the pressure range in a single scheme that allows laser oscillation to occur is between 0.8 kPa and 2 kPa. The discharge current that flows inside both laser schemes was measured and plotted, as indicated in Fig. C-11 and Fig. C-12. From the results shown in Fig. C-11, it can be seen that the discharge current flows through the anode in the single scheme at 0.8 kPa and 1.2 kPa are 7.6 A and 0.8 A, respectively. However, the results shown in Fig. C-12 shows that the discharge current flows through the intermediate electrode in the tandem scheme at 0.8 kPa and 2 kPa, are 24 A and 0.3 A respectively. The pattern is shown in Fig. C-11 and Fig. C-12 were almost the same. However, the range of gas pressure that allows laser oscillation in a tandem scheme is smaller than a single scheme.

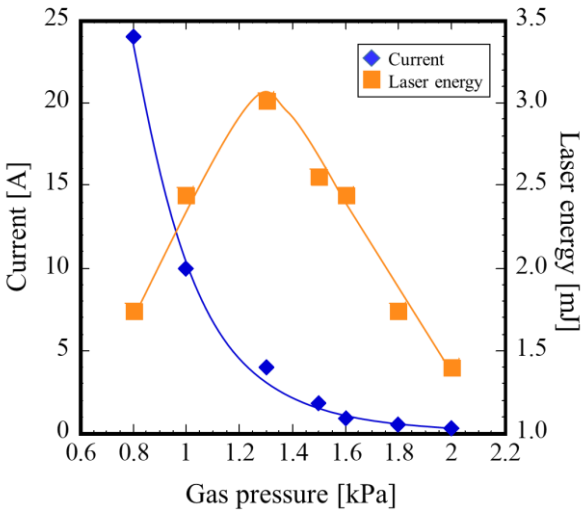

Fig. C-11 Relation between gas pressure, discharge current and laser energy in a single scheme (L = 20 cm)

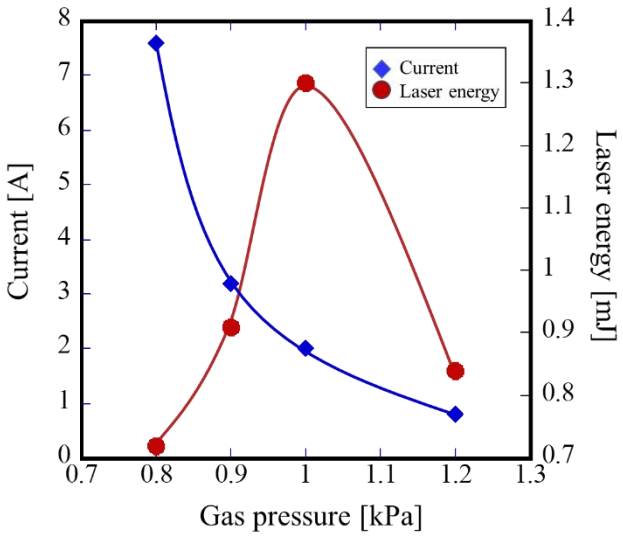

Fig. C-12 Relation between gas pressure, discharge current, and laser energy in the tandem scheme

5.5.2 Relation between discharge current and laser energy in single and tandem scheme

Figure C-13 shows the relation between gas pressure flowing inside the laser tube and the discharge current. In this experiment, the capacitance C_L was fixed to be 2000 pF. The higher the gas pressure flowed inside the laser tube, the lower the amount of current flowed. The decreasing of the discharge current is a result of high discharge impedance due to high gas density.

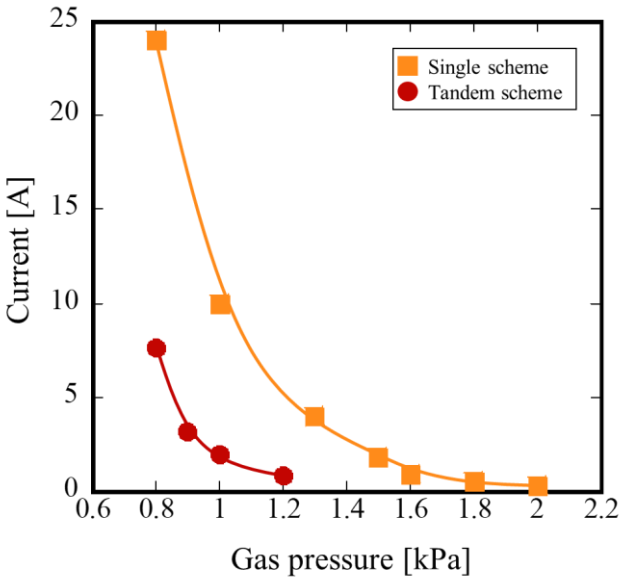

Fig. C-13 Relation between discharge current and laser energy in single and tandem scheme

5.4.3 Relation between electrical energy and laser energy in single and tandem scheme

Figure C-14 shows the dependence of laser output energy on electrical energy. The gas pressure inside the single and tandem scheme was kept constant at 1.3 kPa and 1 kPa, respectively. The horizontal axis that shows the electrical energy stored in the C_L, was calculated by $CV^2/2$, where C and V are the capacitance and applied voltage, respectively. The results obtained indicate that laser energy increases with increasing electrical energy. Although the electrical energy provided in the tandem scheme is higher than in a single scheme, the laser output energy produced by the tandem scheme is lower. In a tandem scheme, when the electrical energy is below 29.2 pF (C_L = 2000 pF), laser oscillation does not occur. High electrical energy is essential for the laser to oscillate. The laser output energy was expected to be higher than the single scheme because the tandem scheme provides a larger discharge volume. This can be considered as a loss in the optical cavity. The efficiency of the single scheme and tandem scheme of longitudinally excited CO_2 laser driven by FHVSS was estimated at about 12% and 7%, respectively. Improvisation is needed for a tandem scheme to increase efficiency.

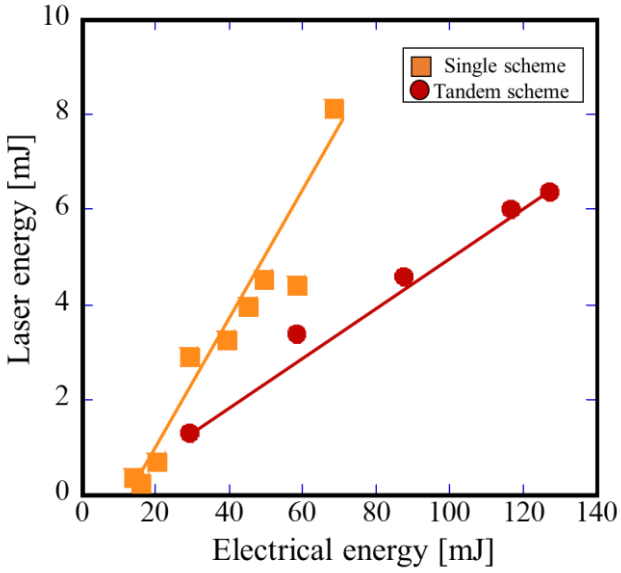

Figure C-14 Relation between electrical energy and laser energy in single and tandem scheme

5.5 Summary

Longitudinally excited CO_2 laser driven by FHVSS in single and tandem schemes has successfully oscillated. In the single scheme, laser characteristics of the laser system with 20 cm and 30-cm length discharge tubes were examined. Laser oscillation was successfully oscillated and produced maximum laser output energy of about 22 mJ for 30 cm-length discharge tube at operating voltage of 10 kV and gas pressure around 2.8 kPa. We

can conclude that higher laser energy can be achieved easily by providing greater input energy, increasing the length of the discharge tube, and operating at optimum gas pressure.

The laser characteristic of the laser system in single and tandem schemes were examined and the results were compared. The laser output energy was expected to be higher than the single scheme because the tandem scheme provides a larger discharge volume. However, through the course of this analysis, several important conceptual flaws were discovered. The low laser output energy produced by the laser system in the tandem scheme can be possibly due to the internal losses caused by the optical resonator. If the resonator mirrors attached at both ends of the electrodes are not perpendicular to the laser tube, internal losses can occur due to the unstable scattering of elements inside the laser tube. To overcome this problem, a window will be attached at one end of the laser tube. The total reflective mirror will uncouple from the laser tube and attach to the mirror holder. The angle of the mirror can be adjusted to get the best angle to produce high laser output energy.

Summary of the appendices

One of the importance of this research lies in the fact that the combination of a longitudinally excited laser scheme and a laboratory-made fast high-voltage solid-state switch (FHVSS) can meet the demands of a simple and compact pulsed gas laser for industrial and medical applications. A simple configuration of longitudinally excited gas laser offers a simple and compact pulsed gas laser because a preionization or fast gas flow system is not required. The longitudinal excitation scheme does not require fast gas flow system, also makes the body compact and decreases the installation area.

FHVSS consisting of an avalanche transistor and series-connected MOSFET or IGBT was developed and demonstrated. The avalanche transistor provides the advantage of fast rise time, while the increased number of series-connected MOSFET or IGBT increases the voltage capacity of this solid-state switch. The FHVSS has advantages that make it suitable for implementation in pulsed-gas lasers. For instance, the spark gap switch used by Uno et al. for the longitudinal excitation scheme can be replaced with the FHVSS to achieve stable laser operation during high repetition rates to provide stable laser operation.

Longitudinally excited CO_2 laser controlled by FHVSS with discharge length of 40 cm that employs spike and sustainer technique produced maximum energy of about 60 mJ when 20 kV of DC voltage is applied at gas pressure around 3 kPa. On the other hand, a longitudinally excited CO_2 laser driven by FHVSS in a single and tandem scheme has been presented. In a single laser scheme, laser oscillation was successfully oscillated and produced maximum laser output energy of about 22 mJ at 2.8 kPa when 7 kV of DC voltage is applied. The advantage of the laser scheme is only one DC voltage is required for the laser operation. This simple and compact laser system can offer the advantage of cost performance.

A future study is needed to improve the laser performance that is capable to produce higher output energy suitable for material processing in industrial applications. For instance, higher laser energy can be easily achievable by increasing the length of the discharge tube and providing greater input energy. Greater input energy, however, can cause higher running costs and shorten the lifetime of the laser. It must be noted that the efficiency of the pulsed power supply also affects the quality and performance of the laser.

The idea of a tandem scheme can be one of the alternatives to increase the laser output energy. In a tandem scheme, two discharge tubes are connected with an intermediate electrode. The laser cavity length is increased. However, the discharge length is short because the voltage is applied at the intermediate electrode. Therefore, the operating voltage required for laser oscillation can be decreased. Theoretically, the tandem scheme construction having a long cavity is expected to produce higher laser output energy than a single scheme.

In the future, a well-designed combination of a longitudinal excitation scheme and an FHVSS that offers simple construction, great compactness, high cost-effectiveness, and high energy efficiency is expected to have superior properties for industrial applications.

List of publications

1. Water temperature as acoustic impedance control for efficient laser peening
   Noor Shahira Masroon, Akihiro Hata, Miho Tsuyama, Manabu Heya, and Hitoshi Nakano
   Optik, 2021, 242, 167097.
2. Effects of Laser Peening Parameters on Plastic Deformation in Aqueous Glycerol Solution as Plasma Confinement layer
   Noor Shahira Masroon, Hikaru Hirata, M. Tsuyama, Manabu Heya, and Hitoshi Nakano
   Journal of Laser Micro/Nanoengineering, 2021, 16, 160-165
3. Control of Plasma Confinement Layer for Effective Laser-peening
   Y. Zhang, N. S. Masroon, Y. Namba, Miho Tsuyama, Manabu Heya, and Hitoshi Nakano
   Journal of Laser Micro/Nanoengineering, 2021, 16, 80-83.
4. Effects of Laser Peening on Various Aluminum Alloys
   Masahiro Yoshiike, Ryotari Oka, Shin Toyokura, Noor Shahira Masroon, Manabu Heya, Miho Tsuyama, and Hitoshi Nakano
   The Review of Laser Engineering, 2021, 49, 50-55.
5. Development of longitudinally excited CO_2 laser
   Noor Shahira Masroon, Miyu Tanaka, Masaya Tei, Kazuyuki Uno, Miho Tsuyama, and Hitoshi Nakano.
   Journal of Physics: Conference Series IOP Science, 2018, 1027,1-6.
6. Simple and Compact Longitudinally Excited CO_2 Laser Driven with a Fast High-Voltage Solid-State Switch
   Noor Shahira Masroon, Sigeyasu Ohashi, M. Tei, M. Tanaka, K. Uno, and H. Nakano
   Journal of Laser Micro/Nanoengineering, 2019, Vol. 14, 186-189.

List of research activities on conference

Domestic Conference

1. 誘導性エネルギー蓄積型パルス電源を用いた小型気体レーザーの開発
   Miyu Tanaka, Shigeyasu Ohashi, Noor Shahira binti Masroon, Kazuyuki Uno, and Hitoshi Nakano.
   平成 29 年電気学会 基礎・材料・共通部門大会 in Muroran Institute of Technology, Japan. Oral presentation. 2017.
2. 小型気体レーザー用高速高電圧固体スイッチの開発
   Masaya Tei, Noor Shahira binti Masroon, Jifaning Achilles, and Hitoshi Nakano,
   平成 29 年電気学会 基礎・材料・共通部門大会 in Muroran Institute of Technology, Japan. Oral presentation. 2017.
3. 軸方向放電励起方式における短パルス CO_2 レーザーの開発
   Shigeyasu Ohashi, Miyu Tanaka, Noor Shahira binti Masroon, Kazuyuki Uno, and Hitoshi Nakano.
   平成 29 年電気学会 基礎・材料・共通部門大会 in Muroran Institute of Technology, Japan. Oral presentation. 2017.
4. 軸方向放電励起方式における短パルス CO_2 レーザーの開発
   Shigeyasu Ohashi, Miyu Tanaka, Noor Shahira binti Masroon, Kazuyuki Uno, and Hitoshi Nakano.
   平成 29 年電気関係学会関西支部連合大会 in Kindai University Japan. Oral presentation. 2017.
5. Longitudinally excited CO_2 laser driven by fast high-voltage solid state switch
   Noor Shahira binti Masroon, Shigeyasu Ohashi, Miyu Tanaka, Masaya Tei, Kazuyuki Uno, and Hitoshi Nakano.
   平成 30 年電気学会全国大会 in Kyushu University, Japan. Oral presentation. 2018.
6. 短パルス軸方向放電励起方 CO_2 レーザーの開発
   Shigeyasu Ohashi, Noor Shahira binti Masroon, Kazuyuki Uno, and Hitoshi Nakano.
   平成 30 年基礎・材料・共通部門大会 in Himeji, Japan. Oral presentation. 2018.
7. 短パルス軸方向放電励起方 CO_2 レーザーの開発
   Shigeyasu Ohashi, Noor Shahira binti Masroon, Kazuyuki Uno, and Hitoshi Nakano.
   平成 29 年電気関係学会関西連合大会 in Osaka Institute of Technology, Japan. Poster presentation. 2018.
8. 高速高電圧固体スイッチで動作する軸方向放電励起 CO_2 レーザーの開発
   Daisuke Asaya, Daiki Toyama, Noor Shahira binti Masroon, Kazuyuki Uno, and Hitoshi Nakano.

令和元年電気学会　基礎・材料・共通部門大会 in Iwate University. Poster presentation. 2019.

9. Effects of controlling acoustic impedance of plasma confinement layer on laser peening Noor Shahira Masroon, Akihiro Hata, Noriaki Kishida, Manabu Heya, Miho Tsuyama, and Hitoshi Nakano
   レーザー学会学術講演会第 40 回年次大会 in Sendai, Japan. 2020.
10. Effects of laser peening parameters on plastic deformation of stainless steel in aqueous glycerol solution
    Noor Shahira Masroon, Miho Tsuyama, Mabu Heya, and Hitoshi Nakano
    令和 3 年度レーザー学会九州支部学生講演会. Oral presentation. 2021. (Online)

International Conference

1. Effects of Laser Peening Parameters on Plastic Deformation in Aqueous Glycerol Solution as Plasma Confinement layer
   Noor Shahira Masroon, Hikaru Hirata, Miho Tsuyama, Manabu Heya, and Hitoshi Nakano
   The 22nd International Symposium on Laser Precision Microfabrication. 2021. (Online)
2. Control of Plasma Confinement Layer for Effective Laser-peening
   Yang Zhang, Noor Shahira binti Masroon, Yoshinari Namba, Miho Tsuyama, Manabu Heya, and Hitoshi Nakano
   The 22nd International Symposium on Laser Precision Microfabrication. 2021. (Online)
3. Longitudinally excited CO_2 laser driven by fast high-voltage solid state switch
   Noor Shahira binti Masroon、Shigeyasu Ohashi、Miyu Tanaka、Masaya Tei、Kazuyuki Uno、Hitoshi Nakano
   The 7th Advanced Lasers and Photon Source (ALPS2018) in Pacifico Yokohama. Poster presentation. 2018.
4. Development of longitudinally excited CO_2 laser
   Noor Shahira binti Masroon, Miyu Tanaka, Masaya Tei, Kazuyuki Uno, Miho Tsuyama, Hitoshi Nakano
   International Laser Technology and Optics Symposium 2017 (iLATOS2017) in Pulai Spring Resort, Johor, Malaysia. Poster presentation. 2017.